VOLUME AVERAGE TECHNIQUE FOR TURBULENT FLOW SIMULATION AND ITS APPLICATION TO ROOM AIRFLOW PREDICTION

A Thesis Submitted to
The College of Graduate Studies and Research
in Partial Fulfilment of
The Requirements for
The Degree of Doctor of Philosophy
in
The Department of Mechanical Engineering
University of Saskatchewan
by

Xianmin Huang
Saskatoon, Saskatchewan
September, 1997

Copyright Statement

Abstract

Fluid motion turbulence is one of the most important transport phenomena occurring in engineering applications. Although turbulent flow is governed by a set of conservation equations for momentum, mass, and energy, a Direct Numerical Simulation (DNS) of the flow by solving these equations to include the finest scale motions is impossible due to the extremely large computer resources required. On the other hand, the Reynolds Averaged Modelling (RAM) method has many limitations which hinder its applications to turbulent flows of practical significance. Room airflow featuring the co-existence of laminar and turbulence regimes is a typical example of a flow which is difficult to handle with the RAM method. A promising way to avoid the difficulty of the DNS method and the limitation of the RAM method is to use the Large Eddy Simulation (LES) method.

In this thesis, the drawbacks of previously developed techniques for the LES method, particularly those associated with the Subgrid Scale (SGS) modelling, are identified. A new Volume Average Technique (VAT) for turbulent flow simulation is then proposed. The main features of the VAT are as follows:

1) The volume averaging approach instead of the more common filtering approach is employed to define solvable fields, so that coarse-graining in the LES and space discretization of the numerical scheme are achieved in a single procedure.

2) All components of the SGS Reynolds stress and SGS turbulent heat flux are modelled dynamically using the newly proposed Functional Scale Similarity (FSS)

SGS model. The model is superior to many previously developed SGS models in that it can be applied to highly inhomogeneous and/or anisotropic, weak or multi-regime turbulent flows using a relatively coarse grid.

3) The so-called SGS turbulent diffusion is identified and modelled as a separate mechanism to that of the SGS turbulent flux represented by the SGS Reynolds stress and SGS turbulent heat flux. The SGS turbulent diffusion is defined in the coarse-graining procedure, and is responsible for most of the energy dissipation.

4) A new 3-D collocated scheme for the solution of viscous incompressible fluid flow, based on the SIMPLE and fractional-step methods, is developed for the LES.

Benchmark tests of the VAT are performed based on 2-D and 3-D lid-driven and 3-D buoyancy-driven cavity flows to demonstrate the accuracy and performance of both the numerical method and LES model. Finally, as an example of a practical calculation, the VAT is applied to the LES of airflow in an enclosed air-conditioned room with a wall-mounted cooling inlet and an outlet on the opposite wall.

Using the VAT, many problems associated with the conventional LES techniques have been at least partially solved. With the development of the VAT and similar approaches, it should soon be possible to use of the LES method to simulate a real flow of engineering interest with the computer resources provided by a workstation.

Acknowledgements

The author would like to thank his supervisor Professor D.J. Bergstrom for his significant help throughout the author's Ph.D. program and thesis work. Also, help from Professor J.D. Bugg, Professor R.W. Besant, Professor D.H. Male, Professor C.A. Shook, Professor J.N. Wilson, and Professor J.A. Kells is greatly appreciated. Additional thanks go to I.J. Macphedran and Keith Jeffrey of the Engineering Computing Services.

Funding for the research work was provided by a University of Saskatchewan Scholarship and from the research grant of Professor D.J. Bergstrom provided by the Natual Science and Engineering Research Council of Canada. The VPX240/10 supercomputer CPU time was awarded by the High Performance Computing Center in Calgary. This funding is greatly appreciated.

Finally, financial support was also provided by my parent Tiyi Huang, aunt Huiying Huang, and uncle Tixin Huang. Special thanks go to my wife Zhongmei Lu and daugher Chonglu (Lucy) Huang for their understanding, concern, and support.

This thesis is dedicated to my parents

Mr. Tiyi Huang and Mrs. Meiying (Lin) Huang

for their love, understanding, and encouragement.

Contents

Nomenclature

Italic Symbols

A	surface area of a control volume
A_{in}	area of airflow inlet in a room
A_{out}	area of airflow outlet in a room
a, b, b'	coefficients in finite volume scheme
B, B_i	dominant length scale of correlations of fluctuations
$\bar{B}, \bar{B}_i$	normalised values of B and B_i
C_{ij}	the cross-correlation term
C_l	coefficient
C_ν	coefficient for eddy viscosity modelling
C_ν^*	coefficient for second eddy viscosity modelling
C'	coefficient
$\mathcal{C}$	model coefficient
$\mathcal{C}_{ij}$	model coefficient
$\mathcal{C}_{\theta j}$	model coefficient

E	turbulent kinetic energy
f	dominant frequency of inlet or outlet flow fluctuations
f	wall function
f	geometric factor
f_w	weighting factor for time average
$\mathcal{F}$	operator of Fourier transform
g	gravitational acceleration
g	Fourier transform of spatial filter function
g_i	1-D Fourier transform of spatial filter function
G	spatial filter function
G_i	1-D spatial filter function
h	characteristic filter width
i	imaginary unit $= \sqrt{-1}$
I_t	turbulence intensity
J	total flux of transported quantity Φ
k	wave number (scalar)
k_c	truncated wave number
k_i	1-D wave number
K	SGS kinetic energy
K_0	the Komogoroff constant
$K_{\tau_{ij}}$	Modelling coefficient for FSS SGS model
K_{σ_j}	Modelling coefficient for FSS SGS model

$\mathbf{k}$	wave number vector
$\mathcal{K}$	volumetric weighting factor
l	mixing length
L	length scale of cavity flow domain
L	characteristic length scale
L_{ij}	the Leonard term
L_{ij}	a tensor in the Germano's dynamic SGS model
L_x, L_y, L_z	length scale of cavity flow domain
L_g	length scale of a room airflow inlet grille grid
m	$= max(\Delta, \eta)$
$\tilde{m}_j$	$= \frac{m}{\Delta_j}$
M_{ij}	a tensor in the Germano's dynamic SGS model
N	number of mesh points required for full simulation
p	SGS pressure fluctuation
P	instantaneous pressure
P	SGS coarse grained pressure
P'	SGS coarse grained pressure (old)
$\tilde{P}$	SGS coarse grained pressure
P'	pressure correction field
Pr	Pandtl number
Ra	Rayleigh number
Re	Reynolds number

R_i	$= \frac{t_{ii}-T_{ii}}{t_{ii}}$
R_m	mass residual
R_p	pressure correction equation residual
R_v	clipping coefficient for τ_{ij}
R_t^j	clipping coefficient for σ_j
$\mathcal{R}$	ratio of length scale
s_j	TGS turbulent heat flux
S	source terms in QUICK scheme
S_j	IGS turbulent heat flux
S_Φ	source term in transport equation of Φ
$\tilde{S}_{ij}$	strain rate of SGS coarse grained velocity
$\lvert\tilde{S}\rvert$	magnitude of $\tilde{S}_{ij}$
t	time
t_{ij}	TGS Reynolds stress
T_{ij}	IGS Reynolds stress
u, v, w	SGS fluctuation of velocity components
u_i	SGS fluctuation of velocity components
u', v', w'	TGS fluctuation of velocity components
u_i'	TGS fluctuation of velocity components
$\breve{u}_j$	RSM of SGS fluctuation u_j
$\breve{u}_t$	RSM of turbulent fluctuation on a room airflow inlet
U_0	driving velocity of LDC flow

U_b	Buoyancy velocity of BDC flow
U_i	instantaneous velocity components
$\tilde{U}_i$	SGS coarse grained velocity components
U, V, W	instantaneous velocity components
$\tilde{U}, \tilde{V}, \tilde{W}$	SGS coarse grained velocity components
$\tilde{U}, \tilde{V}, \tilde{W}$	SGS coarse grained velocity components
$\tilde{U}_i$	SGS coarse grained velocity components
$\hat{U}_i$	TGS coarse grained velocity components
$\hat{U}, \hat{V}, \hat{W}$	TGS coarse grained velocity components
$\vec{U}, \vec{V}, \vec{W}$	flux velocities at CV surfaces
$\vec{U}', \vec{V}', \vec{W}'$	flux velocities at CV surfaces (old)
v_{rms}	RMS of SGS velocity fluctuation
V	characteristic velocity
V	volume of CV
V_{in}	room airflow inlet mean velocity
V_{out}	room airflow outlet mean velocity
$\tilde{V}_{total}$	magnitude of solvable velocity
V_{max}	magnitude of maximum possible instantaneous velocity in a flow
$\mathbf{x}, \mathbf{x}'$	position vector
x, y, z	Cartesian coordinates
x_1, x_2, x_3	Cartesian coordinates
X	length scale coordinate

Greek Symbols

α	thermal diffusivity of fluid
α_j	SGS eddy diffusivity representing turbulent diffusion
α_t	anisotropic eddy diffusivity on a room airflow inlet
β	volumetric expansion rate
Γ	diffusion factor on CV surface
γ	high limit of the dynamic length scale range
γ_i	high limit of the dynamic length scale range
$\bar{\gamma}_j$	$= \frac{\gamma}{\Delta_j}$
δ_i	central difference in each Cartesian direction
Δ	characteristic length scale of SGS level coarse graining
Δ'	characteristic length scale of TGS level coarse graining
Δ_i	value of Δ in each Cartesian direction
Δt	time step
Δ'_i	value of Δ' in each Cartesian direction
$\Delta x, \Delta y, \Delta z$	length scales of CV in each Cartesian direction
Δx_i	length scales of CV in each Cartesian direction
ϵ	dissipation rate of turbulent energy per unit mass
η	Kolmogoroff length scale
η	low limit of the dynamic length scale range

η_i	low limit of the dynamic length scale range
θ	SGS fluctuation of temperature
θ'	TGS fluctuation of temperature
θ_0	random initial phase for turbulent in- and outlet boundary condition
θ_{rms}	RMS of SGS temperature fluctuation
Θ	instantaneous temperature
Θ_{cold}	cold wall temperature
Θ_{hot}	hot wall temperature
Θ_{max}	maximum possible instantaneous temperature in a flow
Θ_{min}	minimum possible instantaneous temperature in a flow
Θ_w	wall temperature (relative) of a room
$\tilde{\Theta}$	SGS coarse grained temperature
$\hat{\Theta}$	TGS coarse grained temperature
κ	the Von Karman constant
ν	kinematic viscosity
ν_t	SGS eddy viscosity
ν_t'	TGS eddy viscosity
ξ_{ij}	turbulent diffusion term in volume averaged momentum equation
ρ	density
ρ_0	density

σ_j	SGS turbulent heat flux
τ_{ij}	SGS Reynolds stress
τ'_{ij}	TGS Reynolds stress
Φ	instantaneous value of a general transported quantity
$\tilde{\Phi}$	SGS coarse grained value of Φ
ϕ	Fourier transform of Φ
ϕ	turbulent fluctuation in Φ
$\tilde{\phi}$	Fourier transform of $\tilde{\Phi}$
ψ_j	turbulent diffusion term in volume averaged energy equation

List of Figures

List of Tables

List of Abbreviations

ACH	Air Change rate per Hour
ADLGS	Alternating Direction Line Gauss-Seidel
CFD	Computational Fluid Dynamics
CFL	Courant-Frriedrichs-Lewy
CPI	Consistent Physical Interpolation
CV	Control Volume
DNS	Direct Numerical Simulation
FSM	Fractional-Step Method
HVAC	Heating, Ventilating, and Air-Conditioning
HPCC	High Performance Computing Centre
IGS	Inter-Grid Scale
IRT	International Research Team
LES	Large Eddy Simulation
LDA	Laser Doppler Anemometry
LDC	Lid-Driven Cavity
LHS	Left Hand Side

PWI	Pressure Weighted Interpolation
PRIME	update PRessure Implicit, Momentum Explicit
QUICK	Quadratic Upstream Interpolation for Convective Kinematics
RAM	Reynolds Average Modelling
RHS	Right Hand Side
RMS	Root-Mean-Square
SI	System International
SGS	Sub-Grid Scale
SMC	Second Moment Closure
SIMPLE	Semi-Implicit Method for Pressure-Linked Equations
TGL	Taylor-Gortler-Like
TGS	Test-Grid Scale
VAT	Volume Average Technique
1-D	One-Dimensional
2-D	Two-Dimensional
3-D	Three-Dimensional

Chapter 1

Introduction

1.1 Turbulent Flow Simulation — The Challenge

Since O. Reynolds published his famous paper on the discovery of the existence of two different regimes in a pipe flow in 1883, it has been broadly accepted by fluid dynamicists that fluid motion can be classified as either laminar or turbulent. Laminar flows, featured as being strongly viscous, stable, and determinable, have been extensively investigated since the last century. Today, laminar flows are well understood and their theory is systematically developed. Numerical simulation of laminar flows has become routine in modern CFD practice.

The situation is far different for turbulent flows which are characterised as being unstable, chaotic, and indeterminable. Turbulence is the most complicated kind of flow making even its precise definition difficult. Although it has been investigated for more than a century, turbulence is still an "unsolved" problem in mechanics;

the nature of turbulence is not well understood and some turbulence phenomena are still unexplained or have only inconsistent explanations among different schools of fluid dynamicists. Lack of knowledge of turbulent flows hinders the development of simulation techniques for them. On the other hand, since most flows occurring in nature and in engineering applications are turbulent rather than purely laminar, numerical simulations for turbulent flows are required.

It should be pointed out that, although the nature of turbulence is hard to understand, fluid dynamicists have reached a general agreement that the smallest eddy in a turbulent flow is several orders larger than the fluid molecules so that, for most industrial and environmental turbulent fluid motion, a continuum hypothesis is still valid. In such a context, turbulence means a 3-D transient motion of fluid, in which the randomly varying quantities are still governed by the conservation laws of mass, momentum, and energy. It is believed that, if the governing equations could be solved numerically with high enough temporal and spatial resolution to include the smallest eddy motions, the results would be in excellent agreement with those from experimental measurement. However, this so called "Direct Numerical Simulation" approach of turbulent flows is impossible to realize at present and in the near future. According to the energy theory of turbulence, the smallest scale of eddies at which dissipation takes place is determined by the Reynolds number, a dimensionless parameter related to the mean-flow kinetic energy in the flow domain and the molecular viscosity of the fluid. In a flow at a Reynolds number at which the fluid turbulence can be maintained, the smallest scale of eddies would be several hundred times smaller than the scale of the flow domain. Therefore, a grid of at least hundreds of millions of cells would be required to capture features of all the eddies in a turbulent flow. Such a simulation is far beyond the capacity (both memory size and speed) of today's largest supercomputer.

Since, with today's computers, even the simplest practical turbulent flow is impossible to simulate directly and engineers are mainly interested in the mean values of fields, one turns to Reynolds-Averaged Modelling (RAM) methods. The RAM meth-

ods are based on the Reynolds-averaged equations which are obtained by decomposing velocity, pressure, and temperature into mean and fluctuating parts in the governing equations, and then taking an ensemble mean. The Reynolds-averaged equations themselves do not represent a closed system for the determination of the mean velocity, temperature, and pressure because of the "Reynolds-stress tensor" which contains six additional unknowns and the "turbulent heat flux vector" which contains another three additional unknowns, both of which appear in the Reynolds-averaged equations due to the process of ensemble averaging. Different versions of the Reynolds-average closure models represent different methods of relating the Reynolds stress tensor and the turbulent heat flux vector to the mean velocity, temperature, and pressure fields in some physically consistent fashion. In this way, the Reynolds-averaged equations are closed. With the RAM method, it is possible to simulate flows found in practice with the capacity of today's computers.

Over the last century, tremendous efforts have been made by some respected scientists in the fields of physics and mathematics to rigorously derive the two-point Reynolds-average closure models using elegant theories of statistics and nonlinear dynamics for the Reynolds averaged equations in forms of both physical and wave number space. This work was pioneered by G.I. Taylor (1935). A.N. Kolmogoroff's (1949) outstanding works in the theory of local homogeneous and isotropic turbulent flow resulted in the "2/3 Kolmogoroff law". Recent development of the work is based on several new concepts, such as "renormalization perturbation" and "renormalization group" theory. However, all of the above elegant models developed so far are too complicated for practical use and have been limited to homogeneous (usually isotropic) flows which do not really exist in practical applications. It seems that the theoretical modelling of turbulence is so challenging that any research tool found successful in remotely similar problems is soon brought to bear. On the other hand, engineers have created a semi-empirical approach for the one-point Reynolds-average closure models. The semi-empirical approach derives the required closure expressions by employing some qualitative conclusions from the statistical theory of homogeneous and isotropic turbulence and the dimensional analysis technique. Any unclear

relationships among parameters are lumped into coefficients which can be further determined by experiments. The semi-empirical closure models are not yet accurate enough, but are the only choice in engineering application.

Simple semi-empirical closure models of the RAM method are the eddy diffusivity models in which the Reynolds stress tensor and the turbulent heat flux vector are modelled using an eddy diffusivity hypothesis based on an analogy between molecular and turbulent motions. Thus, the Reynolds stress and the turbulent heat flux can be related to the gradient of mean flow fields through, respectively, an eddy viscosity and an eddy heat diffusivity. The eddy viscosity and eddy heat diffusivity are calculated from turbulence length and time scales specified in the flow. Prandtl's (see Hinze, 1975) mixing-length model was one of the first eddy-viscosity models proposed for 2-D boundary layers. In this model, a prescribed "mixing length" and the inverse of the normal velocity gradient are employed as, respectively, the turbulence length and time scales. Kolmogoroff (see Hinze, 1975) proposed that turbulent flow phenomena should be closed by solving two equations. The first of these is for energy of the turbulent motion and the second is for its "frequency". The second equation is normally regarded as an auxiliary one. Such models are the one equation turbulence models, in which the turbulence length scale still needs to be prescribed. An obvious way to provide more effective dependence of the turbulence length scale on the flow is to derive a transport equation for it. Thus, two-equation models were developed. An early two-equation model was that proposed by Harlow and Nakayawa (1968). This model, after modification by Launder and Spalding (1974), has been widely applied. It is often called the standard $k-\epsilon$ model, where k represents turbulence kinetic energy, and ϵ is its dissipation rate. More complex semi-empirical closure models of the RAM type are the second moment closure models which explicitly employ transport equations for individual Reynolds stresses and turbulent heat fluxes. The unknown high-order correlations appearing in the transport equations are expressed in terms of the second-order correlations themselves. The second moment closure models do not rely on the eddy diffusivity hypothesis, and therefore relax some unreasonable assumptions.

Although the RAM methods, mainly the ones using the well developed $k-\epsilon$ models, have enjoyed considerable success in prediction of simple turbulent flows, it has not been successful in complex flows, particularly those with strong inhomogeneity, anisotropy, or unsteadiness. Thus, it is important to consider carefully the suitability of the RAM method to turbulent flow simulation. The main reason for the problem-dependent performance of the RAM method is that the assumptions imposed on the Reynolds average turbulence models are so many that not all of them can be valid for flows of practical interest. These assumptions include: 1) high Reynolds number; 2) homogeneous turbulence; 3) gradient-type turbulent diffusion; and 4) similarity of spatial distribution of turbulence quantities. The fact is that all of the Reynolds average turbulence models, ranging in complexity from enhanced coefficients of eddy diffusivities to an additional system of partial differential equations, contain adjustable coefficients that should be determined empirically. Although changing values of these empirical coefficients may, to some extent, offset the deficiency of the RAM method relating to invalid assumptions, such a change relies on experiments and has only a limited range of adjustment. Therefore, the RAM method is not a reliable approach for complex turbulent flows.

Wall-bounded flows represent the main type of flow encountered in engineering application, but also the most difficult kind of flow to be handled by the RAM method. The presence of a wall imposes constraints on the flow. The most obvious constraint is that the viscosity of the fluid enforces the no-slip condition, *i.e.* the velocity of the fluid at the solid surface must be equal to the velocity of the surface. Another constraint in near-wall turbulent flow is the preferential damping of the turbulent velocity fluctuations normal to the wall as the surface is approached. This constraint arises from facts other than viscosity, and makes the turbulence weaker and more anisotropic. Therefore, the first two assumptions for the RAM method, *i.e.* high Reynolds number and homogeneous turbulence, can not be satisfied for a wall-bounded turbulent flow. Flows in the immediate vicinity of the wall are always laminar. The patterns of the flow farther away from the wall in the near-wall region and their effect on the outer flow depend strongly on the speed of the outer flow

relative to the wall surface. If the relative speed of the outer flow is high enough, a so-call "burst-and-sweep" process will be triggered in the near-wall region. This process functions as a source of turbulence production in the near-wall region. In this case, the flow in the near-wall region behaves as a thin boundary layer which has only a limited effect on the outer flow. Furthermore, if the direction of the outer flow is almost parallel to the wall surface (*e.g.* in a pipe or channel flow), the log-law velocity profile is usually valid in the near-wall region. With the log-law profile, one can avoid simulating the near-wall region when the RAM method is applied, and therefore alleviate the problem of invalid assumptions. However, the log-law profile is no longer valid if the direction of the outer flow is changing. On the other hand, if the relative speed of the outer flow is low, the only effect of the wall constraint is to retard the fluid motion. When a wall is approached, the flow experiences a consistent decrease in speed and turbulent fluctuation. In such a case, there is a continuous change of the local Reynolds number from an extremely low value near the wall to a relatively high value remote from the wall, and the flow is strongly inhomogeneous. Such a flow is beyond the simulation capacity of any RAM method.

It should be pointed out that over the past two decades, efforts have been made to extend the RAM method to use at low Reynolds numbers and to describe the flow close to a solid wall. The research has been carried out in two directions. One is to extend the two-equation closure models to low-Reynolds-number flows by incorporating either a wall damping effect or a direct effect of molecular viscosity, or both, on the empirical constants in the turbulent transport equations devised originally for high Reynolds number, fully turbulent flows remote from the wall. Another is to extend the second moment closure models to near-wall flows by modifying the high-Reynolds-number versions of models of the correlations appearing in the transport equations for the individual Reynolds stresses and turbulent heat fluxes. However, these so-called low-Reynolds-number models have the same physical basis as their high-Reynolds-number counterparts. Therefore, the low-Reynolds-number models share with their counterparts many of the same deficiencies. Previous practice shows that the success of the low-Reynolds-number version RAM method is still limited to some simple

parallel wall-bounded flows.

Jets are another kind of flow frequently found in engineering application that may cause problems when simulated using the RAM method. The problems are the low local Reynolds numbers in regions near the boundaries of jets, and the co-existence of the laminar and turbulent flow regimes. Furthermore, when a jet is confined by solid walls, it is inclined to drift and attach randomly on one of the nearby walls depending on its initial perturbation. This so called "multi-solution" phenomenon cannot be accurately predicted by the RAM method.

In view of the above arguments, for simulation of most engineering turbulent flows, the RAM method is not suitable, while the DNS method is at present only a dream. A promising way to avoid the difficulty of the DNS method as well as to remove the deficiency of the RAM method is to use the Large Eddy Simulation (LES) method. In LES, large scale fields are computed directly, while the Sub-Grid Scales (SGS) of the fields are modelled. The sub-grid scales of the fields are assumed to be more nearly universal so that the statistics and their effect upon the large scale can be specified by a small number of parameters. The method allows using a relatively simple SGS turbulence model and a coarse grid mesh which can fit into existing computers.

1.2 LES of Turbulence and Some Problems

Since the pioneering work of Deardorff (1970), LES has developed as a method for simulating wall-bounded turbulent flows of moderate complexity. A detailed review of the present state of the LES method with a historical perspective will be given in the next chapter. In this section, we point out in advance some issues of the LES method, which should be studied and clarified before the method can be confidently applied in engineering practice.

The first issue open to question is how to define the large scale component of the

flow field which the method will attempt to calculate directly. There are generally two ways of doing this: the filtering approach of Leonard (1973), and the volume-averaging approach of Schumann (1974). These two approaches are equivalent, respectively, to low-pass filtering the governing equations in Fourier space (whole domain smoothing) and averaging the governing equations over a small region of physical space (local smoothing). For historical reasons, it has been broadly accepted that the filtering approach is superior to the volume-averaging approach in that it can lead to continuously distributed filtered fields. Almost all of the previous applications of the LES method were based on the filtering approach. One criticism to the volume averaging approach is that it leads to two kinds of averages, *i.e.* volume averages and surface averages. Both of averages appear in the volume averaged governing equations, and are difficult to handle simultaneously. However, the author is strongly in favour of using the volume averaging approach.

An apparent advantage of the volume averaging approach which had already been identified by some previous researchers is that it can directly reach a discretized finite difference scheme for the governing equations. In the volume averaging approach, the volume average procedure serves for both field smoothing and solution domain discretization. However, to justify the filtering approach, one should presumably assume that solution domain discretization has no effect on the filtered field quantities, or view the filtering procedure as only a nominal guide for the SGS modelling, and still use the volume averaging approach in numerical implementation. The former assumption is apparently not accurate, while the latter approach (adopted by many simulators) will actually lead to the volume averaging approach itself. For the filtering approach, most kinds of filters, such as the ideal filter or Gaussian filter, are difficult to realize in physical space. Thus, the simplest "top-hat" filter is broadly employed for LES of flows with engineering significance. The "top-hat" filter looks (but actually is not) identical to volume averaging at discretized points of the solution domain. This may explain why some people are inclined to confuse these two smoothing approaches in their LES practice.

When applying a smoothing approach (filtering or volume averaging) to convective transport equations of a field, the so called SGS-related terms will appear. In the filtering approach, all of these terms including the Leonard term, the SGS flux term, and two cross-correlation terms should be modelled to close the solution system. On the other hand, using the volume averaging approach will lead to a simple expression for the SGS-related terms in which both the Leonard term and the cross-correlation terms vanish. Strict reasoning shows that a so called turbulent diffusion mechanism which should be modelled in the LES is ignored by both the filtering and volume averaging approaches. Physically, the turbulent diffusion represents a turbulent transport enhancement mechanism distinct to that represented by the SGS flux term. Considering the turbulent diffusion is not essential if one tries to model all of the SGS-related terms into a postulated eddy diffusivity with an adjustable coefficient. However, they should be handled in the dynamic SGS models where each SGS-related term is modelled in a self-consistent way without using adjustable coefficients. As to the handling of the two kinds of averages in the finite difference scheme for the governing equations, it is an old issue which has already been dealt with in the conventional finite-volume method.

Another favourable feature of the volume averaging approach is the so called "supersedity" which means that if two volume-averaging processes are applied successively to a field, and if the averaging volume of the one is a subset of the other, then the averaging process with the smaller averaging volume will have no effect on the final averaged field and appears to be "superseded" by the one with the larger averaging volume. The filtering approach does not have such a feature, except when the filter employed is the "ideal filter". However, use of the ideal filter is always avoided due to its complexity in physical space. The dynamic SGS modelling method requires that a test-grid level smoothed (filtered or averaged) field be obtainable numerically from the corresponding sub-grid level smoothed field. This requirement is satisfied due to supersedity when the volume averaging approach is applied. On the other hand, no matter what kind of the filter is employed, the filtering approach cannot satisfy this requirement.

Since a discretized numerical scheme will ultimately be used to solve the large scale flow fields, whether or not the large scale flow fields are continuous, is not significant. If the finite-volume method is applied as a numerical scheme for the large scale motions of a flow, and if the control volume for the finite-volume method is also defined as the SGS volume, the finite-volume discretization of the fields through integration over each control volume is identical to the SGS volume averaging process of the LES. Thus, an extra calculation for defining large scale motion can be avoided.

The second issue to be examined is the SGS model which is the key to the success of the LES method. Commonly used SGS models are the eddy diffusivity models, which lump the SGS turbulence effect into the so-called SGS eddy viscosity (in the momentum equation) and SGS eddy heat diffusivity (in the energy equation). Although efforts have been made to derive and solve a transport equation for the SGS turbulence energy to provide the velocity scale for the SGS eddy viscosity, the expense involved in solving an additional equation does not seem to be justified by improvements in accuracy (Piomelli, 1993). Thus far, the most popular SGS eddy diffusivity model is still the Smagorinsky model which relates the eddy diffusivity directly to the sub-grid length scale and the magnitude of the resolved strain rate tensor. Recently, Germano *et al.* (1991) developed the so-called dynamic SGS model which remarkably improves the Smagorinsky model by calculating the model coefficients (the Smagorinsky coefficients) dynamically as functions of both space and time. The key assumption on which this method is based is that the Smagorinsky coefficients are independent of the characteristic width of the smoothing (filtering or volume averaging) used. This assumptiom requires that the characteristic width of the smoothing be encompassed by the inertial-range scale of the turbulence, so that the small scales are in equilibrium, *i.e.* the energy production and dissipation are in balance. In order to determine the Smagorinsky coefficients dynamically, another smoothing process which is referred to as "test-grid smoothing" with a characteristic width greater than that for the sub-grid smoothing is also applied to the flow fields. It should be pointed out that "supersedity" is required to derive the equations relating the Smagorinsky coefficients with the test-grid smoothed "sub-grid smoothed fields".

Thus, the dynamic SGS model of Germano *et al.* is only valid in the context of the volume-averaging approach. Unfortunately, this fact appears to have been ignored by most previous LES work.

It has been shown that the dynamic SGS model of Germano *et al.* has many desirable features: it exhibits a better asymptotic behaviour near a solid wall and in a laminar flow than the original eddy diffusivity SGS models, and is capable of accounting for counter-gradient momentum or heat transfer (energy backscatter). However, the Smagorinsky model is not a suitable model for strongly inhomogeneous and anisotropic flows. The limitation is mainly due to the invalidity of the eddy diffusivity hypothesis in these flows, and the problem is only partially remedied by using dynamically determined Smagorinsky coefficients. It has been generally accepted that, if the SGS Reynolds stress tensor and the SGS turbulent heat flux vector can be modelled directly without using the eddy diffusivity hypothesis, the accuracy of the SGS modelling would be greatly improved. A model of this nature is the scale similarity model proposed by Bardina *et al.* (1980) which is based on the assumption that the main interaction between resolved and SGS eddies take place between the smallest resolved eddies and the largest SGS ones. Since the interaction components are very much alike, the SGS velocity is approximated by the difference between the filtered and twice-filtered velocities. This gives a model of the form

$$\tau_{ij} = C(\tilde{U}_i\tilde{U}_j - \widetilde{\tilde{U}_i}\widetilde{\tilde{U}_j}) \tag{1.1}$$

where τ_{ij} denotes the SGS Reynolds stress, U_i denotes velocity component in i-direction, over-tilde represents the filtering operator, and the coefficient C was revised from 1.1 to unity by Speziale (1985) to ensure Galilean invariance. So far, the only criticism to this model is that it does not dissipate energy, and can cause numerical instability. To remedy this, the so-called mixed SGS model was proposed by introducing a Smagorinsky-like term into the scale similarity model to account for the proper energy dissipation. Zang *et al.* (1992) improved the performance of the mixed

SGS model by calculating the model coefficients appearing in the Smagorinsky-like term dynamically as functions of both space and time from smoothed fields at both sub-grid and test-grid levels. This so-called dynamic mixed SGS model has shown some advantages over the dynamic eddy diffusivity SGS model originally proposed by Germano *et al.*.

In spite of their remarkable success in predicting some benchmark flows, the accuracy of the theoretical basis behind the dynamic eddy diffusivity or dynamic mixed SGS models is still open to question. First of all, allowing energy backscatter is a desirable feature of both the dynamic eddy diffusivity and dynamic mixed SGS models, but "over-backscatter" of the energy may occur which will result in an exponential instability of the solution. In the simulations by Zang *et al.* (1992), this problem was avoided by locally averaging the calculated Smagorinsky coefficients within a rectangular volume using a stencil of three grid points in each direction and also setting the total viscosity $\nu + \nu_t$ to be zero whenever it became negative. The excessive backscatter of energy is mostly due to the invalidity of the eddy-diffusivity hypothesis. Since the eddy-diffusivity SGS model uses a diffusion transport to model SGS turbulent transport in all directions, the real turbulent transport in each direction will be significantly distorted in regions of inhomogeneous, anisotropic turbulence where the "backscatter" is strong. Thus, a more general remedy to this problem is to totally give up the eddy-diffusivity hypothesis and use an all-component Reynolds stress SGS model instead. Furthermore, the expressions applied to dynamically determine the Smagorinsky coefficients in both the dynamic eddy diffusivity and dynamic mixed SGS models are tensor equations. For the scalar coefficients to be computed, the expressions are "over-determined". In other words, we can not find values of the scalar coefficients which will satisfy the balance of all components in their tensor equations. Any method designed to calculate scalar values of the Smagorinsky coefficients will bring in additional errors to the SGS modelling.

It is true that being less dissipative is one of the reasons for the lack of success of the original scale similarity model proposed by Bardina. The too small dissipation

is mostly due to the fact that the turbulent diffusion, which represents most of the positive energy dissipation was ignored in the model by Bardina. Another reason is that it is difficult to justify equation (1.1) based on the assumption that the SGS velocity can be approximated by the difference between the filtered and twice-filtered velocities. From the author's point of view, numerical instability should not be viewed as a big problem in LES of turbulent flow. The fact is that both strong dissipation and strong unsteadiness are typical features of turbulent flows where they coexist and interact with each other. Therefore, it is not justified to avoid the numerical instability by arbitrarily involving an extra diffusivity in the SGS model. Instead, we expect a LES technique to be able to simulate occurrence of flow unsteadiness and yet avoid numerical divergence at the same time.

Another problem associated with the theoretical basis behind the dynamic eddy diffusivity or dynamic mixed SGS models is that the derivation of the theory is only valid for strictly homogeneous turbulent flows. The smoothing (filtering or volume-averaging) procedure of the model lacks the ability to distinguish the real SGS turbulent fluctuation from inhomogeneous mean flow fields. Although this drawback can be alleviated by refining the grid at strongly inhomogeneous regions in a solution domain, in practice this requires too much computer resource. This is especially the case when the models are applied to simulate turbulent flows near a solid boundary. Therefore, one must find a way to separate spatial inhomogeneity from real turbulent fluctuations of a flow field in the SGS modelling. Otherwise, results of the LES will be inaccurate or grid-dependent, and the situation is worse when turbulence in the flow under consideration is not strong enough — a poor laminar-side asymptotic behaviour of the SGS model.

Finally, a problem which looks to be insignificant but may affect the final results of the LES of turbulent flows is how to determine Δ, the characteristic length scale of the volume average or the length scale of the smallest solvable fluctuation. Most

previous LES workers used the following expression:

$$\Delta = (\Delta x \Delta y \Delta z)^{\frac{1}{3}}.$$

Some others used expressions such as

$$\Delta = (\Delta x^2 + \Delta y^2 + \Delta z^2)^{\frac{1}{2}}$$

or

$$\Delta = \frac{\Delta x + \Delta y + \Delta z}{3}$$

where Δx *etc.* are the length scales of the averaging volume. However, if we acknowledge that the SGS Reynolds stress or SGS turbulent heat flux appearing in the discretized governing equations in finite difference form is a surface average rather than a volume average, it is more reasonable to define the Δ based on surface areas of the averaging volume. In this sense, Δ should have three values, one for each coordinate directions. Furthermore, time-stepping of numerical schemes requires that the governing equations be averaged over a small time step. By so doing, not only the high wave number but also the high frequency components are eliminated. Only a few people, such as Bedford *et al.* (1982) and Dakhoul (1983) have considered this effect in their derivation of the so called space-time filtering approach. The spatial wave number and temporal frequency of a fluctuation are related to each other. It is reasonable to expect that after a spatial smoothing, high frequency components of a fluctuation are also eliminated, and *vice versa*. Therefore, we can view the temporal average of the governing equations over a single time step as an additional volume average superimposed on the SGS volume average. If the characteristic length scale of the time-step average is greater, the expression for Δ should be based on the time-step rather than on the control volume geometry.

In summary of the above discussion, present techniques for the LES method need

to be improved in the following respects:

1) The technique should be developed as a combination of both the field quantity smoothing of the LES and the solution domain discretization of the numerical method. In this sense, the advantages of the volume averaging approach should be explored.

2) The SGS turbulent fluctuation enhances transport in terms of the SGS flux and SGS turbulent diffusion as well. The latter was ignored by the previous volume averaging approach of the LES. Identification and modelling of this mechanism in the LES is essential to the VAT.

3) Eddy diffusivity models are not appropriate for the LES of most flows with engineering and scientific significance. Dynamic models for the full-component SGS Reynolds stress and turbulent heat flux, and those for the SGS turbulent diffusion, should be developed.

4) Conventional dynamic SGS modelling methods are only strictly applicable to homogeneous flows which are not the case in engineering and scientific practice. An approach should be designed to remove inhomogeneity, a non-turbulence effect, from the SGS models.

5) Instability should be acknowledged as an important feature of turbulence and the LES technique should be able to simulate it by employing a special algorithm to avoid divergence.

6) The characteristic length scale of the LES should be re-defined to account for the surface averaging nature of the SGS Reynolds stress and turbulent heat flux, and the time average procedure used for time integration.

1.3 Room Airflow Prediction and LES Technique

The quality of indoor air is increasingly being recognised as an essential factor for the overall health and comfort of human beings since up to 90 percent of a typical person's time is spent indoors. Also, industry needs indoor air quality control for manufacturing, product storage, and research and development processes. Air conditioning has become more and more popular during the last two decades. Today, almost all commercial buildings in industrial countries have been air conditioned, and air conditioning has become one of the most significant factors in national energy consumption.

A successful and cost-effective air conditioning system is one that can maintain a healthy and comfortable indoor environment with adequate outdoor ventilation air and acceptable indoor air quality with a low energy index. Design of improved air conditioning systems has stimulated engineers' interest in improving knowledge about how ventilation air is distributed and how indoor contaminants are transported within buildings. The indoor space in a building is generally divided by internal walls into rooms of different size. A good knowledge of room airflow is a key point in understanding the indoor air motions in buildings. Therefore, it is necessary to provide the means to investigate air distribution in rooms. The nature and severity of indoor air quality, thermal comfort, and air conditioning load problems can be assessed by room air motion analysis. Effective prediction tools for room airflow may help a designer choose the optimum design from a number of possible alternatives.

Investigation of room airflow is mostly conducted by two approaches: experimental measurement and numerical simulation. Although it seems more accurate and reliable, the experimental measurement approach has many limitations. It requires a large investment in instrumentation, equipment, models for buildings, wind tunnel equipment, and personnel. The experimental measurement approach also takes a long time (often many weeks) to complete a study starting from model installation to data acquisition and post-processing. In contrast, an important advantage of the numeri-

cal simulation approach is the minimal investment, since only computer resources are required. Furthermore, the results of numerical simulation can be accessible within a few of days. Given the potential advantages of the numerical simulation approach, it is of critical importance that accurate numerical methods be developed which can be expected to yield realistic predictions of room airflow.

Experimental observation shows that airflow in a room of typical size is not laminar. Previous researchers tended to view such non-laminar flow as "fully developed turbulence", and simulated it with the RAM method. However, the fact is that most room airflow is not simply fully developed turbulence or even turbulence at all. Recent investigations tell us that most room airflow is actually a combination of the following kinds of flow: 1) unsteady laminar; 2) transitional states between laminar and turbulence; 3) local artificially induced turbulence; 4) exterior turbulence convected into the domain; 5) fully developed turbulence. One evidence of the complexity of room airflow is the existence of so called "multiple solutions" which means that, under specific conditions, room airflow shows different patterns in different observations (measurements). The phenomenon is likely to be explained as follows. The flow pattern in a room is determined by the eddy structure of the flow. Since room airflow is a combination of unsteady laminar and turbulent flow, there must be regions in the room where the flow is at the transition point. Whether or not, and to which regime a transition happens, are determined by the instantaneous eddy structure of the flow and local Reynolds number. Once a transition occurs, a new eddy structure and a new distribution of local Reynolds number will be set up, which will determine the next transition, and so on. It should be noted that the laminar-turbulence transition is actually a nonlinear procedure. The critical Reynolds number corresponding to a transition from laminar to turbulence is higher than that corresponding to a transition from turbulence to laminar, a fact probably due to the "energy back-scatter" mechanism in the "energy cascade". Thus, once a transition has happened, it is impossible to resume the pre-transition status even if the new distribution of local Reynolds number allows it. A small disturbance itself has limited effect on the scale structure of the flow in a room, but can affect the local Reynolds number, and con-

sequently reverse the transition direction, and ultimately change the eddy structure of the flow. Thus, the phenomenon of "multiple solutions" is nothing but a typical feature of flows of hybrid regime.

In the sense of the above discussion, room airflow is a typical kind of flow, the numerical simulation of which is beyond the capacity of the RAM method. Therefore, an important objective of the present study is to apply the developed volume average technique of LES to room airflow prediction.

1.4 Scope of Study and Thesis Outline

Having identified some drawbacks of the present techniques for the LES, in this study a so-called Volume Average Technique (VAT) for turbulent flow simulation is developed. The VAT couples the volume averaging approach of the LES with the solution domain discretization approach of the finite volume method. All formulations are re-derived in the context of the volume averaging approach and in framework of the finite-volume method. Additionally, a new functional scale similarity SGS model is proposed which is expressed in terms of the sub-grid and test-grid volume averaged fields. Since it is dynamical in nature, no empirical coefficient is applied in the functional scale similarity SGS model. The model gives up the eddy diffusivity hypothesis, thus over-backscatter of energy can be avoided. Since time averaged fields are involved, the functional scale similarity SGS model is still valid for flows with strong inhomogeneity.

Realization of the LES of flows relies strongly on the efficiency of the numerical scheme applied. In the present study, a new collocated finite-volume scheme for 3-D incompressible viscous flow is developed based on the conventional SIMPLE and fractional-step methods. The scheme is shown to be convenient and efficient when applied with the VAT. After some benchmark tests, the VAT is finally applied to

predict the flow in a room of generic geometrical and air-conditioning configuration. The outline of the thesis is as follows:

In Chapter 2, the current state of the art in turbulent flow simulation is reviewed. The scope of discussion is limited to the LES methods and emphasises the characteristics of previously developed SGS modelling methods.

In Chapter 3, the formal theory of the VAT for turbulent flow simulation is developed. The main aspects covered are:

1) Derivation of finite difference form discretized governing equations with the SGS related terms expressed in terms of control volume surface averages.

2) Development of the functional scale similarity models for both the SGS Reynolds stress and SGS turbulent heat flux.

3) Derivation of the models for the SGS turbulent diffusion term through an analogy to molecular diffusion.

In Chapter 4, numerical methods associated with the VAT for turbulent flow simulation are developed. The most significant aspect covered in this chapter is the collocated scheme for 3-D viscous incompressible flow, which combines the techniques of the SIMPLE scheme, the fractional step method, the QUICK scheme, and the ADLGS solver. Other aspects covered are the numerical approaches for handling boundary conditions, and the numerical schemes for the test-grid volume average and time average.

In Chapter 5, 2-D and 3-D lid-driven cavity flows at $Re = 1000$ and $Re = 400$, and a 3-D buoyancy-driven cavity flow at $Ra = 10^6$ are considered as model problems for testing the numerical schemes developed. The flows are believed to be laminar, and no SGS models are applied.

In Chapter 6, two benchmark flows, *i.e* a lid-driven cavity flow at $Re = 10000$ and a buoyancy-driven cavity flow at $Ra = 10^{10}$, both of which are in the regime of

turbulence, are simulated using the VAT. The results are compared with those from previous experimental and/or numerical investigations for the same flows.

In Chapter 7, as an application of the VAT for turbulent flow simulation, a case of room airflow in an enclosed air-conditioned room with a wall-mounted cooling inlet and an opposing outlet is predicted. Comparisons are made between the results of the simulation and their counterparts from a published experimental investigation of the same room airflow.

Finally, in Chapter 8, the conclusions of the study are presented, along with a summary of its contributions as well as a set of recommendations for future research.

The ultimate objective of the present study is to enable the LES method to be applied to the simulation of engineering turbulent flows with moderate complexity using computer resources provided by a typical workstation or high performance personal computer.

Chapter 2

Literature Review

2.1 Introduction — A Short History

As was pointed out in the previous chapter, LES is probably the only promising method we can apply confidently to simulate complex turbulent flows found in engineering application. Nevertheless, development of the LES method has been strongly related to the sophistication of computers available. Compared with the RAM methods, the LES method needs still larger computer memory and longer CPU time due to the 3-D and time-dependent nature of the computations. This can explain why the LES method has so short a history of development (approximately three decades).

The first application of the LES method was made by meteorologists who tried to simulate global weather patterns for a long time period. A typical 3-D simulation of atmospheric circulation which can be viewed as a real LES of turbulent flow in today's sense is that of Smagorinsky (1963). This paper presented the Smagorinsky

SGS model that has since been used extensively. The first computation of a flow of engineering interest, and also the first use of the name "Large Eddy Simulation", was the simulation of a channel flow by Deardorff in 1970. In this pioneering work, Deardorff laid down most of the foundations of the LES method.

Improvements in Deardorff's method were made by Schumann (1973) and Leonard (1974). They introduced, respectively, a strict theory of the volume averaging approach and that of the filtering approach for the LES method. Since then, research of the LES method has been divided into two categories. The volume averaging approach is represented early by Schumann (1975) and Grotzbach (1977,1978). The latter and his group at Karlsruhe have subsequently extended the method to the computation of annular flows, the inclusion of heat transfer, and the inclusion of the effect of buoyancy. The other approach, *i.e.* the filtering approach is represented by the Stanford group, *e.g.* Mansour *et al.* (1979), Moin *et al.* (1978), and Ferziger (1977). The flows simulated in late 70's and early 80's by the Stanford group are those with at least one homogeneous direction, such as mixing layers and channel flows. Since then, the filtering approach has been broadly used by most LES research groups all over the world. Unfortunately, people have not paid as much attention to the volume averaging approach as it deserves.

The basic idea of LES can be explained more simply in wave number space. In this context, the LES can be performed by simulating the Fourier transformed Navier-Stokes equation with its wave number representation truncated ($k < k_c$). Due to the complexity of the equation, direct application of this so called spectral LES approach is limited to homogeneous isotropic flows, which have little significance in engineering practice. Nevertheless, the approach can be applied to the development of SGS models by using the elegant two-point correlation theories of turbulence.

Almost from the beginning of the use of the LES method, it was realized that developing better models for treating the small scales (SGS models) or at least understanding the models that are in use is of critical importance. The 1980's and early

1990's saw the development of several different versions of SGS model, which almost dominated the research in the field during that period. The most important achievements in the development of the SGS models, from the point of view of engineering applications, are: 1) the scale similarity model proposed by Bardina *et al.* (1980) and 2) the dynamic eddy viscosity model proposed by Germano *et al.* (1991). However, due to an intrinsic deficiency, the pure form of the scale similarity model (as opposed to its mixed form) has not been broadly accepted since its publication. On the other hand, the dynamic eddy viscosity model has been extended and extensively applied in the LES community.

Despite the notable advancements made since 1963, at present the LES method still cannot be considered an engineering tool. To date, very rarely has the LES method been applied to actual engineering configurations, such as flows in complex geometries and at high Reynolds or Rayleigh numbers. This chapter reviews the developed techniques of the LES method in order to give an overview of the current state. Some information comes from review papers by Ferziger (1983), Rogallo & Moin (1984), Grotzbach (1986), Yoshizawa (1986), Aldama (1990), Ferziger (1993), Piomelli (1993a), Lesieur *et al.* (1993), and Lesieur & Metais (1996). The discussion is limited to the LES method for incompressible Newtonian flows governed by the Navier-Stokes equations, since the effects of buoyancy, compressibility, density stratification, *etc.* introduce new physical phenomena that increase the simulation difficulty in degree rather than kind. Both positive and negative features of the present techniques of the LES method, specifically the ones that have been pointed out in the previous chapter, are described in detail and some comments on them are given. In this sense, the present chapter can be viewed as an extension of section 1.2.

2.2 Rationale of LES

All numerical simulation of turbulent flows including LES is based on the assumption that instantaneous flow variables satisfy the Navier-Stokes equations. Justification of describing turbulent flows by the Navier-Stokes equation stems from the fact that the smallest scale of turbulence is still several orders larger than the molecular scale of the fluid, which has been accepted as an axiom among fluid dynamicists. The Navier-Stokes and continuity equations for a viscous incompressible fluid are written as

$$\dot{U}_i + (U_i U_j)_{,j} = -\frac{1}{\rho_0} P_{,i} + \nu U_{i,jj} \tag{2.1}$$

and

$$U_{i,i} = 0 \tag{2.2}$$

where U_i represents the instantaneous velocity component in the ith direction; P, the instantaneous pressure; and ρ_0, a constant reference density.

The rationale of the LES method relies on the fact that simulation of turbulent flows by directly solving equations (2.1) and (2.2) is practically impossible. This fact can be explained using the Kolmogoroff theory of turbulence (refer to Orszag 1977). According to the Kolmogoroff theory of homogeneous turbulence, the Kolmogoroff micro scale η is defined by

$$\eta = O[(\nu^3/\epsilon)]^{\frac{1}{4}} \tag{2.3}$$

where ϵ denotes the energy dissipation rate per unit mass and ν is the kinematic viscosity of the fluid. On the other hand, experiments show that ϵ is mostly determined by the characteristic velocity V and characteristic length L of the largest eddies in a given turbulent flow, *i.e.*

$$\epsilon = O(V^3/L). \tag{2.4}$$

From equations (2.3) and (2.4), we have

$$L/\eta = O(Re^{3/4})$$

where $Re = VL/\nu$ is the Reynolds number of the flow. Thus N, the number of mesh points required to directly simulate the turbulent flow, can be estimated as:

$$N = O[(L/\eta)^3] = O(Re^{9/4}). \tag{2.5}$$

In engineering applications, the Reynolds number is usually very large. For a flow at $Re = 10^6$, approximately 10^{13} grid points are needed, which is definitely beyond the memory capacity of any existing computer, and those in the foreseeable future. Even worse in this regard is that a more precise data type (*e.g.* four-word representation of a real number) with smaller machine round-off error may be necessary to handle the increased quantity of calculations associated with large numbers of grid cells. Furthermore, from the point of view of numerical stability, the use of an extremely fine grid should be matched with an extremely small step for time advancement (the CFL condition), which will consequently lengthen simulation time to an intolerable degree.

In order to reduce the need for computer resources, in LES only the large scale eddies in a flow are simulated directly. The justification for doing this is supported by the following facts summarised by Ferziger (1983). Firstly, the large eddies interact strongly with the mean flow and are responsible for most of the transport of mass, momentum, and energy. The structure of large eddies is strongly dependent on the geometry of the flow, so they are highly anisotropic. By contrast, the small scale eddies are much more universal, nearly isotropic. The main effect of small eddies is to dissipate fluctuations of field quantities, which affects the mean properties only slightly. The small eddies seem to be created and destroyed much more quickly. The conclusion is that the large eddies are more important and also more difficult to model

in a flow than the small eddies, which provides the rationale of the LES. A qualitative comparison between the LES and DNS methods may give us some insight: the DNS is a simpler "brute force" method, while the LES is a more complex but "artful" scheme.

2.3 Coarse-graining Procedure in LES

The coarse-graining or smoothing procedure in LES splits the instantaneous field quantities of a flow into the directly resolved parts and the unsolved SGS parts. To this end, two approaches, the filtering and the volume averaging approaches have been proposed. In this section, the formalism of these two approaches is examined in detail.

2.3.1 Filtering Approach

Leonard's (1974) definition of space filtering is as follows:

$$\tilde{\Phi} = \iiint_{-\infty}^{\infty} G(\mathbf{x} - \mathbf{x}')\Phi(\mathbf{x}')d^3\mathbf{x}' \tag{2.6}$$

where G is a suitably defined spatial filter function. For convenience, the above operation can be written in the contracted form

$$\tilde{\Phi}(\mathbf{x}) = G(\mathbf{x}) * \Phi(\mathbf{x}). \tag{2.7}$$

By taking the space Fourier transform of the above equation and using the convolution theorem, we obtain the expression of the filtering in wave number space as

$$\tilde{\phi}(\mathbf{k}) = g(\mathbf{k})\phi(\mathbf{k}) \tag{2.8}$$

where ϕ and g are, respectively, the space Fourier transforms of Φ and G, *e.g.*

$$\phi(\mathbf{k}) = \iiint_{-\infty}^{\infty} and\Phi(\mathbf{x}) \exp(-i\mathbf{k}\cdot\mathbf{x}) d^3\mathbf{x}$$

where $i = \sqrt{-1}$. We can represent any 3-D filter function in terms of a product of 1-D filter functions in each direction, so that

$$G(\mathbf{x}) = \prod_{j=1}^{3} G_j(x_j)$$

or in wave number space

$$g(\mathbf{k}) = \prod_{j=1}^{3} g_j(k_j)$$

where G_j and g_j are, respectively, the 1-D, j-direction filter functions in physical and wave number space.

Several researchers have investigated the properties of different 1-D filters in connection with their applicability to the LES method (Leonard, 1974; Kwak *et al.*, 1975; Clark *et al.*, 1979; Babajimopoulos and Bedford, 1980; Bedford and Dakhoul, 1982). The most commonly applied 1-D filters include: 1) the ideal filter; 2) the Gaussian filter; and 3) the box filter (also known as the top-hat filter). Their mathematical expressions in both physical and wave number space were given by Aldama (1990) as discussed below.

The 1-D ideal filter is originally defined in wave number space as

$$g_j(k_j) = \begin{cases} 1 & \text{for } |k_j| < 2\pi/h \\ 0 & \text{for } |k_j| > 2\pi/h \end{cases} \tag{2.9}$$

which in physical space takes the form

$$G_j(x_j) = \frac{\sin(2\pi x_j/h)}{\pi x_j}. \tag{2.10}$$

In the case of the 1-D box filter we have

$$G_j(x_j) = \begin{cases} 1/h & \text{for } |x_j| < h/2 \\ 0 & \text{for } |x_j| > h/2 \end{cases} \tag{2.11}$$

or in wave number space

$$g_j(k_j) = \frac{\sin(hk_j/2)}{hk_j/2}. \tag{2.12}$$

Finally, for the Gaussian filter

$$G_j(x_j) = \sqrt{6/\pi}\frac{\exp[-6(x_j/h)^2]}{h} \tag{2.13}$$

and

$$g_j(k_j) = \exp[-\frac{h^2k_j^2}{24}]. \tag{2.14}$$

In equations (2.9) through (2.14), h represents the characteristic filter width. Plots of the dimensionless 1-D filters, $hG(x_j)$, and the corresponding Fourier transform, $g(k_j)$, are shown in Figures 2.2 and 2.1 for the ideal filter, in Figures 2.3 and 2.4 for the box filter, and in Figures 2.5 and 2.6 for the Gaussian filter. All of the above filters have been applied in previous LES work.

It can be shown through "integration by parts" that the filter operator and spatial, as well as temporal, derivative are commutable (Leonard, 1974). Thus, the filtered Navier-Stokes equations are

$$\dot{\tilde{U}}_i + \widetilde{U_i U_j}_{,j} = -\frac{1}{\rho_0}\tilde{P}_{,i} + \nu \tilde{U}_{i,jj} \tag{2.15}$$

and

$$\tilde{U}_{i,i} = 0. \tag{2.16}$$

The difficulty comes from the nonlinear term, *i.e.* the second term on the LHS of equation (2.15), which is handled by introducing the following velocity decomposition:

$$U_i = \tilde{U}_i + u_i'$$

where u_i' represents the SGS components of the velocity field U_i. Thus, the term can be expressed as

$$\widetilde{U_i U_j} = \tilde{U}_i \tilde{U}_j + (\widetilde{\tilde{U}_i \tilde{U}_j} - \tilde{U}_i \tilde{U}_j) + (\widetilde{\tilde{U}_i u_j'} + \widetilde{u_i' \tilde{U}_j}) + \widetilde{u_i' u_j'} \tag{2.17}$$

or briefly

$$\widetilde{U_i U_j} = \tilde{U}_i \tilde{U}_j - L_{ij} - C_{ij} - \tau_{i,j} \tag{2.18}$$

where L_{ij}, C_{ij}, and τ_{ij} are, respectively, the Leonard term, the cross-correlation term, and the SGS Reynolds stress term. Substituting the expression (2.18) into the filtered Navier-Stokes equation (2.15), we have

$$\dot{\tilde{U}}_i + (\tilde{U}_i \tilde{U}_j)_{,j} = -\frac{1}{\rho_0}\tilde{P}_{,i} + (\nu \tilde{U}_{i,j} + L_{ij} + C_{ij} + \tau_{ij})_{,j}\,. \tag{2.19}$$

Theoretically, only the C_{ij} and τ_{ij} in equation (2.19) are related to the SGS motions of the flow and should be modelled to close the solution system; the L_{ij} is calculable from

the resolved fields. However, since it is related to filtering of the product of two filtered velocity components, the term is difficult to calculate numerically. Several different approaches were taken toward this issue, which are listed below. The modelling methods for the C_{ij} and τ_{ij} appearing in equation (2.19) will be discussed later in this chapter.

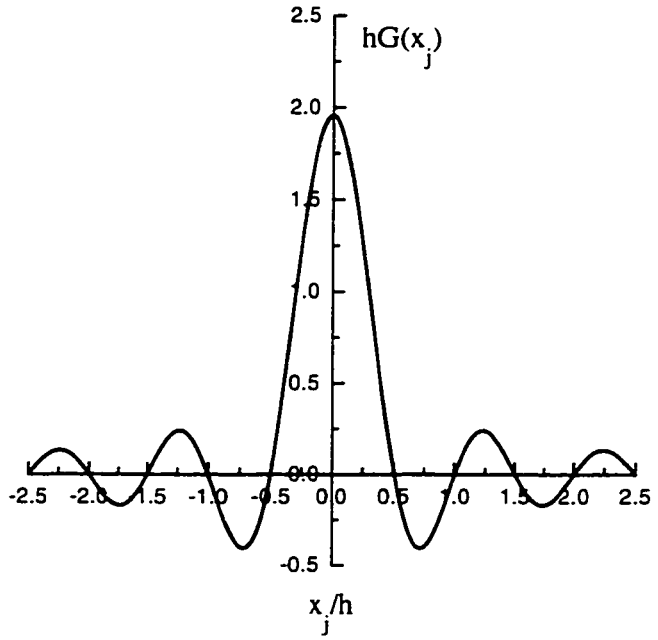

Figure 2.1: 1-D ideal filter in physical space

1) Some investigations suggest that the term is responsible for only a small amount of energy transfer between the large and small scales and can be swamped by the numerical errors inherent in the finite difference representation. Thus, the term can be neglected or lumped with the SGS models for the C_{ij} and τ_{ij}. Then the numerical schemes developed for solving the instantaneous fields of the flow can be directly applied to solving the filtered fields. This approach has been widely adopted in the LES of wall-bounded flows.

2) Leonard (1974) showed that the term L_{ij} (named after him) removes significant energy from the large scales and should probably not be lumped with the SGS models.

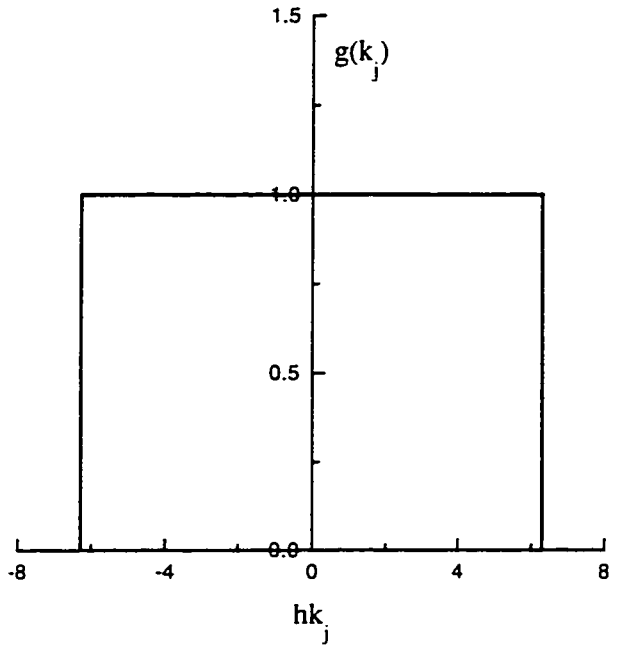

Figure 2.2: 1-D ideal filter in wave number space

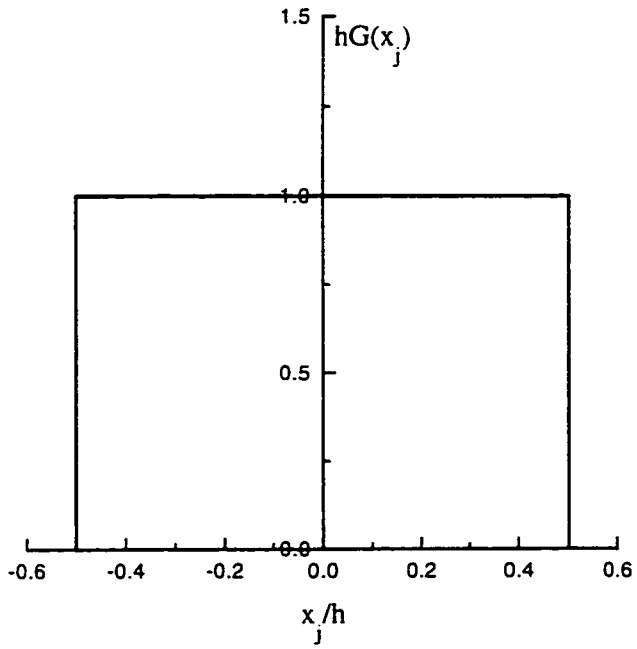

Figure 2.3: 1-D box filter in physical space

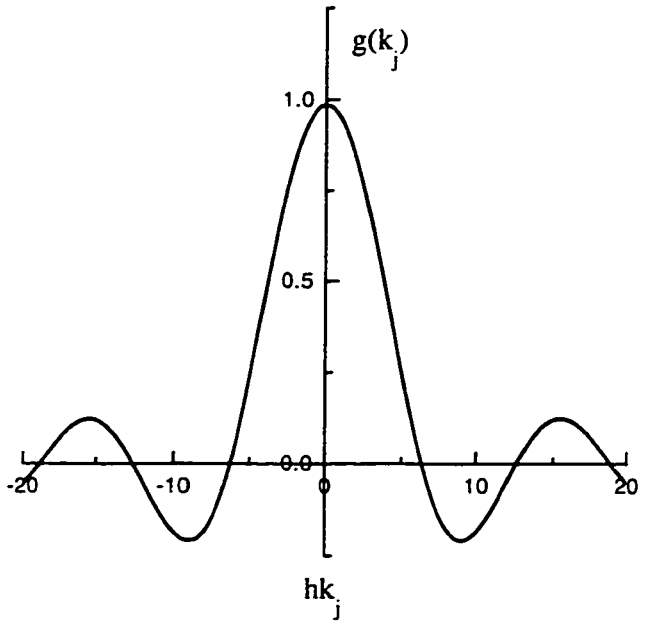

Figure 2.4: 1-D box filter in wave number space

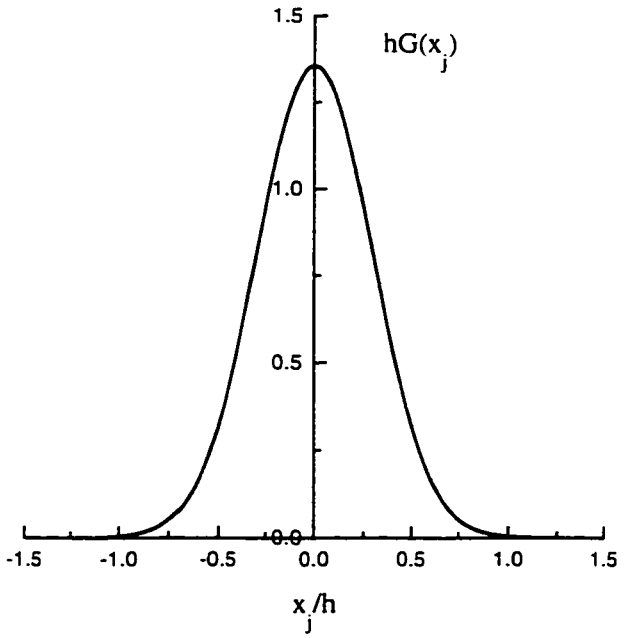

Figure 2.5: 1-D Gaussian filter in physical space

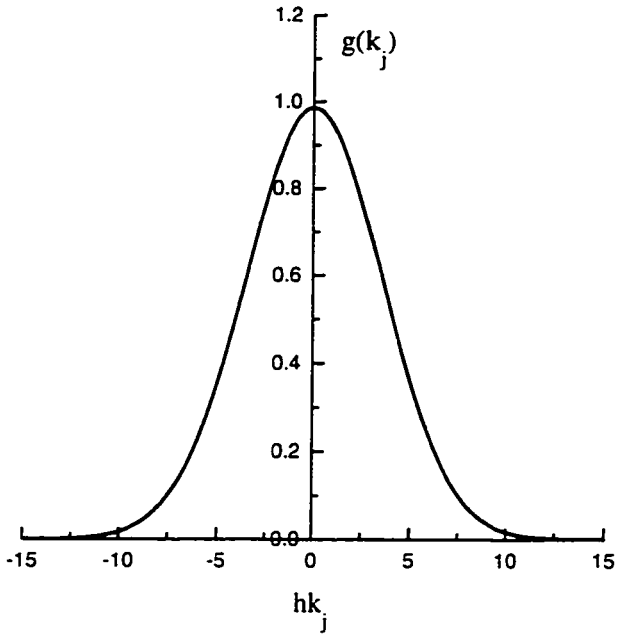

Figure 2.6: 1-D Gaussian filter in wave number space

He proposed to express it in terms of a Taylor series expansion as

$$-L_{ij} \approx \frac{(\tilde{U}_i\tilde{U}_j)_{,ij}}{2} \iiint_{-\infty}^{\infty} |\mathbf{x}'|^2 G(\mathbf{x}') d^3\mathbf{x}'$$

At low Reynolds number, Clark *et al.* (1979) found this approach to be quite accurate when compared with values from a DNS. One drawback of the above approximation of the Leonard term is that a second order derivative appears inside another derivative in the filtered governing equation, so that a third order differential equation results. This fact will cause problems at the boundaries, due to the lack of sufficient boundary information. Applications of this approach were limited to the LES of turbulent flows with homogeneous directions.

3) As an alternative to modelling the Leonard term, one could treat the filtered large scale nonlinear advective term, $\widetilde{\tilde{U}_i\tilde{U}_j}$, explicitly (in the time stepping sense). In doing this, the term is first Fourier-transformed into a product of g, the filtering function in wave number space, and $\mathcal{F}(\tilde{U}_i\tilde{U}_j)$, the Fourier transform of $\tilde{U}_i\tilde{U}_j$. After

calculating the product, the required value of the term can be obtained by inverting the Fourier transform. This approach has been favoured in most of the early LES research carried out at Stanford (Ferziger *et al.*, 1977; Mansour *et al.*, 1979; Bardina *et al.*, 1980; McMillan *et al.*, 1980). However, the computational procedure for this approach is too complicated, and there has been no evidence that it is more accurate than the previous approach.

Although some researchers (*e.g.* Rogallo and Moin, 1984) claim that when the ideal filter is employed, the Leonard term will vanish identically, *i.e.*, $\widetilde{\tilde{U}_i\tilde{U}_j} = \tilde{U}_i\tilde{U}_j$, the validity of this argument is questionable. Using the ideal filter, one can only reach the equality $\tilde{\tilde{\Phi}} = \tilde{\Phi}$ rather than the required condition, $\widetilde{\tilde{\Phi}_1\tilde{\Phi}_2} = \tilde{\Phi}_1\tilde{\Phi}_2$. The appearance of the above contradictory positions is probably due to the fact that people deal with the issue separately without regarding the effect of numerical errors. Theoretically, no matter what kind of filter is applied, the Leonard term does exist and represents a high wave number (or SGS) contribution in correlations between large scale fields. It can be shown that the length scale of this high wave number portion ranges from h/2 to h. In $\widetilde{\tilde{U}_i\tilde{U}_j}$, the SGS portion has been removed, while in $\tilde{U}_i\tilde{U}_j$, which is retained in the convection term on the LHS of equation (2.19), the SGS portion is still included. Thus, the Leonard term is introduced to compensate for the above discrepancy. However, from a numerical point of view, if we use a grid cell with length scale similar to h, we actually are not able to capture the effect of the above mentioned high wave number portion in the calculation of $\tilde{U}_i\tilde{U}_j$. In other words, with the coarse grid, we actually obtain the value of $\tilde{U}_i\tilde{U}_j$ without the SGS portion, which is equivalent to $\widetilde{\tilde{U}_i\tilde{U}_j}$. Thus, in this case the Leonard term can be neglected or, as was referred to before, be swamped by numerical errors.

Two apparent features of the filtering approach are: 1) that the governing equations for the large scale fields are still differential equations which are valid continuously over the entire solution domain, and 2) that the characteristic width of the filter can be selected freely. Both features are very attractive from a theoretical point of view. However, they have less significance from a numerical point of view. To

be solved numerically, the differential equations governing the filtered fields should first be discretized. The discretization procedure may complicate the situation since it is also a coarse-graining procedure. Dissociation of the filtering and numerical coarse-graining procedures from each other can only occur when the length scale of a grid cell is much smaller than the characteristic width of filtering. However, too small a ratio of the characteristic width of filtering over the length scale of the grid cell will complicate the integral calculation and deteriorate locative sensitivity of the approach. In fact, the range of the characteristic width of the filter to be selected is very limited. It must not be less than the length scale of the grid cells, because numerical schemes lack the ability to capture effects of eddies smaller than the grid cells. On the other hand, in order to capture strong inhomogeneity of the flow in the near wall region, the characteristic width of the filter must not be greater than twice the grid cell length scale near solid boundaries. In practice, using a filter with the characteristic width equal or close to the grid length scale is probably the best selection.

2.3.2 Volume Averaging Approach

Let us consider the other coarse-graining approach, *i.e.* volume averaging. This approach is based on the recognition that we shall be solving the equations numerically. Thus, it makes sense to use an approach that arrives at the discretized equations as quickly as possible.

In the volume averaging approach, one first divides the flow region into many rectangular subregions, SR, each with side h_i (i=1,2,3). Schumann (1974) defined the volume average of a field quantity Φ as

$$\tilde{\Phi} = \frac{1}{V} \iiint_{SR} \Phi dV \tag{2.20}$$

where $V = h_1 h_2 h_3$ is the volume of the subregion. It is interesting to rewrite equation (2.6) for the case of the box filter with characteristic width $\mathbf{h} = \{h_1, h_2, h_3\}$, as

$$\tilde{\Phi} = \frac{1}{V} \iiint_{|\mathbf{x}-\mathbf{x}'|<\mathbf{h}} \Phi(\mathbf{x}') d^3\mathbf{x}'. \tag{2.21}$$

Comparison of equation (2.20) and (2.21) shows that the volume average presents only one value for each subregion, while the values obtained by box filtering are position-dependent and distributed continuously throughout the subregion. However, the volume average and the box filtering are related at the centre of the subregion where the value of box filtering is identical to that of the volume average.

Application of the volume average (2.20) to the Navier-Stokes and continuity equations (2.1,2.2) provides the following finite difference equations:

$$\dot{\overbrace{U_i}} + \delta_j \overbrace{U_i U_j}^{j} = -\frac{1}{\rho_0} \delta_i \overbrace{P}^{i} + \nu \delta_j \overbrace{U_{i,j}}^{j} \tag{2.22}$$

$$\delta_i \overbrace{U_i}^{i} = 0 \tag{2.23}$$

where $\overbrace{\Phi}^{i}$ denotes an average of the field Φ over the subregion surface normal to the x_i-direction, *e.g.*

$$\overbrace{\Phi}^{1} = \frac{1}{h_2 h_3} \iint \Phi dx_2 dx_3$$

and $\delta_i \overbrace{\Phi}^{i}$ is the centre difference of the surface average,

$$\delta_i \overbrace{\Phi}^{i} = \frac{1}{\Delta x_i} (\overbrace{\Phi}^{i+\frac{1}{2}} - \overbrace{\Phi}^{i-\frac{1}{2}}).$$

Shumann (1974) introduced the velocity decomposition based on surface average, *i.e.*

$$U_i = \overbrace{U_i}^{j} + u_i' \tag{2.24}$$

and expressed the surface averaged velocity component products appearing in equation (2.22) as

$$\overbrace{U_i U_j}^{j} = \overbrace{U_i}^{j}\overbrace{U_j}^{j} + \overbrace{u_i' u_j'}^{j} = \overbrace{U_i}^{j}\overbrace{U_j}^{j} + \tau_{ij}. \tag{2.25}$$

Only the second term on the RHS of (2.25), *i.e.* the SGS Reynolds stress, should be modelled in the simulation. Thus, equation (2.22) was rewritten as

$$\dot{\overbrace{U_i}}^{j} + \delta_j(\overbrace{U_i}^{j}\overbrace{U_j}^{j}) = -\frac{1}{\rho_0}\delta_i \overbrace{P}^{i} + \delta_j(\tau_{ij} + \nu \overbrace{U_{i,j}}^{j}). \tag{2.26}$$

The volume averaging approach was employed after Schumann by several LES researchers such as Antonopoulos (1981) and Leslie (1982), and some realistic results were obtained.

A drawback of the above derivation of Schumann (1974) is the application of the surface average based decomposition (2.24) to flow fields which are actually volume averaged. A consequence of this inconsistency is that the turbulent effects due to flow fluctuations across the averaging surfaces cannot be captured. However, the problem is surmountable if a volume average based decomposition and the linear interpolation method is applied instead. Since the characteristic length scale of the volume average is similar to that of the grid cell in the volume averaging approach, the Leonard term will vanish due as pointed out in section 2.3.1. A detailed description of the volume average based decomposition procedure is given in Chapter 3.

2.4 SGS Modelling Methods

In this section, we focus our attention on the modelling methods for the SGS-related terms, *i.e.* the SGS Reynolds stress τ_{ij} and the cross-correlation terms[1]. Unlike the turbulence models of the RAM methods, the role of the SGS models in the LES is not to provide the turbulent statistics of a flow, but to prevent the omission of the small scales from spoiling the calculation of the large scales from which the large scale turbulent statistics are taken. From the point of view of energy conservation, the SGS models should provide the correct magnitude of the energy transfer between the resolved and sub-grid scales. This transfer is usually from resolved to sub-grid scales but may be reversed, *e.g.* near solid walls, where the small productive eddies are not solved directly.

Although Clark *et al.* (1979) found that the measured cross-correlation terms drain significant energy from the resolved scales, there are actually few methods for reaching an isolated model for them. The cross-correlation terms are either lumped with the Leonard terms using a Taylor series expansion (Clark *et al.* 1979) or lumped with the SGS Reynolds stress using an eddy diffusivity model with adjustable coefficients. Aldama (1990) has identified the inappropriateness of expanding the cross-correlation terms with a Taylor series expansion. The reason is that the highly fluctuating nature of u_i' prevents it from being represented by a Taylor series in the scale of the filter width. Thus, an accurate modelling method for the cross-correlation terms is still not available.

Justification for lumping the cross-correlation terms with the SGS Reynolds stress or equivalently assuming them to be zero may be explained as follows. Physically the cross-correlation terms represent correlations between large scale fields and SGS fluctuations. It is believed that, in a turbulent flow, only the fluctuations with similar length scales are correlated with each other via a procedure of "vortex stretching".

[1] It is implicitly assumed that the discussion of the cross-correlation terms is in the context of the filtering approach in this section

Only the high wave number modes in the solvable fields and the low wave number modes in the SGS fluctuations are correlated with each other, and the correlations represent a main contribution to the cross-correlation terms. Let's assume that the dominant length scale of the low wave number modes in the SGS fluctuations is Δ_l which should be a bit lower than Δ (the characteristic width of the filter), while the dominant length scale of the high wave number modes in the solvable fields is Δ_L which should be a bit higher than Δ. Thus, it can be shown (see Appendix A.1) that the product of these two dominant modes has modes of length scales $\frac{\Delta_L\Delta_l}{\Delta_L-\Delta_l}$ and $\frac{\Delta_L\Delta_l}{\Delta_L+\Delta_l}$. If Δ_l and Δ_L are close to each other, the mode with length scale $\frac{\Delta_L\Delta_l}{\Delta_L+\Delta_l}$ is absolutely in the SGS range and will vanish when filtered (with the characteristic length scale Δ) again. Therefore, the correlation terms have only low wave number modes with approximately a very large length scale $\frac{\Delta_L\Delta_l}{\Delta_L-\Delta_l}$. These extremely large modes have negligible effect on local or instantaneous features of the flows under consideration.

The review thereafter in this section will focus on modelling methods for the SGS Reynolds stress τ_{ij}.

For historical reasons, development of the modelling method for the SGS Reynolds stress follows the development of the Reynolds average models. First of all, like the conventional Reynolds stress, it is not difficult to derive a set of equations describing the dynamical behaviour of τ_{ij} using equation (2.17). The following equation is from Ferziger (1983):

$$\dot{\tau}_{ij} + (\tau_{ij}\tilde{U}_k)_{,k} = -[(L_{ik} + \widetilde{\tau_{ik}})\tilde{U}_{j,k} + (L_{jk} + \widetilde{\tau_{jk}})\tilde{U}_{i,k}]$$

$$+ \frac{\tilde{P}}{\rho_0}[(u'_{i,j} \widetilde{+u'_{j,i}}) - (\tilde{U}_{i,j} \widetilde{+\tilde{U}_{j,i}})] - 2\nu[u'_{i,k}\widetilde{u'_{j,k}} - \tilde{U}_{i,k}\widetilde{\tilde{U}_{i,k}}] + D \qquad (2.27)$$

where the cross-correlation terms C_{ij} have been lumped into τ_{ij}, and the terms on the RHS are, respectively, the production, the redistribution, and the dissipation. The last term, D, represents many diffusion terms which are not written explicitly. All of

the terms in equation (2.27) are analogous to terms in the Reynolds stress equations of second-moment closure modelling. Equation (2.27) also serves as the theoretical basis for most SGS models developed.

2.4.1 Eddy Diffusivity SGS Models

The idea of diffusivity models for LES is similar to those for the RAM method, *i.e.* to lump the SGS turbulence effect, mainly that from the SGS Reynolds stress, into the SGS eddy diffusivity, which is referred to as the eddy viscosity (ν_t) for the momentum equation. A mathematical representation of the model is as follows:

$$\tau_{ij} = -\widetilde{u_i' u_j'} = 2\nu_t \tilde{S}_{ij} - \frac{1}{3}\delta_{ij}\widetilde{u_k' u_k'}. \tag{2.28}$$

With equation (2.28), the Reynolds stress term in equation (2.19) can be absorbed into the diffusion term by combining the eddy viscosity with the molecular kinematic viscosity.

Like the conventional eddy diffusivity models for the RAM method, the eddy diffusivity SGS models can be "derived" from equation (2.27) under the "production equals dissipation" argument and other conditions. The most important one of these conditions is the scale separation between the resolved and SGS eddies, which can only be satisfied at a very high local Reynolds number. Therefore, no matter how accurate the method employed to calculate the eddy viscosity (ν_t), a fatal drawback of the eddy diffusivity SGS models is that they are only valid for fully developed, unbounded turbulent flows.

The eddy diffusivity SGS models build up a one-to-one correlation between the SGS Reynolds stress tensor and the resolvable scale strain rate tensor. However, the analysis of the data obtained from DNS fail to display such a correlation (Clark *et*

al., 1979 and McMillan & Ferziger, 1980). Recently, Lui *et al.* (1994) also showed poor correlation between these two tensors by using experimental data taken in the far field of a turbulent round jet at a much higher Reynolds number.

However, probably due to the lack of any other option, at present the eddy diffusivity SGS models are still widely applied. A comment by Ferziger (1983) summarises well the situation:

The results (of the LES) *shows that eddy viscosity models are rather poor and, in fact, they become poorer when there is mean strain and/or shear in the flow. However, it is not easy to find more accurate models ..., so we may be forced to use eddy viscosity models until something better is developed.*

In the present section, the SGS eddy diffusivity models of Smagorinsky and Schumann are reviewed.

2.4.1.1 Smagorinsky's SGS Models

The first eddy diffusivity SGS model was proposed by Smagorinsky in 1963. To parameterise the SGS Reynolds stress, he related the eddy viscosity directly to the characteristic width of the filter Δ and the magnitude of the resolved stain rate tensor as follows:

$$\nu_t = C_\nu \Delta^2 |\tilde{S}| \tag{2.29}$$

where

$$|\tilde{S}| = (2\tilde{S}_{ij}\tilde{S}_{ij})^{1/2}; \quad \tilde{S}_{ij} = \frac{\tilde{U}_{i,j} + \tilde{U}_{j,i}}{2}$$

and C_ν is a constant coefficient.

Generally, C_ν is problem-dependent and should be determined empirically by using flow field data from either an experiment or a direct numerical simulation. In LES of decaying isotropic turbulence, Shaanan *et al.* (1975), Ferziger *et al.* (1977), and Antonopoulos-Domis (1981) obtained values of $\sqrt{C_\nu}$ ranging from 0.19 to 0.24 by

matching the computed energy-decay rate to the experimental data of Comte-Bellot & Corrsin (1971). For the same turbulence (lower Reynolds number), Clark *et al.* (1979) and McMillan & Ferziger (1979) gave comparable values of $\sqrt{C_\nu}$ using flow field data generated by DNS.

It has been observed (Kolmogoroff, 1941a,b) that, at very high Reynolds number, a so called inertial subrange of wave numbers exists where the effect of viscous dissipation is negligibly small compared with the flux of energy transferred by inertial effects. Thus in the inertial subrange, the 3-D energy spectrum of turbulence $E(k)$ is solely related to ϵ, the dissipation rate of turbulent kinetic energy. By using dimensional analysis, one can obtain the famous $-5/3$ Kolmogoroff spectral law as follows,

$$E(k) \simeq K_0 \epsilon^{2/3} k^{-5/3}. \tag{2.30}$$

If the characteristic width of the filter Δ lays within the inertial subrange, one can take advantage of equation (2.30) to calculate the coefficient C_ν analytically. This fact was first recognised by Lilly (1966) who estimated ϵ as

$$\epsilon \simeq 2\nu_t \int_0^{\pi/\Delta} k^2 E(k) dk. \tag{2.31}$$

Furthermore, ϵ can also be estimated as

$$\epsilon \simeq \tau_{ij} \tilde{U}_{j,i} \tag{2.32}$$

by assuming that it is nearly equal to the energy production rate due to the SGS Reynolds stress and the resolvable scale shear. Combining equations (2.32) with (2.28) we have

$$\nu_t \simeq (\sqrt{C_\nu}\Delta)^{4/3} \epsilon^{1/3}. \tag{2.33}$$

Finally, substituting equations (2.33) and (2.30) into (2.31) we have

$$\sqrt{C_\nu} \simeq \frac{1}{\pi}\left(\frac{3K_0}{2}\right)^{-3/4}.$$

For a Kolmogoroff constant of $K_0 = 1.4$, this yields $\sqrt{C_\nu} \simeq 0.18$.

The above value of $\sqrt{C_\nu}$ does a good job for isotropic turbulence. However, for inhomogeneous shear flows many researchers, *e.g.* Deadorff (1970, 1971), have found that this value should be reduced by 50% or more. This is no surprise because the theory is based on isotropic turbulence. A review of this problem is given by Herring (1979).

Several alterations or modifications to Smagorinsky's SGS model have been proposed. For example, Leslie and Quarini (1979) replaced the magnitude of the velocity strain rate tensor $|\tilde{S}|$, in equation (2.29) with its ensemble average $\overline{|\tilde{S}|}$. Kwak *et al.* (1975) proposed that it is better to use the magnitude of the vorticity $|\tilde{\omega}|$, rather than $|\tilde{S}|$, in equation (2.29). However, there is no evidence to show that these modifications significantly improve the original Smagorinsky SGS model.

2.4.1.2 Schumann's SGS Models

As an alternative to Smagorinsky's SGS model, Schumann (1975) proposed a SGS model with two eddy viscosities. The idea behind Schumann's SGS Model is as follows. Firstly, the resolvable scale component $\tilde{\Phi}$ based on filtering or volume averaging consists of the mean component $\overline{\tilde{\Phi}}$ and a fluctuating part around it. The characteristic length scale of the former is much larger than that of the latter. With this in mind, Schumann inferred that it is not appropriate to model τ_{ij} using a single SGS eddy viscosity. So, he divided the strain rate tensor of the resolved velocity $\tilde{S}_{ij}$ into

mean and fluctuating parts, and wrote the model expression as

$$\tau_{ij} = -\widetilde{u_i' u_j'} = 2\nu_t^*(\tilde{S}_{ij} - \overline{\tilde{S}_{ij}}) + 2\nu_t \overline{\tilde{S}_{ij}} - \frac{1}{3}\delta_{ij}\widetilde{u_k' u_k'} \tag{2.34}$$

where ν_t^* and ν_t are the SGS eddy viscosities associated with, respectively, the fluctuating and mean parts of $\tilde{S}_{ij}$.

Schumann assumed that ν_t^* is more isotropic than ν_t in his LES of a channel flow using the volume averaging approach. Therefore, the following model was applied:

$$\nu_t^* = C_\nu^*(FK)^{1/2}C' \tag{2.35}$$

where F is the characteristic size of the surface used in finding τ_{ij}; K is the SGS kinetic energy contained within the area F; C_ν^* is an adjustable factor corresponding to C_ν in Smagorinsky's model; and C' is an additional coefficient introduced to account for anisotropic effects. Since the SGS eddy viscosity ν_t is closely associated with the mean flow, which in the channel flow is in the x_1 direction only, it was therefore modelled by

$$\nu_t = l^2|\delta_2 \overline{\tilde{U}_1}| \tag{2.36}$$

where l is the so-called mixing length; δ_2 represents the finite difference operator in the x_2 direction. Schumann defined the mixing length as:

$$l = \min[C_l F^{1/2}, \kappa x_2']$$

where C_l is a numerical coefficient; x_2' is the distance to the nearest wall; κ (≈ 0.4) is the Von Karman constant.

In Schumann's model, K was solved from a transport equation. Thus, the model is also referred to as one-equation SGS model. The SGS modelling approach of using one additional transport equation was also adopted by Grotzbach (1979, 1986) and

Horiuti & Yoshizawa (1985).

Moin and Kim (1982) applied and modified Schumann's model in their LES of plane channel flow. In the modelling of ν_t^*, they suggested the following expression:

$$\nu_t^* = C_\nu^* \Delta^2 |\tilde{S}_{ij} - \overline{\tilde{S}_{ij}}|$$

where Δ is defined as $(\Delta_1 \Delta_2 \Delta_3)^{1/3}$. The second eddy viscosity was modelled as

$$\nu_t = C_\nu [\Delta_3 f(x_2)]^2 |\overline{\tilde{S}_{ij}}|$$

where $f(x_2)$ is a wall damping function. In this version of the model, no SGS kinetic energy was applied. The idea of choosing the span-wise grid length scale Δ_3 as the characteristic length scale was suggested by the streak structure of turbulent boundary layers observed by Kline *et al.* (1967).

2.4.2 Scale Similarity and Mixed SGS Models

Bardina *et al.* introduced the scale similarity SGS model in 1980. The model is based on the assumption that the interaction between the SGS and resolved eddies is similar in form to that between the filtered and twice filtered fields. By representing the SGS velocity by the difference between the filtered and twice filtered fields, they suggested a SGS model for the Reynolds stress tensor as shown in equation (1.1). The analysis of both the DNS data (Bardina *et al.*, 1980) and the experimental data (Lui *et al.*, 1994) have shown that the model exhibits a good correlation with the real SGS Reynolds stress.

However, when implemented in LES calculations, a Smagorinsky-like term should be added to the model shown in equation (1.1), because the pure scale similarity model

dissipates no energy, which causes numerical instability in the simulation procedure. Therefore, the so-called mixed SGS model was proposed, which takes the following form

$$\tau_{ij} = C[(\tilde{U}_i\tilde{U}_j - \widetilde{\tilde{U}_i}\widetilde{\tilde{U}_j}) - \delta_{ij}(\tilde{U}_k\tilde{U}_k - \widetilde{\tilde{U}_k}\widetilde{\tilde{U}_k})] - 2\nu_t\tilde{S}_{ij}. \tag{2.37}$$

It is the mixed SGS model that was really employed by Bardina *et al.* (1980). Later, the mixed SGS model was applied to the simulation of homogeneous turbulence in rotating coordinates with sheared turbulence (Bardina *et al.*, 1983).

Since Bardina. several new formulations have been proposed to correct for the lack of dissipation of the pure scale similarity SGS model. Goutorbe *et al.* (1994) and Lui *et al.* (1994) have proposed using a second filter or spatial average different from the first one. The idea is somehow related to the concept of the dynamic SGS models which will be reviewed in the next subsection.

The scale similarity SGS model breaks through the shackles of the eddy diffusivity modelling approach. It is plausible and represents a promising direction for accurate SGS modelling. The mixed SGS model can be deemed as a compromise between new and old in order to avoid the difficulty associated with the new. This difficulty is surmountable. as will be shown below.

2.4.3 Dynamic SGS Models

The adjective "dynamic" means that the coefficients appearing in the SGS models are determined "dynamically" in accordance with the local instantaneous flow fields under consideration. In other words, the dynamic SGS models have no coefficient to be determined empirically before simulation. This feature is very attractive to making LES a real predictive rather than a postdictive numerical method. Based on the Smagorinsky SGS model, Germano *et al.* (1991) proposed that the model coefficient, *i.e.* the Smagorinsky coefficient, be calculated by applying another so-

called test-grid filtering to the flow fields. The characteristic width of the test-grid filtering (Δ') is larger than that of the sub-grid filtering (Δ).

A key assumption on which Germano dynamic SGS model is based is that the Smagorinsky coefficient is independent of the characteristic width of the filtering. It is also assumed that the Leonard and cross-correlation terms can be lumped together with the SGS Reynolds stress, and modelled by the same relation. Thus, following equation (2.28), we can write the eddy viscosity model expressions at both sub-grid and test-grid levels as

$$\tau_{ij} = -(\widetilde{\tilde{U}_i\tilde{U}_j} - \tilde{U}_i\tilde{U}_j) = 2\nu_t\tilde{S}_{ij} - \frac{1}{3}\delta_{ij}(\widetilde{\tilde{U}_k\tilde{U}_k} - \tilde{U}_k\tilde{U}_k) \tag{2.38}$$

and

$$\tau'_{ij} = -(\widehat{\tilde{U}_i\tilde{U}_j} - \hat{\tilde{U}}_i\hat{\tilde{U}}_j) = 2\nu'_t\hat{\tilde{S}}_{ij} - \frac{1}{3}\delta_{ij}(\widehat{\tilde{U}_k\tilde{U}_k} - \hat{\tilde{U}}_k\hat{\tilde{U}}_k). \tag{2.39}$$

Now, using Smagorinsky's model to express ν_t and ν'_t, respectively, in equations (2.38) and (2.39) with the same coefficient C_ν, then test-grid averaging equation (2.38), and subtracting the resultant equation from equation (2.39), we can obtain the following tensor identity:

$$L_{ij} - \frac{1}{3}\delta_{ij}L_{kk} = 2C_\nu M_{ij} \tag{2.40}$$

where

$$L_{ij} = \hat{\tilde{U}}_i\hat{\tilde{U}}_j - \widehat{\tilde{U}_i\tilde{U}_i}, \tag{2.41}$$

$$M_{ij} = \Delta'^2|\hat{\tilde{S}}|\hat{\tilde{S}}_{ij} - \Delta^2\widehat{|\tilde{S}|\tilde{S}_{ij}}. \tag{2.42}$$

We will show here that some specific conditions should be satisfied to validate the derivation by Germano *et al.* (1991). First of all, one should assume that

$$\hat{\tilde{\Phi}} = \hat{\Phi} \tag{2.43}$$

for any field Φ. Apparently, equation (2.43) is valid only in the case of using the ideal

filter. Furthermore, in order to calculate L_{ij} and M_{ij} from the resolvable or sub-grid filtered fields, it must be possible to write equations (2.41) and (2.42) as

$$L_{ij} = \hat{\tilde{U}}_i\hat{\tilde{U}}_j - \widehat{\tilde{U}_i\tilde{U}_i} \tag{2.44}$$

and

$$M_{ij} = \Delta'^2|\hat{\tilde{S}}|\hat{\tilde{S}}_{ij} - \Delta^2\widehat{|\tilde{S}|\tilde{S}_{ij}} \tag{2.45}$$

where $\hat{\tilde{S}}$ represents the strain rate of velocity based on $\hat{\tilde{U}}_i$. The above formulation is only possible in the case when equation (2.43) is valid. Therefore, Germano's dynamic SGS model is only applicable with the ideal filter.

We refer to the feature (of a coarse-graining approach in LES) expressed by equation (2.43) as "supercedity", and will show in Chapter 3 that the volume averaging approach retains this feature.

Let's return to equation (2.40) where every term can be determined explicitly from the large scale fields in LES. However, equation (2.40) represents five independent equations for one unknown variable, C_ν. Germano *et al.* (1991) contracted it with $\tilde{S}_{ij}$ to obtain,

$$C_\nu = \frac{L_{ij}\tilde{S}_{ij}}{2M_{ij}\tilde{S}_{ij}}. \tag{2.46}$$

In tests using channel flow data from DNS, Germano *et al.* (1991) have shown that expression (2.46) may lead to numerical instability because its denominator could locally vanish or become extremely small. A remedy to this problem is to take an appropriate average along a homogeneous direction. Lilly (1992) suggested an alternative contraction that minimises the total error of the equations in the least-squares sense, *i.e.*

$$C_\nu = \frac{L_{ij}M_{ij}}{2M_{ij}M_{ij}} \tag{2.47}$$

The advantage of expression (2.47) is that its denominator is positive definite and vanishes only when the numerator also vanishes. Thus, it is more popular than

Germano's original expression, and was employed by, for example, Piomelli (1993b) and Sreedhar & Ragab (1994).

Germano's dynamic SGS model is an eddy diffusivity SGS model in nature, so that it can be used only if both Δ and Δ' are in the inertial subrange of scales. Germano *et al.* (1991) extrapolated it into the wall regions of turbulent flow. However, the dynamic meaning of this model in the wall regions is rather unclear. The problem associated with this extrapolation is that the C_ν calculated can be of either sign or even zero, and fluctuates considerably in both time and space. Analysis of DNS data (Lund *et al.*, 1993) and of experimental data (Liu *et al.*, 1994) shows that the variance of C_ν may reach values more than 10 times its mean value! Although allowing a negative value of C_ν is a positive feature of the model which represents a sort of backscatter of the turbulent kinetic energy, too large of negative values are unphysical and will destabilize the numerical solution procedure. In order to avoid this problem, Germano *et al.* (1991) suggested that equation (2.40) be averaged over space and/or time. Averaging over the direction of flow homogeneity has been a popular choice and has produced good results. The trade-off of this additional averaging procedure is the loss of some "dynamic" features of the model. Zhao & Voke (1996) suggested that not equation (2.40) but the value of C_ν be averaged over the homogeneous direction. The performance of the dynamic SGS model was shown to be improved with this modification.

Germano's idea of dynamic SGS modelling was successfully extended in the form of a mixed SGS model by Zang *et al.* (1992), who showed some advantages of this so called "dynamic mixed SGS model" over Germano's dynamic SGS model. In Zang's dynamic mixed SGS model, spatial averaging and "cut-off" are applied to avoid over-backscatter of the energy. An alternative approach to the additional averaging has been suggested by Meneveau *et al.* (1994). Instead of averaging over directions of homogeneity, the error associated with Germano's identity is minimised along particle trajectories. The approach has been shown to be as effective as spatially averaging. However, two additional transport equations need to be solved, which

then increases the computational effort. Wu & Squires (1997) combined Meneveau's particle trajectory approach with Zang's dynamic mixed SGS models. With this so-called Lagrangian mixed dynamic model, they simulated an equilibrium 3-D turbulent boundary layer. The results obtained match well with the DNS data.

2.4.4 Other SGS Modelling Methods

Three SGS modelling methods, *i.e.* the SGS modelling method with transport equations, the "built-in" SGS models, and the spectral SGS models, which are not representable of the main stream of the LES research are reviewed briefly in this subsection.

2.4.4.1 SGS Modelling with Transport Equations

The idea of calculating all components of the SGS Reynolds stress tensor using transport equations derived for them comes from an analogy to the second moment closure model for the RAM methods of turbulence. Theoretically, there is no difficulty in deriving a set of transport equations for τ_{ij} as shown in equation (2.27). However, there are at least two major problems associated with the solution of the equations. Firstly, the equations contain many SGS scale related terms which should be modelled. The modelling for these SGS scale related terms is actually not easier than that for the SGS Reynolds stress itself. Secondly, the solution of six additional partial differential equations will more than double the computing cost.

The only use of this modelling method to date was by Deardorff (1973) in his LES of meteorological flows. Since, in his simulation, a scalar quantity (*i.e.*, the temperature) is also involved, the solution system of the simulation is closed by 10 additional partial differential equations. Deardorff reported a computer time increase on the order of 2.5 compared with the case of using Smagorinsky's model. Although using the transport equation SGS model does lead to improved results, such a complex

modelling method is less attractive than the previously reviewed scale similarity SGS model or dynamic SGS model combined with the possibility of using a judiciously distributed set of mesh points over solution domains.

2.4.2.2 Built-in SGS models

The essence of built-in or intrinsic SGS models is actually "no SGS model at all". The idea is based on the fact that numerical schemes always involve truncation errors as well as numerical diffusion or damping. Under specific conditions, the effect of these truncation errors is to mimic that of the SGS fluctuations, so that no SGS model is necessary. We can call this LES without any SGS model as coarse-grid or pseudo DNS. Some of the results obtained with this approach appear reasonable, *e.g.* Kawamura & Kuwahara (1984), while others have displayed very poor agreement with experiments (Silveira-Neto *et al.*,1993). Boris *et al.* (1992) showed that the monotone algorithms such as the piecewise parabolic method or flux-corrected transport method have intrinsically the features of a SGS model coupled naturally to the resolved scales in the computed flow. Nevertheless, it is still open to question how to ensure that a numerical scheme exactly meets the requirements of SGS modelling.

More recently, Denaro (1996) suggested that the SGS effect be recovered by using higher order approximation for the advective terms. In Denaro's so called model-free simulation, a numerical flux is defined from a weak integration formulation derived from the Taylor expansion. However, it is still doubtful that the SGS effect on the inter-control-volume transport can be retrieved from a filtered field through a purely mathematical handling.

It is worthwhile to note that the intrinsic SGS models at least remind us that numerical schemes have an effect on the SGS models, and we should consider both the numerical scheme and the SGS modelling procedure together in LES.

2.4.2.3 Spectral SGS Models

Both Smagorinsky's and Schumann's SGS models have been constructed from dimensional analysis incorporated with physical considerations based on the inertial-subrange concept for homogeneous turbulence. On the other hand, statistical theories of homogeneous turbulence based on the two-point correlations have been elaborated. Therefore, it is natural that efforts have been made to develop the SGS models or to estimate numerical parameters appearing in the developed SGS models using these elegant theories. Using statistical theories, the SGS models are studied in wave number space. Thus, these SGS models are referred to as spectral SGS models or two-point closure SGS models. For detailed review of these models, see Lesieur *et al.* (1993), Herring & Kerr (1993), and Lesieur & Metais (1996).

The two-point closure theory on which the spectral SGS models are based is only valid for isotropic and/or homogeneous turbulence. To the author's knowledge, all spectral SGS models are of the eddy diffusivity type, and the theories are only used to obtain expressions for the SGS eddy diffusivity. Additionally, the spectral SGS models are too complicated to be handled numerically in physical space, especially when the geometry of the solution domain is complex. All of the above facts hinder the application of these models to the turbulent flows encountered in engineering practice.

2.5 Application of LES

In this section, previous LES applications will be reviewed based on the types of turbulent flows considered. The scope of discussion here is limited to flows of engineering interest. For a review of the LES applications in the area of geophysics, see Wyngaard & Moeng (1993).

The emphasis of previous LES work can be classified as: 1) development of the LES technique; 2) exploring physics of turbulence and constructing RAM's; and 3) application to real problems. Only rarely has the LES method been applied to explore the physics of turbulence or to develop RAM's; people have preferred to do that using the DNS method on low Reynolds number turbulent flows, so that the uncertainty brought in by the SGS modelling procedures can be avoided. Thus, in this section, we focus our attention only on the LES work in categories 1) and 3).

The objectives of most LES work carried out to date pertain to category 1), *i.e.* to test or verify the SGS models or other LES techniques. The vast majority of problems tackled so far with the LES technique are so called "building-block" flows, problems that isolate one or two physical phenomena of engineering interest and are handled in a simplified geometry. The reason is that, to date, the LES method is still too expensive to handle an engineering flow of moderate complexity. We begin our discussion with LES work on these building-block flows, and then switch to those on real flows in engineering practice. Meanwhile, challenges associated with the LES of some of the flows will be discussed as well.

2.5.1 Burgers' Flow

The simplest flow to be considered for testing the SGS models is the 1-D flow governed by the periodic Burgers' equation, a 1-D analogy to the Navier-Stokes equation. Advantages of using Burgers' equation to test SGS models is apparent. It retains some important features of the Navier-Stokes equation, such as nonlinearity, advection and diffusion processes, and it is relatively easy to solve analytically or numerically at high Reynolds number. The approach has been adopted by Love & Leslie (1977), Love (1980), Dakhoul & Bedford (1986), and Aldama (1990). Nevertheless, the feasibility of the approach is open to question. Firstly, turbulence is actually a 3-D phenomenon; it is not justified to represent a 3-D dynamical procedure with 1-D equation. Sec-

ondly, the absence of the pressure term and the continuity constraint in the Burgers' equation imply that the 1-D flow governed by the periodic Burgers' equation may be significantly different from real turbulence.

2.5.2 Homogeneous Flows

Homogeneous flows play an important role in the development of turbulence theory, and so do they in the development of the SGS modelling for the LES. A homogeneous flow is one in which the statistics of turbulence are the same at every point in space. Therefore, a homogeneous flow exhibits no convection and diffusion transport, and only the production, dissipation and redistribution need to be dealt with.

Homogeneous flows can be classified as: 1) isotropic homogeneous flows; 2) strained homogeneous flows; and 3) sheared homogeneous flows. An isotropic homogeneous flow is initiated by a divergence-free random perturbation with the desired energy spectrum. Since the only turbulent effect in isotropic homogeneous flows is dissipation, the turbulence is decaying with time. Experimentally, isotropic homogeneous flows can be approximated in a wind tunnel by using grids or a set of jets. A strained homogeneous flow is produced by putting an initially isotropic flow through a wind tunnel section in which fluid elements are stretched in one direction and compressed in another direction. In strained homogeneous flow, the turbulence decays for a short time and then increases with time due to the production caused by by irrotational strain. Sheared homogeneous turbulence is produced in a flow which has uniform shear. Sheared homogeneous turbulence behaves in a manner similar to strained homogeneous turbulence, *i.e.* after a period of decay, the turbulent energy begins to increase.

Application of the LES to homogeneous flows has been broadly performed by several LES researchers, including Shaanan *et al.* (1975), McMillan & Ferziger (1980), Kaltenbach *et al.* (1994), Sukoriansky (1996), and Menon *et al.* (1996). There

are several advantages to using homogeneous flows for developing the SGS models. Firstly, the flows have been investigated in depth experimentally and numerically; see Ferziger (1980) for a review. Secondly, the governing equations for LES can be significantly simplified in a case when the flow considered has homogeneous directions, and less computer resources are required. Third, the statistical theory of turbulence has been elaborated for homogeneous flows, which can serve to guide the SGS modelling development. However, no homogeneous flow really occurs in scientific and technological applications. Thus, a SGS model developed in a homogeneous flow may not be appropriate for flows which occur in engineering practice.

2.5.3 Free Shear Flows

Free shear flows are one of the types of flow of major engineering interest. They can be grouped into three categories: 1) a mixing layer — which occurs when two parallel flows of different speed are brought together; 2) a jet — a stream of fluid issuing from an opening; and 3) a wake — the velocity defect behind an impenetrable body. The "free" here is equivalent to "no bounding walls". It has been broadly accepted that free shear flows are easier to simulate than wall-bounded flows, because free boundary conditions are easier to handle numerically than solid ones.

The early LES work on free shear flows was limited to the mixing layer which has been studied analytically, experimentally, and numerically for a long time. Much of the recent work is concerned with the coherent vortex structures observed in a mixing layer. LES of the mixing layer was first made at low resolution by Mansour *et al.* (1978). Cain *et al.* (1981) obtained better results by scaling the grid to include the fundamental instability wave and its sub-harmonic. The mixing layer is of continuing interest to researchers in LES. Some recent LES of the mixing layer are those by Milane & Nourazar (1995) and Lesieur (1996).

Systematic study of wakes and jets with the LES method began in the 1990's.

Wakes and jets are generally classified as 2-D and 3-D according to the configuration of the obstructions or discharge outlets. Solution domains of wakes may cover regions upstream of the obstacle body. Some recently reported LES work on wakes are as follows: Sakamoto *et al.* (1993), Joshi *et al.* (1994), Jordan (1994), Sun & Dalton (1994,1995), Murakami & Mochida (1995). Those on jets are: Dai *et al.* (1994), Voke *et al.* (1995), and Akselvoll & Moin (1996).

2.5.4 Wall-Bounded Flows

The significance of wall-bounded flows in technological application and the difficulties associate with simulating them have been described in Chapter 1, where we distinguished between near-wall flows with and without turbulent production caused by the "streaks". It is believed that the most expensive application of LES to date has been the calculation of near-wall flow with streaks, because extremely high resolution is necessary to capture the turbulent production mechanism of the streaks. According to Kline *et al.*'s experimental investigation (1967), at least five wall units span-wise and 20 wall units stream-wise resolution are required. However, if high resolution meshes should be employed near walls for a fully developed channel or duct flow, the advantage of the LES method over the DNS method will be diminished.

The LES of fully-developed plane channel flow was first performed by Schumann (1975). Kim & Moin (1979) reported the results of LES for a fully developed channel flow using a higher resolution grid ($64 \times 64 \times 64$) and a near wall damped SGS eddy viscosity model. This work was later repeated (Moin & Kim, 1982) using still greater resolution ($64 \times 128 \times 63$), a modified SGS model, and improved numerical schemes. The computed velocity and pressure fields were used to show the coherent structures of near-wall turbulence, and the result was in good agreement with laboratory observations (see Kline *et al.*, 1967). This is probably one of the most remarkable achievements in CFD of turbulence in this century.

LES of wall-bounded flows in the 1990's was not limited to fully developed plane channel flows. The degree of complexity of the problems considerably increased to become closer to real problems in engineering application. The main objective of the LES of these flows was still to test the LES technique developed, but they also provide experience for finally applying the LES method to flows of technological interest. We will briefly review some of this work.

Kajishima & Miyake (1992a) performed LES of channel flow at $Re = 4900$ with fluid injection from one wall using a grid of 1.23×10^6 control volumes. Ciofalo & Collins (1992) considered heat transfer in their LES of plane and rib-roughened channels at Reynolds numbers from 10000 to 40000. Zhou *et al.* (1996) and Thomas & Williams (1994) performed LES of open channels, with and without curvature, which have significance in hydraulic engineering.

Duct flows are similar to plane channels in many aspects. The LES of flow in a square duct was made by Kajishima *et al.* (1992b) at Reynolds numbers of 6200 and 67400 with a grid of 1.6×10^5 control volumes. Similar work was conducted by Su & Friedrich (1994a) in Tsinghua University of China, and by Breuer & Rodi (1994). The LES of duct flows with curvature was made by Su & Friedrich (1994b), Breuer & Rodi(1994), and Boersma & Nieuwstadt (1996).

Unlike fully developed channel flows, Flows in boundary layers are of developing in the stream-wise direction, which makes LES of free boundary layers a bit more difficult. LES of both thermal and momentum boundary layers at Re_θ between 353 to 576 were made by Tsai & Leslie (1990). Recently, LES of a developing boundary layer at Re_θ between 1470 to 1700 using the dynamic SGS model was reported by Wu *et al.* (1997). The LES of a spatially developing boundary layer on a concave surface was also carried out by Lund & Moin (1997) in Stanford University.

The LES has also been applied to cavity and back-facing-step flows. Strictly speaking, these are not pure wall-bounded flows, *e.g.* a back-facing-step flow can be viewed as a wall-bounded wake, while a shear-driven cavity flow is, in nature, a wall-bounded

shear layer. Jordan & Ragab (1994) published their LES of 3-D shear-driven cavity flow at Reynolds numbers of 5000 and 10000. The same simulation was performed by Zang *et al.* (1992,1993) using the dynamic and dynamic mixed SGS models. A LES of a back-facing step flow was made by Ortega *et al.* (1996).

2.5.5 Real Flows of Engineering Interest

Strictly speaking, only the LES work in category 3) can be viewed as genuine applications. Rarely have such applications been reported prior to 1990. To the author's knowledge, the earliest successful application of LES is that by Grotzbach (1979) who used a very coarse grid ($16 \times 16 \times 8$) LES to investigate the effect of buoyancy on flow mixing in the downcommer of a nuclear reactor — a problem related to nuclear reactor safety. His LES results and conclusion were later confirmed by experiments. The LES of wind tunnel airflow around a model of building was first performed by Murakami *et al.* (1986) and Murakami *et al.* (1987). In their simulation, the Reynolds number based on the size of the model and approaching wind speed was 10^5, and a grid of $44 \times 33 \times 21$ cells was employed. The correspondence between the simulation and wind tunnel experiment results was found to be good. However, this work can only be viewed as an indirect application of the LES method to real engineering flows.

The features of low Reynolds number ($\simeq 10^5$) and simple geometrical configuration make the airflow around a model building an ideal target for LES application. In the 1990's, a few such applications were performed. Among them are those by Baetke *et al.* (1990), Yang *et al.* (1993), Mochida *et al.* (1993), Frank & Mauch (1993), Murakami *et al.* (1995), Yu and Kareem (1996a, 1996b), and Murakami *et al.* (1996). All of these showed good agreement between the LES and the corresponding experimental results, and some of them, *e.g.*, Murakami *et al.* (1996) also showed the superiority of the LES method over the RAM methods. LES of the flow fields around full size building were also reported by Mochida *et al.* (1993) and He & Song (1995).

The results obtained corresponded well with the field measurements.

Application of the LES method to simulate flows in tube bundles has been active since 1990 at Texas A & M University. Flows of this type are always encountered in the designs of heat exchangers, so that the LES of them has engineering significance. The main objective of LES work at Texas A & M University on tube bundles is to investigate instantaneous flow patterns in tube bundles and/or to calculate turbulent buffeting forces on them. For reference, see Pruitt *et al.* (1991), Hassan *et al.* (1991), Hassan *et al.* (1993), Pruitt *et al.* (1993), Hassan *et al.* (1994), Barsamian *et al.* (1994).

Another type of real flow for which simulations are being performed using the LES method is channel flows in hydraulic engineering. These applications can be viewed as a direct high Reynolds number extension of Shumman's (1975) pioneering work on a 2-D channel flow. Thomas & Williams (1995) performed a LES of flow in a compound open channel with one flood plain at Reynolds number 42000. If this simulation is still not a typical engineering application due to its low Reynolds number, another LES of a symmetric trapezoidal channel at Reynolds number 430,000 performed later (Thomas & Williams 1996) definitely is.

In addition, the application of the LES method to air pollution problems was tried by Meszaros *et al.* (1987) and McGrattan *et al.* (1996) to a flow in a baffled stirred tank reactor by Eggels (1996).

Although a significant advance has been made in the 1990's, the LES method is still far from being a routine tool in engineering practice. The published applications of a limited number of engineering applications appear to be successful, however the unsuccessful examples are generally not published. Currently, the LES techniques, especially the SGS modelling technique, are still deficient and need to be improved to handle the wide range of real flows which occur in engineering applications. The LES is still considerably more expensive than the RAM method. Due to the limited computer resources available, one has to apply a very coarse grid, for which the LES

method almost degenerates to the RAM method. As will be shown later, the development of the VAT not only improves the LES techniques, but also partly alleviates the problem of inadequate computer resources by allowing the use of coarser grids.

2.6 Summary

In this chapter, the current state of the art in the area of LES for turbulent flows has been reviewed. Specifically, the main characteristics of the coarse-graining approaches and the developed SGS modelling techniques have been described. It is concluded that although notable achievements have been made since the 1970's, the LES today has limited use in the engineering research community. The main problem is still inappropriate SGS modelling approaches, *e.g.* the eddy diffusivity SGS models have faced some of the same problems as the Reynolds average models. The scale similarity SGS model is superior in principle to the eddy diffusivity SGS models, but some modifications and improvements are required. In the next chapter, we will present such modifications and improvements in the formulation of the VAT for turbulent flow simulation.

Chapter 3

Mathematical Formulation

3.1 Introduction

In this chapter, the mathematical formulas on which the volume average technique of the LES method is based are derived systematically in the same frame as the control volume discretization. The derivation starts from the conservation laws of mass, momentum, and energy for incompressible flows. Since the technique will finally be applied to room airflow prediction, assumptions corresponding to a typical room airflow are made. However, the method can easily be extended to any other incompressible or slightly compressible flow.

3.2 Basic Equations

Governing equations of a flow are mathematical representations of the physical laws the flow obeys. Let's consider a typical room airflow. Firstly, thermal comfort of human beings requires that both temperature variation and air motion speed in a room be relatively small compared to, respectively, the bulk temperature in Kelvin and the speed of sound. Typically, the temperature variation in an air-conditioned room is less than 10 K, and the speed of air motion is less than 5 m/s. Therefore, it is reasonable to assume that all physical properties of air are constant except for the density difference in the body force term in the momentum equation. Using the Boussinesq approximation and without considering kinetic energy dissipation in the energy equation, the basic equations governing the airflow in a room are:

$$U_{i,i} = 0 \tag{3.1}$$

$$\dot{U}_i + (U_i U_j)_{,j} = -\frac{1}{\rho_0} P_{,i} - \beta g_i \Theta + \nu U_{i,jj} \tag{3.2}$$

$$\dot{\Theta} + (\Theta U_j)_{,j} = \alpha \Theta_{,jj} \tag{3.3}$$

where U_i represents the instantaneous velocity component in the ith direction; P, the instantaneous pressure; ρ_0, a constant reference density; g_i, the component of the gravity vector; Θ, the temperature deviation from a fixed reference value; ν, the fluid kinematic viscosity; α, the fluid thermal diffusivity; β, the fluid volumatric expansion rate; x_i, the ith component of a Cartesian position vector; t, the time. In our notation, $(\cdot)_{,i}$ and $\dot{(\cdot)}$ denote, respectively, space and time derivatives, *e.g.*

$$(\cdot)_{,i} \equiv \frac{\partial(\cdot)}{\partial x_i}; \quad (\cdot)_{,ij} \equiv \frac{\partial^2(\cdot)}{\partial x_i \partial x_j}; \quad \dot{(\cdot)} \equiv \frac{\partial(\cdot)}{\partial t}.$$

The summation convention is employed for repeated indices in each term.

Equation (3.1) through (3.3) are a set of time-dependent, three-dimensional, non-

linear, partial differential equations which mathematically represent velocity and temperature fields in a room. They are the starting point of all numerical simulation approaches for room air flow.

3.3 Volume Average Approach

As in any other LES technique, the first step of the volume average technique of turbulence is to define the large-scale fields the method can solve explicitly. For that purpose, we divide the flow domain into control volumes in the same way as we do in finite volume space discretization. The length scales of a control volume in each direction are denoted as Δx_i. Then, the node value of a field in each control volume is defined as a volume average of the field in the control volume which can be expressed as

$$\tilde{\Phi} = \frac{1}{\Delta V}\iiint \Phi dV \tag{3.4}$$

where ΔV represents the volume of the control volume under consideration,

$$\Delta V = \Delta x_1 \Delta x_2 \Delta x_3$$

and Φ is a field to be averaged. By applying the volume average (3.4) to equation (3.1) through (3.3), the following finite difference form equations can be obtained:

$$\delta_i \overbrace{U_i}^{i} = 0 \tag{3.5}$$

$$\dot{\tilde{U}}_i + \delta_j \overbrace{U_i U_j}^{j} = -\frac{1}{\rho_0}\delta_i \overbrace{P}^{i} - \beta g_i \tilde{\Theta} + \nu \delta_j \overbrace{U_{i,j}}^{j} \tag{3.6}$$

$$\dot{\tilde{\Theta}} + \delta_j \overbrace{\Theta U_j}^{j} = \alpha \delta_j \overbrace{\Theta_{,j}}^{j} \tag{3.7}$$

where $\overbrace{\Phi}^{i}$ denotes an average of field Φ over a control volume surface normal to x_i-direction,

$$\overbrace{\Phi}^{i} = \frac{1}{\Delta S_i}\iint \Phi dS \tag{3.8}$$

where ΔS_i represents the area of control volume surface perpendicular to the x_i direction, *e.g.*

$$\Delta S_1 = \Delta x_2 \Delta x_3$$

and $\delta_i \overbrace{\Phi}^{i}$ is the centre difference of the surface average,

$$\delta_i \overbrace{\Phi}^{i} = \frac{1}{\Delta x_i}(\overbrace{\Phi}^{i+\frac{1}{2}} - \overbrace{\Phi}^{i-\frac{1}{2}}).$$

It should be pointed out here that two kinds of averages appear in the above formulation, *i.e.* the volume averages defined in equation (3.4) and surface averages defined in equation (3.8). Since the surface averages are not calculable in the simulation, following the same approach as in the conventional finite volume method, the surface averages of quantities will all be expressed in terms of the node values of the corresponding quantities, which themselves are volume averages, through homogeneous interpolation.

Then, the following decompositions are introduced,

$$U_i = \widetilde{U_i} + u_i$$

$$\Theta = \tilde{\Theta} + \theta$$

$$P = \tilde{P} + p$$

where u_i, θ, and p are, respectively, the SGS portions of the velocity, temperature, and pressure fields. When substituting the above decompositions into equations (3.5)

through (3.7), we face the task of dealing with both linear and nonlinear terms involving surface averages. The SGS portions of fields vanish in the linear terms, since surface averages in these terms can be expressed in terms of homogeneous interpolations of the volume averages, and volume averages of SGS portions are zero in control volumes. On the other hand, the SGS portions of fields will play important roles in the nonlinear terms of the equations, from which the SGS turbulent transport comes.

Let's expand the nonlinear terms on the LHS of equations (3.6) and (3.7) as follows:

$$\delta_j \overbrace{\widetilde{U}_i\widetilde{U}_j}^{j} = \delta_j \overbrace{(\widetilde{U}_i + u_i)(\widetilde{U}_j + u_j)}^{j} = \delta_j(\overbrace{\widetilde{U}_i\widetilde{U}_j}^{j} + \overbrace{u_i u_j}^{j} + \overbrace{\widetilde{U}_i u_j}^{j} + \overbrace{u_i\widetilde{U}_j}^{j}) \tag{3.9}$$

$$\delta_j \overbrace{\widetilde{\Theta}\widetilde{U}_j}^{j} = \delta_j \overbrace{(\widetilde{\Theta} + \theta)(\widetilde{U}_j + u_j)}^{j} = \delta_j(\overbrace{\widetilde{\Theta}\widetilde{U}_j}^{j} + \overbrace{\theta u_j}^{j} + \overbrace{\widetilde{\Theta}u_j}^{j} + \overbrace{\theta\widetilde{U}_j}^{j}). \tag{3.10}$$

The first terms in the parentheses on the RHS's of equations (3.9) and (3.10) have nothing to do with the SGS portions of fields. These terms actually represent, respectively, the momentum and heat energy fluxes caused by convection of large scale motions through control volume surfaces, and can be handled in the same way as in the conventional finite volume method. In both terms, the surface averages do not make any sense for the same reason pointed out in subsection 2.3.1, *i.e.* the finite volume scheme can not sense any fluctuations of $\tilde{U}_i\tilde{U}_j$ or $\tilde{\Theta}\tilde{U}_j$ on a control volume surface with length scales larger than the surface size. Thus, numerically, these surface averages can be ignored.

The second terms in the parentheses on the RHS' of equations (3.9) and (3.10) represent, respectively, momentum and heat energy fluxes through control volume surfaces due to correlation among components of SGS velocity and temperature fluctuations. These terms are referred to as the SGS Reynolds stress and the SGS turbulent heat flux respectively, and should be modelled in the technique. It is convenient

to adopt a formulation with minus signs, so that they are denoted as

$$\tau_{ij} = -\overbrace{u_i u_j}^{j} \tag{3.11}$$

and

$$\sigma_j = -\overbrace{\theta u_j}^{j}. \tag{3.12}$$

The last two terms in the parentheses of the RHS' of equation (3.9) and (3.10) are the so called cross-correlation terms which represent, respectively, momentum and heat energy fluxes caused by correlation between SGS velocity fluctuations and large scale motions. As was mentioned in chapter 1, the cross-correlation terms vanish in the context of the volume average approach, because in that case we assume a uniform distribution of averaged fields on surfaces of each control volume, which have no correlation with the SGS fluctuations. However, these are the so-called SGS turbulent diffusion terms representing a transport enhancement mechanism analogous to molecular diffusion, which should be modelled. We denote them in the momentum and energy equations as, respectively, ξ_{ij} and ψ_j.

Using the above notations and noting that although volume averages of quantities are not defined at control volume surfaces, we still can use them instead of the surface averages of quantities at control volume surfaces appearing in equation (3.5) through (3.7) by implicitly acknowledging that the volume averages of quantities at control volume surfaces are obtained through homogeneous interpolations, then the final form of the governing equations are as follows:

$$\delta_i(\widetilde{U}_i) = 0 \tag{3.13}$$

$$\dot{\widetilde{U}}_i + \delta_j(\widetilde{U}_i\widetilde{U}_j) = -\frac{1}{\rho_0}\delta_i(\tilde{P}) - \beta g_i\tilde{\Theta} + \nu\delta_j(\widetilde{U}_{i,j}) + \delta_j(\tau_{ij} + \xi_{ij}) \tag{3.14}$$

$$\dot{\tilde{\Theta}} + \delta_j(\tilde{\Theta}\widetilde{U}_j) = \alpha\delta_j(\tilde{\Theta}_{,j}) + \delta_j(\sigma_j + \psi_j). \tag{3.15}$$

3.4 Models for SGS Reynolds Stress and SGS Turbulent Heat Flux

The purpose of the SGS modelling is to express the SGS Reynolds stress τ_{ij}, SGS turbulent heat flux σ_j, and SGS turbulent diffusion terms ξ_{ij} and ψ_j in terms of only the solvable large scale fields, *i.e.* the volume averaged field quantities defined at the node of each control volume, in a physically consistent manner, so that the equation system can be closed. The SGS modelling is the most challenging task in, and the key to the success of, the VAT of turbulent flow simulation. In this section, the functional dynamic scale similarity models for the SGS Reynolds stress and SGS turbulent heat flux are discussed in detail. Models for the SGS turbulent diffusion terms are discussed in the next section.

According to equation (3.11) and (3.12), the SGS Reynolds stress and SGS turbulent heat flux are surface averages of products of SGS fluctuations. However, it is difficult to obtain the surface averages numerically, because field quantities are defined at node points. What we can do is model the SGS Reynolds stress and SGS turbulent heat flux at the node of each control volume based on volume averaging, and then interpolate them to control volume surfaces. With this in mind, we use the following expressions instead of equation (3.11) and (3.12):

$$\tau_{ij} = -\widetilde{u_i u_j} \tag{3.16}$$

$$\sigma_j = -\widetilde{\theta u_j}. \tag{3.17}$$

We assume that the error brought in due to this substitution is negligible.

3.4.1 Test-grid Volume Average

In order to model the SGS Reynolds stress and SGS turbulent heat flux expressed in equations (3.16) and (3.17) dynamically, consider the following expressions for the volume averages of products of decomposed fields for a control volume:

$$\widetilde{U_iU_j} = (\widetilde{U_i} + u_i)\widetilde{(U_j} + u_j) = \widetilde{U_i}\widetilde{U_j} + \widetilde{u_iu_j} \tag{3.18}$$

$$\widetilde{\Theta U_j} = (\tilde{\Theta} + \theta)\widetilde{(U_j} + u_j) = \tilde{\Theta}\widetilde{U_j} + \widetilde{\theta u_j}. \tag{3.19}$$

Note that no cross-correlation terms appear in equations (3.18) and (3.19) due to the features of the volume average.

Then, at the same control volume, consider another so called test-grid volume average with a larger characteristic width Δ'. Generally, $\Delta' = 2\Delta$, where Δ is the characteristic width of the previously described control volume average (referred to as the sub-grid volume average). Thus, we have

$$\widehat{U_iU_j} = (\widehat{U_i} + u_i')\widehat{(U_j} + u_j') = \widehat{U_i}\widehat{U_j} + \widehat{u_i'u_j'} \tag{3.20}$$

and

$$\widehat{\Theta U_j} = (\hat{\Theta} + \theta)\widehat{(U_j} + u_j') = \hat{\Theta}\widehat{U_j} + \widehat{\theta u_j'} \tag{3.21}$$

where the "angle hat" denotes test-grid averaging. Further, upon rearrangement,

$$\tau_{ij} = -\widetilde{u_iu_j} = -\widetilde{U_iU_j} + \widetilde{U_i}\widetilde{U_j} \tag{3.22}$$

$$\sigma_j = -\widetilde{\theta u_j} = -\widetilde{\Theta U_j} + \tilde{\Theta}\widetilde{U_j} \tag{3.23}$$

and

$$\tau_{ij}' = -\widehat{u_i'u_j'} = -\widehat{U_iU_j} + \widehat{U_i}\widehat{U_j} \tag{3.24}$$

$$\sigma'_j = -\widehat{\theta' u'_j} = -\widehat{\Theta U_j} + \hat{\Theta}\widehat{U_j} \tag{3.25}$$

where τ'_{ij} and σ'_j are, respectively, the SGS Reynolds stress and the SGS turbulent heat flux at the test-grid level. By test-grid averaging equations (3.22) and (3.23) and subtracting them, respectively, from equations (3.24) and (3.25), the following equations are obtained:

$$T_{ij} = \tau'_{ij} - \widehat{\tau_{ij}} = \widehat{\widehat{U}_i \widehat{U}_j} - \widehat{\widehat{U}_i}\widehat{\widehat{U}_j} \tag{3.26}$$

$$S_j = \sigma'_j - \widehat{\sigma_j} = \hat{\tilde{\Theta}}\widehat{\widehat{U}_j} - \widehat{\tilde{\Theta}\widehat{U}_j} \tag{3.27}$$

where an important feature of the volume average approach, *i.e.* the supersedity which implies $\widehat{\widehat{(\cdot)}} = \widehat{(\cdot)}$, has been applied. The LHS of equation (3.26), denoted as T_{ij}, represents the difference of the SGS Reynolds stresses between test-grid and sub-grid levels. The LHS of equation(3.27), denoted as S_j, represents the difference of the SGS turbulent heat flux between test-grid and sub-grid levels. These inter-grid Reynolds stress and inter-grid turbulent heat flux are only related to large scale fields, and are calculable numerically by test-grid averaging the sub-grid averaged fields.

It is worthwhile to note that equations (3.26) and (3.27) are only valid for flows where space unevenness of the sub-grid averaged fields is caused purely by turbulent fluctuation rather than by a combination of turbulent fluctuation and field inhomogeneity in space. In order to validate them in the case of inhomogeneous flows, the sub-grid averaged fields are further decomposed as follows.

$$\widehat{U_i} = \overline{\overline{\widehat{U_i}}} + \tilde{u}_i$$

$$\tilde{\Theta} = \overline{\overline{\tilde{\Theta}}} + \tilde{\theta}$$

where $\overline{\overline{\widehat{U_i}}}$ and $\overline{\overline{\tilde{\Theta}}}$ are, respectively, the ensemble means of sub-grid volume averaged velocity and temperature fields, while $\tilde{u}_i$ and $\tilde{\theta}$ are homogeneous fluctuations about

them. For a stationary turbulent flow, the ensemble mean fields are time-independent and can be replaced by the time averaged fields and viewed as portions of the mean fields associated with flow inhomogeneity. We don't want the test-grid averages in equation (3.26) and (3.27) to be affected by the ensemble mean fields. In other words, the test-grid averages there should have a special feature that can distinguish homogeneous turbulence from inhomogeneous ensemble mean fields, and treat them separately. A mathematical interpretation of this feature is as follows:

$$\hat{\tilde{\Phi}} = \widehat{\bar{\tilde{\Phi}} + \tilde{\phi}} = \hat{\bar{\tilde{\Phi}}} + \hat{\tilde{\phi}} = \bar{\tilde{\Phi}} + \widehat{\tilde{\Phi} - \bar{\tilde{\Phi}}}.$$

Thus, equations (3.26) and (3.27) can be rewritten as follows:

$$T_{ij} = (\widehat{\tilde{U}_i - \bar{\tilde{U}}_i})(\widehat{\tilde{U}_j - \bar{\tilde{U}}_j}) - (\widehat{\tilde{U}_i - \bar{\tilde{U}}_i})(\widehat{\tilde{U}_j - \bar{\tilde{U}}_j}) \tag{3.28}$$

$$S_j = (\widehat{\tilde{\Theta} - \bar{\tilde{\Theta}}})(\widehat{\tilde{U}_j - \bar{\tilde{U}}_j}) - (\widehat{\tilde{\Theta} - \bar{\tilde{\Theta}}})(\widehat{\tilde{U}_j - \bar{\tilde{U}}_j}). \tag{3.29}$$

3.4.2 Coefficient Modelling

The derivation thereafter attempts to relate the SGS Reynolds stress τ_{ij} and SGS turbulent heat flux σ_j at the sub-grid level with those at the inter-grid level, *i.e.* T_{ij} and S_j. We first assume that their relationship can simply be expressed as

$$\tau_{ij} = K_{\tau_{ij}} T_{ij} \tag{3.30}$$

and

$$\sigma_j = K_{\sigma_j} S_j \tag{3.31}$$

where $K_{\tau_{ij}}$ and $K_{\sigma_{ij}}$ are coefficients to be determined dynamically by the model. For that purpose, we assume further that the magnitudes of each component of the Reynolds stress or turbulent heat flux obey a similar distribution upon the length scales of "eddies" which is expressed as

$$\frac{dF(x)}{dx} = f(x) = \begin{cases} A(\frac{x}{B})^2 e^{-2(\frac{x}{B})} & \text{if } x > 0 \\ 0 & \text{otherwise} \end{cases} \tag{3.32}$$

Figure 3.1 schematically shows the distribution function where B is the dominant length scale of the distribution,*i.e.* the length scale corresponding to the peak value A of the distribution function. We introduce two additional length scales on Figure 3.1. The symbol η represents the length scale of the smallest calculable turbulent fluctuation which can be estimated as

$$\eta = \sqrt{\widetilde{U_i}\widetilde{U_i}}\Delta t$$

where Δt is the step used for time marching in the numerical scheme applied. The symbol γ represents the characteristic length scale of the time averaging applied for calculating the ensemble mean fields — assuming the turbulent flow under consideration is stationary — appearing in equations (3.28) and (3.29), which can be calculated as

$$\gamma = N\eta$$

where N is the number of instantaneous fields to be time-averaged for calculating the ensemble mean fields. The reasons for selecting (3.32) as the distribution function are: 1) it is a one-peak non-negative function in the region $[0, \infty]$; 2) it has zero derivatives at each end of the function's domain. These features match well with typical wave number spectra of turbulent flows.

We refer to the range between η and γ as the dynamic length scale range of the

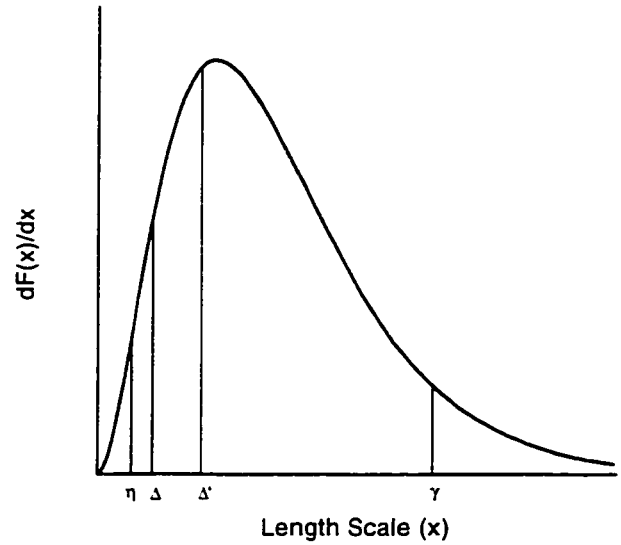

Figure 3.1: Dependence of Reynolds stress or turbulent heat flux upon length scale of "eddies"

LES technique. A perfect LES should be of $\eta < \Delta_i$ and $\gamma > L$, where Δ_i is the characteristic length scale of the control volume and L is the characteristic length scale of the solution domain. In the derivation thereafter, we assume $\eta < \Delta_i'$ and $\gamma > \Delta_i'$, where Δ_i' is the characteristic length scale of the test-grid average. This is the minimal requirement of the LES technique; otherwise, no SGS contribution can be captured. However, even this minimal requirement can not be satisfied at some specific locations where the flow speeds are too low.

It is also assumed that the corresponding components of the Reynolds stress or the turbulent heat flux at test-grid and sub-grid levels are the same in sign. Since values of self-correlations of SGS field fluctuations, including three for velocity components and one for temperature, are always positive, they can be used to determine the coefficients relating τ_{ij} to T_{ij} and σ_j to S_j. A detailed description of the procedure follows.

First of all, the self-correlation of any field fluctuation can be divided into portions according to its length scale distribution, which are the sub-grid portion, the

portion between sub-grid and test-grid, and the solvable portion. On the other hand, these portions can also be expressed in terms of definite integrations of the distribution function $f(x)$. Thus, for diagonal components of the SGS Reynolds stress, the following expressions hold:

$$-\tau_{ii} = \int_0^m f(x)dx = \frac{AB}{4} - \frac{AB}{4}[2(\frac{m}{B})^2 + 2(\frac{m}{B}) + 1]e^{-2(\frac{m}{B})} \tag{3.33}$$

$$\begin{aligned} -T_{ii} = \int_m^{\Delta'} f(x)dx &= \frac{AB}{4}[2(\frac{m}{B})^2 + 2(\frac{m}{B}) + 1]e^{-2(\frac{m}{B})} \\ &- \frac{AB}{4}[2(\frac{\Delta'}{B})^2 + 2(\frac{\Delta'}{B}) + 1]e^{-2(\frac{\Delta'}{B})} \end{aligned} \tag{3.34}$$

$$\begin{aligned} -t_{ii} = \int_m^{\gamma} f(x)dx &= \frac{AB}{4}[2(\frac{m}{B})^2 + 2(\frac{m}{B}) + 1]e^{-2(\frac{m}{B})} \\ &- \frac{AB}{4}[2(\frac{\gamma}{B})^2 + 2(\frac{\gamma}{B}) + 1]e^{-2(\frac{\gamma}{B})} \end{aligned} \tag{3.35}$$

where

$$m = \max(\Delta, \eta)$$

and no summation convention is employed.

In the above derivation, Δ, the characteristic length scale of averaging, has been mentioned twice. However, they should be specified in terms of Δx_i in the simulation. It should be pointed out that although the volume average version of τ_{ij} is calculated at the nodes of each control volume, they will finally be interpolated to control volume surfaces to represent the surface average value of the SGS Reynolds stresses there. In this sense, the length scales for each τ_{ij} should be calculated based on the corresponding surfaces used for averaging. Thus, three characteristic length scales corresponding to three Cartesian directions are used in the present simulation *i.e.*

$$\Delta = \Delta_1 = \sqrt{\Delta y \Delta z},$$

$$\Delta = \Delta_2 = \sqrt{\Delta x \Delta z},$$

and

$$\Delta = \Delta_3 = \sqrt{\Delta x \Delta y}.$$

It is noted that T_{ii} is directly available in the simulation procedure, and t_{ii} can be approximated as

$$t_{ii} = -(\widetilde{U_i} - \widehat{\widetilde{U_i}})^2.$$

So, for each characteristic length scale Δ_j, $\bar{B}_j = \frac{B}{\Delta_j}$ can be solved from the following equation obtained from equations (3.34) and (3.35):

$$\frac{[2(\frac{2}{\bar{B}_j})^2 + 2(\frac{2}{\bar{B}_j}) + 1]\exp[2(\frac{\bar{\gamma}_j - 2}{\bar{B}_j})] - [2(\frac{\bar{\gamma}_j}{\bar{B}_j})^2 + 2(\frac{\bar{\gamma}_j}{\bar{B}_j}) + 1]}{[2(\frac{\bar{m}_j}{\bar{B}_j})^2 + 2(\frac{\bar{m}_j}{\bar{B}_j}) + 1]\exp[2(\frac{\bar{\gamma}_j - \bar{m}_j}{\bar{B}_j})] - [2(\frac{\bar{\gamma}_j}{\bar{B}_j})^2 + 2(\frac{\bar{\gamma}_j}{\bar{B}_j}) + 1]} = \frac{t_{ii} - T_{ii}}{t_{ii}} \tag{3.36}$$

where

$$\bar{m}_j = \frac{m}{\Delta_j}$$

and

$$\bar{\gamma}_j = \frac{\gamma}{\Delta_j}.$$

Finally, the coefficient C_{ij} which represents the ratio of τ_{ii} over T_{ii} along the j-direction can be obtained from equations (3.33) through (3.35). Thus,

$$C_{ij} = (\frac{t_{ii}}{T_{ii}})\frac{\exp[2(\frac{\bar{m}_j}{\bar{B}_j})] - [2(\frac{\bar{m}_j}{\bar{B}_j})^2 + 2(\frac{\bar{m}_j}{\bar{B}_j}) + 1]}{[2(\frac{\bar{m}_j}{\bar{B}_j})^2 + 2(\frac{\bar{m}_j}{\bar{B}_j}) + 1] - [2(\frac{\bar{\gamma}_j}{\bar{B}_j})^2 + 2(\frac{\bar{\gamma}_j}{\bar{B}_j}) + 1]\exp[-2(\frac{\bar{\gamma}_j - \bar{m}}{\bar{B}_j})]}. \tag{3.37}$$

The terms C_{ij} thus obtained are applied to calculate $K_{\tau_{ij}}$ as

$$K_{\tau_{ij}} = \sqrt{C_{ij}C_{jj}}. \tag{3.38}$$

Following the same procedure, another coefficient $C_{\theta j}$ can be calculated based on the length scale distribution of the auto correlation of the SGS temperature fluctua-

tion. Thus, K_{σ_j} can be expressed as

$$K_{\sigma_j} = \sqrt{C_{\theta j} C_{jj}}. \tag{3.39}$$

3.5 Models for SGS Turbulent Diffusion

In this section, the models for the SGS turbulent diffusion are discussed in detail, beginning with the concept itself. The idea is related to the understanding of the turbulent transport enhancement mechanism of not only the LES but also the RAM method.

Let's first consider the RAM method of turbulent flows. It is well known that turbulence in a flow can greatly enhance the transport of any scalar or vector quantities. According to the Reynolds averaged equation (Reynolds, 1895) for a transported quantity Φ, the turbulent transport enhancement comes uniquely from the correlation between the turbulent fluctuation of the transported quantity, ϕ, and that of the velocity, u_i, which can be expressed as $\overline{\phi u_i}$. Both of the cross-correlation terms, *i.e.* $\overline{\phi \bar{U}_i}$ and $\overline{\bar{\Phi} u_i}$ vanish because there is no correlation between mean values and turbulent fluctuations. This form of the Reynolds averaged equation has been used for a century without doubting its validity. However, a comparison with molecular transport (diffusion) suggests that the correlation $\overline{\phi u_i}$ does not represent all of the turbulent transport enhancement mechanism. Let's take a look at how random molecular motion enhances the transport (diffusion). A molecular motion is definitely not correlated with any fluctuation of transported quantities, but it does enhance the transport (diffusion). The same principle should also be valid for a turbulent motion. In the case that the turbulent velocity fluctuations are not correlated with the fluctuation of the transported quantity, *i.e.* $\overline{\phi u_i} = 0$, transport should still be enhanced by the turbulent motion in the same way as by a molecular motion. A

typical example of the case is what happens when ink drops into a highly disturbed body of water. Initially, the concentration field of the ink in the water is apparently not correlated with the fluctuation of velocity, but a high rate of diffusion can be observed, which is definitely due to the turbulent fluctuations in the water. It can be concluded that turbulent fluctuations enhance transport via two mechanisms, which will be referred to as the turbulent diffusion and the turbulent flux. The former is analogous to molecular diffusion and is an example of gradient transport, while the latter is the one already involved in the Reynolds averaged equation which is correlation associated. Nevertheless, it should be noted that almost all of the RAM methods interpret the effect of the turbulent flux $\overline{\phi u_i}$ as diffusion transport and model it in terms of an eddy diffusivity with empirically determined coefficients. This makes the two transport enhancement mechanisms the same in form so that no problems occur when they are combined. In this sense, the identification of the turbulent diffusion as distinct has only academic rather than practical significance in the RAM theory.

The counterpart of the turbulent diffusion in the LES method is the so called SGS turbulent diffusion which represents a SGS transport enhancement mechanism other than that represented by τ_{ij} or σ_j. It is apparent that if one tries to model τ_{ij} or σ_j in terms of eddy diffusivity SGS models with adjustable coefficients, the identification of the SGS turbulent diffusion is of no practical significance. However, in the present study, all components of both τ_{ij} and σ_j are modelled dynamically without using any empirical coefficient. Therefore, in order to model all the transport enhancement mechanism, it is necessary to identify and model the SGS turbulent diffusion in the VAT for the turbulent flow simulation.

It is noted that only the SGS velocity fluctuations normal to the surface of a control volume are responsible for the SGS turbulent diffusion across that surface. In order to model the SGS turbulent diffusion, let's consider a near-surface region between two neighbouring control volumes shown in Figure 3.2.

On the area of the control volume surface, u_j, could be positive or negative. We

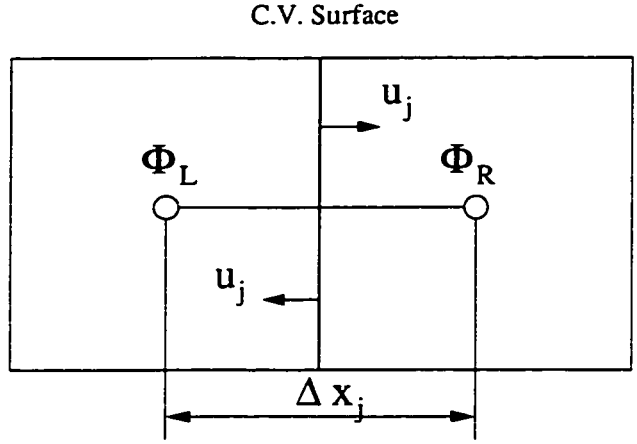

Figure 3.2: Near-surface Region of Two Neighbouring Control Volumes

assume that u_j is positive on half of the area, and is negative on the other half. We also assume that positive and negative u_j have the same mean magnitude denoted as $\breve{u}_j$. Therefore, in analogy to molecular diffusion, the pure flux of $\tilde{\Phi}$ across the control volume surface j due to the SGS fluctuation u_j can be expressed as

$$\frac{1}{2}\breve{u}_j \frac{\tilde{\Phi}_R - \tilde{\Phi}_L}{\Delta x_j}\overline{\Delta_j} \tag{3.40}$$

where $\overline{\Delta_j}$ is the mean length scale of the SGS fluctuation u_j; Δx_j, the distance between the nodes of two neighbouring control volumes. It is convenient to introduce the SGS eddy diffusivity α_j as

$$\alpha_j = \frac{1}{2}\breve{u}_j\overline{\Delta_j}. \tag{3.41}$$

At a control volume node, $\overline{\Delta_j}$ can be estimated as the length scale corresponding to the geometric center of the area under the functional plot $f(x)$ within the SGS range $[0, m_j]$ (refer to Figure 3.1). So that,

$$\overline{\Delta_j} = \frac{\int_0^{m_j} x f(x)dx}{\int_0^{m_j} f(x)dx} =$$

$$[\frac{3\bar{B}_j}{2}]\{\frac{\exp[2(\frac{\bar{m}_1}{\bar{B}_j})] - [\frac{4}{3}(\frac{\bar{m}_1}{\bar{B}_j})^3 + 2(\frac{\bar{m}_1}{\bar{B}_j})^2 + 2(\frac{\bar{m}_1}{\bar{B}_j}) + 1]}{\exp[2(\frac{\bar{m}_1}{\bar{B}_j})] - [2(\frac{\bar{m}_1}{\bar{B}_j})^2 + 2(\frac{\bar{m}_1}{\bar{B}_j}) + 1]}\}. \tag{3.42}$$

$\breve{u}_j$ can be modelled as

$$\breve{u}_j = \sqrt{-\tau_{jj}}.$$

Thus, the SGS turbulent diffusion across the surface can be modelled as

$$\alpha_j \frac{\dot{\Phi}_R - \dot{\Phi}_L}{\Delta X_j}. \tag{3.43}$$

Finally, we obtain the following models for the SGS turbulent diffusion terms in equations (3.14) and (3.15):

$$\xi_{ij} = \alpha_j \frac{\widetilde{U}_i^{j+\frac{1}{2}} - \widetilde{U}_i^{j-\frac{1}{2}}}{\Delta X_j} \tag{3.44}$$

$$\psi_j = \alpha_j \frac{\tilde{\Theta}^{j+\frac{1}{2}} - \tilde{\Theta}^{j-\frac{1}{2}}}{\Delta X_j}. \tag{3.45}$$

Numerically, it is convenient to include the SGS turbulent diffusion by combining the eddy diffusivity α_i $(i = 1, 2, 3)$ with the molecular viscosity ν or molecular thermal diffusivity α. Attention must be paid to the fact that the eddy diffusivity components α_i $(i = 1, 2, 3)$ are anisotropic.

3.6 Discussion

In the formulation of the VAT for turbulent flow simulation, the main contribution is a new SGS model. Since both the coefficients $K_{\tau_{ij}}$ and K_{σ_j} appearing in the model are calculated by postulating a functional distribution of the Reynolds stress or turbulent

heat flux over the length scale of eddies, and the model is similar in form to Bardina's scale similarity SGS model. it is referred to as the functional scale similarity SGS model in the present study. In this section, some comments regarding features of the newly developed LES technique are provided. Whenever it is helpful, comparison between this technique and the ones previously developed are made.

First of all, the reason for avoiding the attributive "large-eddy" in the title of this thesis is given. The attributive "large-eddy" may be misleading because in some cases the important flow structures to be resolved are extremely small, such as those near solid walls, and are at the dissipation scale. Thus, there is no clearly defined length scale gap between large and small eddies. Secondly, as was pointed out in section 3.3, there is actually no means for one to select the characteristic length scale Δ_i when the volume averaging approach is employed; it is uniquely determined by the length scales of each finite control volume for space discretization. It seems that the volume average — a procedure for the finite volume space discretization — determines every thing. In this context, the LES is better referred to as "larger-than-grid-size eddy simulation" or simply "volume average simulation". Thus, the technique developed for it can be referred to as the volume average technique or VAT in short.

It should be noted that like other dynamic SGS models, the sub-grid effect represented by the functional scale similarity SGS model comes from the inter-grid turbulent fluctuations, *i.e.* the turbulent fluctuations with length scales from Δ_i to Δ_i'. In order to calculate it, the solvable sub-grid averaged fields are treated by using the test-grid averaging procedure. The original purpose of this procedure is to separate the inter-grid turbulent fluctuations from the solvable sub-grid averaged fields. A solvable sub-grid averaged field involves not only turbulent fluctuations with length scales larger than Δ_i, but also the corresponding mean field. In the case of inhomogeneous turbulent flow, the mean field itself is spatially changing but this is not turbulent fluctuation by nature. However, the previous dynamic SGS models or dynamic mixed models treat it as a turbulent fluctuation since they treat the solvable sub-grid averaged field as a whole. A consequence of this approach is apparent: the

simulation result is strongly grid-dependent and has poor asymptotic behaviour on the laminar side. The situation becomes worse when a coarser grid is applied. In the functional scale similarity SGS model, mean fields are first removed from the corresponding solvable sub-grid averaged fields. Then, the residual fields are treated. The residual fields represent only the turbulent fluctuations with length scales larger than Δ_i from which the effect of pure inter-grid turbulent fluctuations can be picked up. This treatment can be viewed as an important advantages of the functional scale similarity SGS model.

The identification and modelling of the SGS turbulent diffusion is an important feature of the VAT. The SGS eddy diffusivity derived on the basis of this newly developed concept is distinct in nature to that proposed before, because in the present study, the SGS eddy diffusivity α_i represents the SGS turbulent diffusion rather than a substitute for the turbulent flux. Additionally, instead of being related to the magnitude of the resolved strain rate, the α_i in the present study is associated with the SGS velocity fluctuations u_i which vanish in the case of laminar flow. Thus, good asymptotic behaviour of the technique can be expected. Furthermore, since the SGS eddy diffusivity α_i is always positive, it introduces the high energy dissipation rate which is required for the LES and which was not brought in by Bardina's original scale similarity SGS model.

Anisotropy is another important feature of the functional scale similarity SGS model of the VAT, which is essential in LES of wall-bounded flows. The anisotropy comes from: 1) the full-component modelling of τ_{ij} and σ_j and, 2) the surface-based definition of the characteristic length scales Δ_i in each control volume. As was pointed out in chapter 2, the full-component modelling of τ_{ij} and σ_j is logically more accurate than most other SGS models previously developed. On the other hand, the surface-based definition of the characteristic length scales can handle different cut-off length scales of the volume average in different coordinate directions, therefore allowing one to use highly non-uniform grids and/or control volumes with high aspect ratio in the LES, which are frequently adopted in near-wall regions.

Dynamically determining the ratios between the Reynolds stress or turbulent heat flux of the sub-grid level and those of the inter-grid level is a key procedure in the functional scale similarity SGS model of the VAT. It is interesting to note that if both $K_{\tau_{ij}}$ and K_{σ_j} were fixed to be $\frac{1}{3}$, a limiting case when $\Delta_i \ll B_i$ and $\eta = 0$ (and $\Delta_i' = 2\Delta_i$), it would imply that the SGS Reynolds stress or SGS turbulent heat flux at both sub-grid and test-grid levels are proportional to the squares of the characteristic length scales of averaging. This fact is also deducible from the dynamic SGS model proposed by Germano *et al.*. In this sence, the functional scale similarity SGS model can be viewed as an extension of Germano's dynamic SGS model; the latter is only valid when the characteristic length scales of the volume averaging are extremely small compared to the dominant length scale of the turbulent eddies (see Appendix A.2). In this sense, using the functional scale similarity SGS model can alleviate the problem of computer resource shortage, because it allows using relatively large characteristic length scales of the volume averaging (even larger than the dominant length scale of turbulent eddies) in the LES.

Finally, let's focus our attention on the negative side of the VAT, mainly the modelling errors involved in the technique. As was mentioned in subsection 3.4.2, the so-called dynamic length scale range of the VAT is $[\eta, \gamma]$. Any fluctuation out of this range will be lost in the simulation. Thus, if the inter-grid length scale range is completely outside the dynamic length scale range, no SGS effect can be captured. This deficiency is not unique in the VAT, but a general problem for all dynamic modelling techniques of the LES.

The distribution function shown in figure 3.1 is essentially transformed from the one in wave number space by assuming that

$$X = \frac{2\pi}{k} \tag{3.46}$$

The characteristic length sales *i.e.* η, Δ_i, Δ_i', and γ are all defined in physical space. Figures 2.2 and 2.1 show that equation (3.46) only holds approximately, which will

introduce errors to the dynamically determined coefficients $K_{\tau_{ij}}$ and K_{σ_j}.

In the case where almost all turbulent fluctuations have length scales smaller than the characteristic length scale of the volume average, *i.e.* $B \ll \Delta$, the Reynolds stress or turbulent heat flux at the inter-grid length scale level will be extremely small compared to those at the sub-grid length scale level. But we actually model the latter from the former in the functional scale similarity SGS model, which is tantamount to conjecturing the whole iceberg from its above surface portion. An extreme situation occurs when the flow is laminar, but due to some numerical errors, the resolvable fields are still fluctuating in simulation. These random numerical fluctuations may be interpreted as turbulent fluctuations by the functional scale similarity SGS model. Even worse is that the random numerical fluctuations may lead to almost zero value of $(-t_{ii} + T_{ii})$ which will lead to extremely large values of the coefficients $K_{\tau_{ij}}$ or K_{σ_j}, and consequently to unreasonably high values of the SGS Reynolds stress or SGS turbulent heat flux. The phenomenon is referred to as numerical noise in the functional scale similarity SGS model in the present study. In order to avoid LES being contaminated by the numerical noise, we have to set both $K_{\tau_{ij}}$ and K_{σ_j} to zero whenever the obtained value of $(-t_{ii}+T_{ii})$ is too small compared with $-t_{ii}$. By doing this, an additional error is introduced.

3.7 Summary

The formulation for the VAT has been derived rigorously in this chapter. In particular, the functional scale similarity SGS model for the SGS Reynolds stress and SGS turbulent heat flux has been presented. In addition, the SGS turbulent diffusion, a transport enhancement mechanism analogous to molecular diffusion introduced by the coarse-graining procedure, is identified and modelled in terms of the sub-grid length scales and the RMS of the SGS turbulent fluctuation. The features of this newly developed technique are discussed in detail. The technique for numerical im-

plementation of the VAT in the LES is developed in the following chapter.

Chapter 4

Numerical Implementation

4.1 Introduction

In the previous chapter, in order to define large scale fields, the governing equations of fluid flow are volume averaged over control volumes. Meanwhile, the governing equations are discretized in space by the same volume average into a finite-difference form shown in equations (3.5) through (3.7). In this chapter, numerical schemes for the solution of these governing equations are discussed in detail. Firstly, starting from equations (3.5) through (3.7), a collocated scheme for 3-D incompressible flow is developed based on the fractional step and the SIMPLE methods.In the collocated scheme development, all SGS modelling terms, such as τ_{ij} *etc.*, are assumed to be known. Although the scheme is specifically designed to facilitate the LES procedure in the frame of the finite volume method, it can also be applied, without any change, to laminar flow simulations or the DNS of turbulence, and can be applied, with a

turbulence model, to the RAM simulation of turbulence. Secondly, some specifically designed schemes associated with SGS modelling procedure are described. Thirdly, approaches for boundary condition specification in the present study are given. Finally, the code designed to realize the volume average technique is discussed.

4.2 Collocated Scheme for Incompressible Flows

4.2.1 Background

An efficient and accurate numerical scheme for solving the governing equations of fluid flow is the key to the success of the LES method. Such a scheme should be three-dimensional, time-accurate, and save computer memory and CPU time. Numerical schemes for the approximate solution of the incompressible Navier-Stokes equations have been investigated rather extensively in the last two decades. These numerical schemes can be classified, according to the discretization techniques employed, as the finite-difference (including finite-volume), finite-element, and spectral methods, or according to the forms of the governing equations on which the numerical scheme is based, as the primitive-variable or non-primitive-variable methods. The finite-difference scheme based on the primitive-variable Navier-Stokes equations has been the most popular numerical method for computation of 3-D incompressible flows.

Although several different approaches for solving the primitive-variable incompressible Navier-Stokes equations have been developed, according to Quartapelle (1993), the most elegant and powerful one, and perhaps the only one to be recommended without any reservation and to enable a cost-effective solution is the fractional-step method. The fractional-step method was proposed independently by Chorin (1968) and by Teman (1969). Basic to the derivation of the fractional-step method is a theorem of orthogonal decomposition due to Ladyzhenskaya (1969). The typical form

of the time-discretized equations of this method consists of two distinct steps. First, a provisional velocity field, not satisfying the condition of incompressibility, is calculated as a solution of the discretized version of the momentum equation without a pressure gradient. Then, the provisional velocity field is decomposed into the sum of a solenoidal (divergence-free) velocity and the gradient of a scalar function proportional to the unknown pressure which can be solved from a derived Poisson equation for pressure. In the sense of time-stepping, the SIMPLE (Semi-Implicit Method for Pressure-Linked Equation) method of Patankar and Spalding (1972) for the solution of incompressible flows is actually a special version of the fractional-step method. In SIMPLE, the real pressure is decomposed into an old value (given by the previous estimate) and its correction. The estimated pressure is included in the momentum equation, while only the pressure correction is involved in the second step. Thus, the provisional velocity obtained is decomposed into the sum of a solenoidal velocity field and the gradient of a scalar function proportional to the unknown pressure correction. Since the pressure correction field is much smaller than the pressure field, this fractional-step version has the following advantages: the tangential components of the velocity boundary condition can be exactly satisfied; and the Poisson equation can be solved more accurately with the same solver.

The nature of the volume average technique for turbulent flow simulation requires that a finite-volume scheme based on the primitive-variable Navier-Stokes equations be applied in the present study. The SIMPLE algorithm turns out to be a finite-volume scheme and, as was mentioned above, is a version of the powerful fractional-step methods for solving the primitive-variable Navier-Stokes equations. However, an unwanted feature of the SIMPLE method is the use of a staggered grid arrangement to avoid the spurious pressure mode caused by uncoupled networks of pressure points, which is inconvenient for programming. This is especially the case when the flow under consideration is 3-D, which requires a four-control-volume staggered grid configuration, and a non-uniform or adaptive grid is employed. It is apparent that the staggered grid arrangement is not suitable for the dynamic SGS modelling procedures of the LES method in which two grid systems, *i.e.* a subgrid system and a test

grid system, are dealt with simultaneously. Therefore, a collocated or non-staggered finite-volume scheme, in which all field quantities are located at the same node point, is needed for the LES of turbulent flows.

There have been several collocated numerical schemes reported in the literature. Only two types of these schemes can be implemented in a way which mimics the SIMPLE scheme. One was originally proposed by Rhie and Chow (1983) and subsequently modified by Peric *et al.* (1988), Majumdar (1988), Miller *et al.* (1988), and Armfield (1991). To ensure velocity-pressure coupling, all of these methods apply a so called Pressure-Weighted Interpolation (PWI) scheme to obtain the flux velocity at each surface of a control volume by adding a sparse 2Δ gradient and subtracting a compact 1Δ gradient of the pressure to the corresponding linear interpolation of the node velocities. The flux velocity thus obtained is used in the continuity equation and this prevents the occurrence of "checkerboard" pressure modes. The other so called Consistent Physical Interpolation (CPI) scheme was originally proposed by Schneider and Raw (1987) in their development of a finite-element-oriented scheme for non-staggered control volumes. The name CPI, however, was given by Deng *et al.* (1994) who extended the scheme to a finite-difference formulation. A key point of the CPI scheme is viewing the reconstruction of the flux velocity at the control-volume cell face as a closure problem; additional equations are employed to "close" the algebraic representation of the conservation equations. The closure equations used should include all of the relevant physical influences that can affect the control-volume cell face flux velocities. It should be pointed out that the closure equations applied for the CPI schemes have no transient terms, thus the CPI scheme is not time accurate and is only valid for steady-state problems.

The present study uses the SIMPLE scheme as the starting point for the development of the numerical scheme. Three changes have been made to the conventional SIMPLE scheme. Firstly, the scheme is collocated, so that all field quantities are defined at cell-centred nodes. In order to ensure velocity-pressure coupling, a provisional velocity field is calculated at nodes from the momentum equations with the pressure

terms eliminated. Then, the flux velocities on the surfaces of each control volume are obtained by subtracting the 1Δ gradient of the pressure from the interpolated provisional velocities at the control volume surfaces. The flux velocities are applied at the RHS of the Poisson equations for the pressure correction, and the 2Δ gradient of the corrected pressure field is subtracted from the node-located provisional velocity to obtain the new velocity field. Secondly, a 1-D QUICK (Quadratic Upstream Interpolation for Convective Kinematic) scheme is employed for the transported variables at the surfaces of each control volume. The QUICK scheme is believed to be able to reduce the false diffusion which may contaminate the accuracy of the SGS modelling. Thirdly, the efficiency of the method is enhanced by using the PRIME (update PRessure Implicit, Momentum Explicit) algorithm, so that the solver of the linear system is only employed for the Poisson equation and the energy equations. A detailed description of the scheme is given below.

4.2.2 Finite Volume Discretization

In our numerical simulation, the original form of the basic equations was considered as opposed to its dimensionless form. The general form of the governing equations shown in equations (3.5) through (3.7) can be expressed as:

$$\dot{\Phi} + \delta_j(U_j\Phi - \Gamma\Phi_{,j}) = S_\phi. \tag{4.1}$$

For $\Phi = 1$ and $\Gamma = 0$, one obtains the continuity equation; for $\Phi = U_i$ and $\Gamma = \nu$, one obtains the momentum equation; while for $\Phi = \Theta$, $\Gamma = \alpha$, and $S_\phi = 0$, one obtains the energy equation. It should be mentioned that in this chapter we handle only the volume averaged quantities. However, the symbols "$\sim$" are all dropped for brevity.

Applying the following time average over a time increment Δt,

$$\frac{1}{\Delta t}\int_t^{t+\Delta t} \Phi dt$$

to equation (4.1), we have

$$\frac{(\Phi^1 - \Phi^0)}{\Delta t} + \delta_j(U_j\Phi - \Gamma\Phi_{,j}) = S_\phi \tag{4.2}$$

where the superscripts "0" and "1" denote the values of fields at time "t" and "$t+\Delta t$", respectively, and the symbols without superscript refer to time averaged quantities between time t and $t + \Delta t$. Multiplying both sides of equation (4.2) with ΔV, the volume of the control volume, gives

$$(\Phi^1 - \Phi^0)(\frac{\Delta V}{\Delta t}) + J_e A_e - J_w A_w + J_n A_n - J_s A_s + J_t A_t - J_b A_b = S_\Phi \Delta V \tag{4.3}$$

where J_i denotes the total flux of Φ, *i.e.* convection and diffusion, through control volume surfaces, and the areas of the six control-volume surfaces are denoted by A_e *etc.*.

In the present study, only the flows in a regular cuboid room are considered. Therefore, the flow domain is discretized using Cartesian coordinates, and the control volumes obtained are all cuboid.

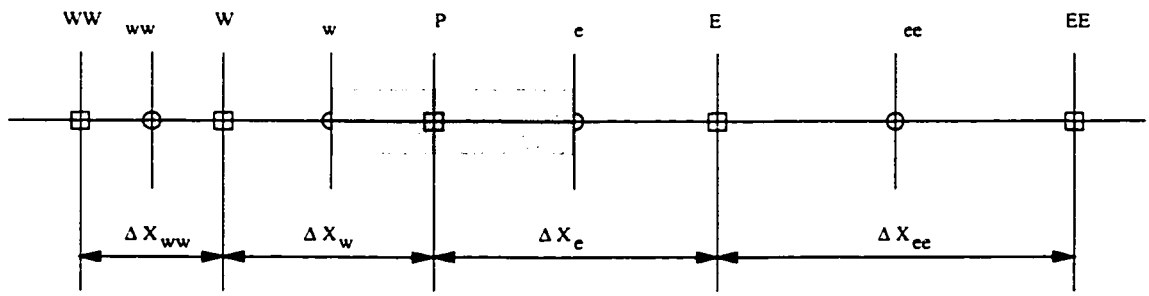

Figure 4.1: Grid configuration in X-direction

Figure 4.1 illustrates the grid configuration in the x-direction. Generally, finer grids are used in near-wall regions. All the unknown values including velocities, temperatures, pressures, the SGS Reynolds stress, *etc.* are calculated at nodal points marked with a "□". The points marked with a "o" are located on the surfaces of the control volumes. Node P is the central grid point on which one focuses attention. Nodes EE, E, W, WW denote the east and west neighbours of P. Each face is located midway between the two corresponding nodes.

In finite-volume discretization, the total fluxes J_i should be expressed in terms of the values of Φ at nodes. For illustration, we consider the x-direction fluxes which can be expressed in terms of convection and diffusion terms as follows:

$$J_e A_e = (\vec{U}_e \Phi_e - \Gamma_e \Phi_{,x}^e) A_e \tag{4.4}$$

$$J_w A_w = (\vec{U}_w \Phi_w - \Gamma_w \Phi_{,x}^w) A_w \tag{4.5}$$

where $\vec{U}_e$ and $\vec{U}_w$ represent, respectively, the flux velocities at east and west surfaces of the control volume. The diffusion terms can be directly discretized as

$$\Gamma_e \Phi_{,x}^e = \Gamma_e \left(\frac{\Phi_E - \Phi_P}{\Delta x_e}\right) \tag{4.6}$$

and

$$\Gamma_w \Phi_{,x}^w = \Gamma_w \left(\frac{\Phi_P - \Phi_W}{\Delta x_w}\right). \tag{4.7}$$

However, the convection terms are related to the flux velocities $\vec{U}_e$ and $\vec{U}_w$, and transported quantity Φ at control volume surfaces, which themselves are not directly available.

4.2.3 1-D QUICK Scheme

The 1-D QUICK scheme is applied to the convective terms in the momentum and energy equations to express Φ at control volume surfaces in terms of its values at the neighbouring nodes. Thus, for $\vec{U_e} > 0$, we have

$$\Phi_e = \left[\frac{1}{2} + \frac{1}{4}\frac{\Delta x_e}{\Delta x_w}\right]\Phi_P - \left[\frac{1}{4}\frac{{\Delta x_e}^2}{\Delta x_w(\Delta x_e + \Delta x_w)}\right]\Phi_W - \left[\frac{1}{4}\frac{\Delta x_e}{\Delta x_e + \Delta x_w}\right]\Phi_E + \underbrace{\frac{1}{2}\Phi_E}_{Source} \tag{4.8}$$

and

$$\Phi_w = \left[\frac{1}{2} - \frac{1}{4}\frac{\Delta x_w}{\Delta x_w + \Delta x_{ww}}\right]\Phi_P + \left[\frac{1}{2} + \frac{1}{4}\frac{\Delta x_w}{\Delta x_{ww}}\right]\Phi_W - \underbrace{\left[\frac{1}{4}\frac{{\Delta x_w}^2}{\Delta x_{ww}(\Delta x_w + \Delta x_{ww})}\right]\Phi_{WW}}_{Source} \tag{4.9}$$

while for $\vec{U_e} < 0$, we have

$$\Phi_e = \left[\frac{1}{2} - \frac{1}{4}\frac{\Delta x_e}{\Delta x_e + \Delta x_{ee}}\right]\Phi_P + \left[\frac{1}{2} + \frac{1}{4}\frac{\Delta x_e}{\Delta x_{ee}}\right]\Phi_E - \underbrace{\left[\frac{1}{4}\frac{{\Delta x_e}^2}{\Delta x_{ee}(\Delta x_e + \Delta x_{ee})}\right]\Phi_{EE}}_{Source} \tag{4.10}$$

and

$$\Phi_w = \left[\frac{1}{2} + \frac{1}{4}\frac{\Delta x_w}{\Delta x_e}\right]\Phi_P - \left[\frac{1}{4}\frac{{\Delta x_w}^2}{\Delta x_e(\Delta x_e + \Delta x_w)}\right]\Phi_E - \left[\frac{1}{4}\frac{\Delta x_w}{\Delta x_e + \Delta x_w}\right]\Phi_W + \underbrace{\frac{1}{2}\Phi_W}_{Source}. \tag{4.11}$$

The use of source terms in equations (4.8) through (4.11) is from Perng & Street (1989). These terms automatically adjust themselves to differently stretched grids and still ensure satisfaction of the "all-positive coefficients" rule. For brevity, equations (4.8) through (4.11) are represented by

$$\Phi_e = f_P^e\Phi_P + f_W^e\Phi_W + f_E^e\Phi_E + S_e \tag{4.12}$$

and

$$\Phi_w = f_P^w \Phi_P + f_W^w \Phi_W + f_E^w \Phi_E + S_w \tag{4.13}$$

where f_P^e *etc.* are referred to as the geometric factors, and S_e, *etc.*. are the source terms.

Substituting equation (4.8) through (4.13), as well as the corresponding expressions in the y and z directions, into equation (4.3), we obtain

$$\frac{\Delta V}{\Delta t}\Phi_P^1 + a_P \Phi_P = \sum_{NP} a_{NP}\Phi_{NP} + S_\Phi \Delta V + \frac{\Delta V}{\Delta t}\Phi_P^0 + b \tag{4.14}$$

where

$$a_P = \vec{U}_e f_P^e A_e - \vec{U}_w f_P^w A_w + \vec{V}_n f_P^n A_n - \vec{V}_s f_P^s A_s + \vec{W}_t f_P^t A_t - \vec{W}_b f_P^b A_b$$

$$+ \frac{(\Gamma A)_e}{\Delta x_e} + \frac{(\Gamma A)_w}{\Delta x_w} + \frac{(\Gamma A)_n}{\Delta y_n} + \frac{(\Gamma A)_s}{\Delta y_s} + \frac{(\Gamma A)_t}{\Delta z_t} + \frac{(\Gamma A)_b}{\Delta z_b} \tag{4.15}$$

and

$$b = -\vec{U}_e S_e A_e + \vec{U}_w S_w A_w - \vec{V}_n S_n A_n + \vec{V}_s S_s A_s - \vec{W}_t S_t A_t + \vec{W}_b S_b A_b \tag{4.16}$$

where the subscript NP denotes the neighbouring nodes E, W, N, S, T, B of the node P. The specific forms of the neighbour coefficients are given below:

$$a_E = -\vec{U}_e f_E^e A_e + \frac{(\Gamma A)_e}{\Delta x_e} + \vec{U}_w f_E^w A_w$$

$$a_W = \vec{U}_w f_W^w A_w + \frac{(\Gamma A)_w}{\Delta x_w} - \vec{U}_e f_W^e A_e$$

$$a_N = -\vec{V}_n f_N^n A_n + \frac{(\Gamma A)_n}{\Delta y_n} + \vec{V}_s f_N^s A_s$$

$$a_S = \vec{V}_s f_S^s A_s + \frac{(\Gamma A)_s}{\Delta y_s} - \vec{V}_n f_S^n A_n$$

$$a_T = -\vec{W}_t f_T^t A_t + \frac{(\Gamma A)_t}{\Delta z_t} + \vec{W}_b f_T^b A_b$$

$$a_B = \vec{W}_b f_B^b A_b + \frac{(\Gamma A)_b}{\Delta x_b} - \vec{W}_t f_B^t A_t.$$

For time stepping, assume:

$$\Phi_P = \Phi_P^1 \quad (implicit)$$

and

$$\Phi_{NP} = \Phi_{NP}^0 \quad (explicit).$$

Therefore, the following semi-implicit scheme is obtained:

$$\Phi_P^1 = \frac{(\sum a_{NP}\Phi_{NP}^0 + b + S_{\Phi_P}\Delta V)^{(0)} + \frac{\Delta V}{\Delta t}\Phi_P^0}{(\frac{\Delta V}{\Delta t} + a_P)^{(0)}} \tag{4.17}$$

where the superscript "(0)" denotes that coefficients in parenthesis are calculated using the field quantity values at time step "t". Equation (4.17) is applied for the solution of both momentum and energy equations.

4.2.4 Pressure Correction Scheme

The continuity equation (3.5) can be rewritten as:

$$\vec{U}_e A_e - \vec{U}_w A_w + \vec{V}_n A_n - \vec{V}_s A_s + \vec{W}_t A_t - \vec{W}_b A_b = 0 \tag{4.18}$$

where only six flux velocities appear. The flux velocities play an important role in coupling the continuity equation with the momentum equation. In the collocated scheme, we actually relate the flux velocities to the nodal velocities which are solved from the momentum equation, while information from the continuity equation is sent back to the nodal velocities via the flux velocities.

The information from the continuity equation is represented by a pressure correction field P' superimposed on the pressure field P. Each corrected flux velocity can be expressed as a sum of the corresponding pre-corrected flux velocity and the pressure correction term. *e.g.*

$$\vec{U}_e = \vec{U}_e{}' - \frac{A_e(P'_E - P'_P)}{(a_P + \frac{\Delta V}{\Delta t})_e}.$$

By substituting the above and other velocity correction relations written at six surface points into the discretized form of the continuity equation, we obtain

$$\frac{P'_E - P'_P}{(a_P + \frac{\Delta V}{\Delta t})^e} A_e^2 - \frac{P'_P - P'_W}{(a_P + \frac{\Delta V}{\Delta t})^w} A_w^2 +$$

$$\frac{P'_N - P'_P}{(a_P + \frac{\Delta V}{\Delta t})^n}) A_n^2 - \frac{P'_P - P'_S}{(a_P + \frac{\Delta V}{\Delta t})^s}) A_s^2 +$$

$$\frac{P'_T - P'_P}{(a_P + \frac{\Delta V}{\Delta t})^t}) A_t^2 - \frac{P'_P - P'_B}{(a_P + \frac{\Delta V}{\Delta t})^b}) A_b^2$$

$$= \vec{U}_e{}' A_e - \vec{U}_w{}' A_w + \vec{V}_n{}' A_n - \vec{V}_s{}' A_s + \vec{W}_t{}' A_t - \vec{W}_b{}' A_b \qquad (4.19)$$

where the $1/\rho_0$ has been absorbed into the P'_P, *etc.* for brevity. Finally, we rewrite equation (4.19) in the following form:

$$a'_P P'_P = a'_W P'_W + a'_E P'_E + a'_S P'_S + a'_N P'_N + a'_B P'_B + a'_T P'_T + b' = \sum a'_{NP} P'_{NP} + b' \quad (4.20)$$

where

$$a'_W = \frac{A_w^2}{(a_P + \frac{\Delta V}{\Delta t})^w}; \quad a'_E = \frac{A_e^2}{(a_P + \frac{\Delta V}{\Delta t})^e}; \quad a'_S = \frac{A_s^2}{(a_P + \frac{\Delta V}{\Delta t})^s}$$

$$a'_N = \frac{A_n^2}{(a_P + \frac{\Delta V}{\Delta t})^n}; \quad a'_B = \frac{A_b^2}{(a_P + \frac{\Delta V}{\Delta t})^b}; \quad a'_T = \frac{A_t^2}{(a_P + \frac{\Delta V}{\Delta t})^t}$$

$$a'_P = a'_W + a'_E + a'_S + a'_N + a'_B + a'_T$$

$$b' = -\vec{U_e}' A_e + \vec{U_w}' A_w - \vec{V_n}' A_n + \vec{V_s}' A_s - \vec{W_t}' A_t + \vec{W_b}' A_b.$$

The coefficients $(a_P)_e$, *etc.*. appearing in (4.19) are obtained through a linear interpolation between the corresponding neighbouring nodes, *e.g.*

$$(a_P + \frac{\Delta V}{\Delta t})_e = \frac{1}{2}[(a_P + \frac{\Delta V}{\Delta t})_P + (a_P + \frac{\Delta V}{\Delta t})_E]. \tag{4.21}$$

4.2.5 Fractional Step Method

Having described the discrete equations above, we begin to discuss in detail the solution procedure of the collocated scheme. For each control volume, we store three components of velocity U_i, temperature Θ, and pressure P at the node, and six flux velocities $\vec{U_e}$, *etc.* at the control volume surfaces. A single discrete time step is split into three sub-steps.

Firstly, a provisional velocity U_i^* is calculated at each node using the scheme expressed in (4.17) for the momentum equations without any pressure terms, *i.e.*

$$(U_i)_P^* = \frac{(\sum a_{NP}(U_i)_{NP} + b + (S_P)'\Delta V)^{(0)} + \frac{\Delta V}{\Delta t}(U_i)_P^{(0)}}{(\frac{\Delta V}{\Delta t} + a_P)^{(0)}} \tag{4.22}$$

where $(S_P)'$ denotes source terms without considering the pressure gradient.

Secondly, the flux velocities at the control volume surfaces are computed and updated by adding the corresponding pressure gradient terms to the linearly interpolated

provisional velocities at the surfaces, *e.g.*

$$\vec{U}_e = \frac{1}{2}[(U_1)_P^* + (U_1)_E^*] - \frac{A_e(P_E - P_P)}{(a_P + \frac{\Delta V}{\Delta t})_e} \tag{4.23}$$

where $(a_P + \frac{\Delta V}{\Delta t})$ is obtained from equation (4.21). By substituting the updated flux velocities into the pressure correction equation (4.20) and solving it implicitly for the pressure correction field P', the new pressure field P^1 at control volume nodes can be obtained as:

$$P^1 = P + (P' - P'_r)$$

where P'_r is the calculated pressure correction at a reference point in the domain where the pressure is assumed to be unchanged.

Thirdly, the new velocity fields at control volume nodes can be obtained as

$$U_P = U_P^* - \left(\frac{\Delta V}{a_P + \frac{\Delta V}{\Delta t}}\right)_P \frac{(P_E - P_W)}{\Delta x_e + \Delta x_w}, \tag{4.24}$$

$$V_P = V_P^* - \left(\frac{\Delta V}{a_P + \frac{\Delta V}{\Delta t}}\right)_P \frac{(P_N - P_S)}{\Delta x_n + \Delta x_s}, \tag{4.25}$$

and

$$W_P = W_P^* - \left(\frac{\Delta V}{a_P + \frac{\Delta V}{\Delta t}}\right)_P \frac{(P_T - P_B)}{\Delta x_t + \Delta x_b}. \tag{4.26}$$

And the flux velocities on control volume surfaces are updated again, *e.g.*

$$\vec{U}_e^{\,1} = \vec{U}_e - \frac{A_e(P'_E - P'_P)}{(a_P + \frac{\Delta V}{\Delta t})_e}. \tag{4.27}$$

Finally, the energy equation can be solved implicitly or explicitly with the above updated flux velocities based on the equation (4.14).

In the collocated scheme, the momentum equation (4.22) can be solved explicitly,

because its RHS is only related to the fields at the old time step "0". This so called PRIME feature significantly enhances the solution efficiency of the scheme. Additionally, the collocated scheme has second-order accuracy in both space and time, because in the scheme, the flux velocities on control volume surfaces are updated twice in one time step and the QUICK is employed for surface transported quantities.

4.2.6 ADLGS Solver and Residuals

In the present study, The ADLGS (Alternate Direction Line Gauss-Seidel) solver is applied for solving the pressure correction Poisson equations. One advantage of this solver is that almost no memory space in addition to that for eight finite-difference coefficients for each control volume is required. A factor of 1.6 is used in the solver to over-relax the field values at the neighbouring nodes located on the down-sweeping side.

In the solution procedure, two residuals, *i.e.* the mass residual R_m and the residual for the pressure correction Poisson equation R_p are calculated at each time step. The definitions of the residuals are as follows:

$$R_m = \frac{1}{N}\sum_{1}^{N}\frac{|b'|}{\Delta V}$$

$$R_p = \frac{1}{N}\sum_{1}^{N}\left|\frac{a'_P P'_P - \sum a'_{NP} P'_{NP}}{a'_P P'_P}\right|$$

where N is the total number of control volumes in the domain.

4.3 Numerical Schemes for SGS Modelling

4.3.1 Test-grid Volume Average

The configuration of the test-grid control volume is depicted in Figure 4.2. Note that for brevity, the figure only shows a two-dimensional grid. The upper case letters represent the nodes in and around the sub-grid control volume under consideration, while the low case letters represent its surface points. The surfaces of the corresponding test-grid control volume coincide with the neighbouring nodes of the node P, so that the test-grid control volume doubles the size of the corresponding sub-grid control volume in each coordinate direction.

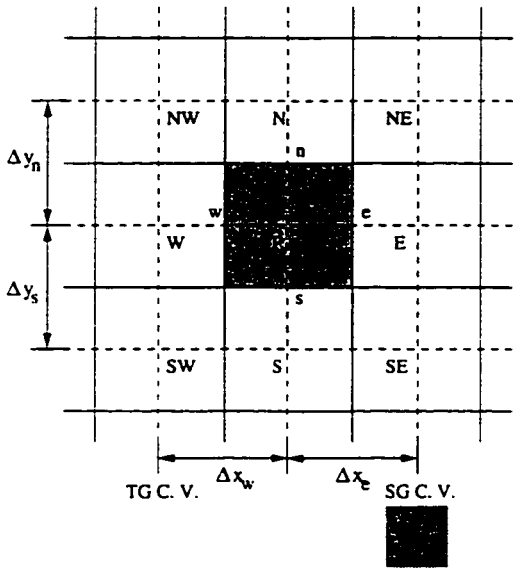

Figure 4.2: Grid configuration for dynamic SGS modelling

In order to calculate the SGS Reynolds stress and turbulent heat flux, the sub-grid volume averaged fields which are obtained directly by solving the sub-grid volume averaged governing equations should be averaged over the test-grid control volume

where the values of the sub-grid averaged fields at 27 nodes are involved, *i.e.*

$$\widehat{\widetilde{\Phi_P}} = \sum \mathcal{K}_n \widetilde{\Phi_n} \tag{4.28}$$

where the subscript "n" denotes the 27 nodes involved in the test-grid control volume, and $\mathcal{K}_n$ represents the volumetric weighting factors for each nodes which are listed below:

$$\mathcal{K}_E = \frac{75}{512}\mathcal{R}_E; \quad \mathcal{K}_W = \frac{75}{512}\mathcal{R}_W; \quad \mathcal{K}_N = \frac{75}{512}\mathcal{R}_N;$$

$$\mathcal{K}_S = \frac{75}{512}\mathcal{R}_S; \quad \mathcal{K}_T = \frac{75}{512}\mathcal{R}_T; \quad \mathcal{K}_B = \frac{75}{512}\mathcal{R}_B;$$

$$\mathcal{K}_{NE} = \frac{45}{512}\mathcal{R}_N\mathcal{R}_E; \quad \mathcal{K}_{NW} = \frac{45}{512}\mathcal{R}_N\mathcal{R}_W; \quad \mathcal{K}_{TE} = \frac{45}{512}\mathcal{R}_T\mathcal{R}_E;$$

$$\mathcal{K}_{TW} = \frac{45}{512}\mathcal{R}_T\mathcal{R}_W; \quad \mathcal{K}_{SE} = \frac{45}{512}\mathcal{R}_S\mathcal{R}_E; \quad \mathcal{K}_{SW} = \frac{45}{512}\mathcal{R}_S\mathcal{R}_W;$$

$$\mathcal{K}_{BE} = \frac{45}{512}\mathcal{R}_B\mathcal{R}_E; \quad \mathcal{K}_{BW} = \frac{45}{512}\mathcal{R}_B\mathcal{R}_W; \quad \mathcal{K}_{ST} = \frac{45}{512}\mathcal{R}_S\mathcal{R}_T;$$

$$\mathcal{K}_{SB} = \frac{45}{512}\mathcal{R}_S\mathcal{R}_B; \quad \mathcal{K}_{BN} = \frac{45}{512}\mathcal{R}_B\mathcal{R}_N; \quad \mathcal{K}_{BS} = \frac{45}{512}\mathcal{R}_B\mathcal{R}_S;$$

$$\mathcal{K}_{NET} = \frac{27}{512}\mathcal{R}_N\mathcal{R}_E\mathcal{R}_T; \quad \mathcal{K}_{NEB} = \frac{27}{512}\mathcal{R}_N\mathcal{R}_E\mathcal{R}_B; \quad \mathcal{K}_{SET} = \frac{27}{512}\mathcal{R}_S\mathcal{R}_E\mathcal{R}_T;$$

$$\mathcal{K}_{SEB} = \frac{27}{512}\mathcal{R}_S\mathcal{R}_E\mathcal{R}_B; \quad \mathcal{K}_{NWT} = \frac{27}{512}\mathcal{R}_N\mathcal{R}_W\mathcal{R}_T; \quad \mathcal{K}_{NWB} = \frac{27}{512}\mathcal{R}_N\mathcal{R}_W\mathcal{R}_B;$$

$$\mathcal{K}_{SWT} = \frac{27}{512}\mathcal{R}_S\mathcal{R}_W\mathcal{R}_T; \quad \mathcal{K}_{SWB} = \frac{27}{512}\mathcal{R}_S\mathcal{R}_W\mathcal{R}_B;$$

$$\mathcal{K}_P = \frac{125}{512}$$

where

$$\mathcal{R}_E = \frac{\Delta x_e}{\Delta' x}; \quad \mathcal{R}_W = \frac{\Delta x_w}{\Delta' x}; \quad \mathcal{R}_N = \frac{\Delta y_n}{\Delta' y};$$

$$\mathcal{R}_S = \frac{\Delta y_s}{\Delta' y}; \quad \mathcal{R}_T = \frac{\Delta z_t}{\Delta' z}; \quad \mathcal{R}_B = \frac{\Delta z_b}{\Delta' z};$$

$$\Delta' x = \Delta x_e + \Delta x_w; \quad \Delta' y = \Delta y_n + \Delta y_s; \quad \Delta' z = \Delta z_t + \Delta z_b.$$

4.3.2 Time Average

Time averages are employed instead of the ensemble average of the field quantities in equations (3.28) and (3.29) by assuming that the flow under consideration is stationary. In the solution procedure, we save both instantaneous fields, U_i and Θ, and their time averaged counter-parts, $\overline{U_i}$ and $\overline{\Theta}$. At each time step, the time averaged quantities are updated by the following schemes:

$$\overline{U_i}^1 = f_w \overline{U_i}^0 + (1 - f_w) U_i^1$$

$$\overline{\Theta}^1 = f_w \overline{\Theta}^0 + (1 - f_w) \Theta^1$$

where f_w is a weighting factor less than unity. The characteristic time scale of the time average is defined as:

$$T = \frac{\Delta t}{1 - f_w}.$$

4.3.3 Solution Method for $\bar{B}_j$

Equation (3.36) is solved for $\bar{B}_j$ using the following iteration scheme:

$$\bar{B}_j^{(n)} = (1 - r)\bar{B}_j^{(o)} + 2r(2 - \bar{m}_j) / \ln\{[\frac{2(\frac{2}{\bar{B}_j})^2 + 2(\frac{2}{\bar{B}_j}) + 1}{2(\frac{\bar{m}_j}{\bar{B}_j})^2 + 2(\frac{\bar{m}_j}{\bar{B}_j}) + 1}](\frac{1}{R_i})\}$$

$$R_i = \frac{t_{ii} - T_{ii}}{t_{ii}} + (\frac{T_{ii}}{t_{ii}})[\frac{2(\frac{\bar{\Gamma}_j}{\bar{B}_j})^2 + 2(\frac{\bar{\Gamma}_j}{\bar{B}_j}) + 1}{2(\frac{\bar{m}_j}{\bar{B}_j})^2 + 2(\frac{\bar{m}_j}{\bar{B}_j}) + 1}] \exp[-2\frac{(\bar{\Gamma}_j - \bar{m}_j)}{\bar{B}_j}]$$

where the superscripts "(o)" and "(n)" denote, respectively, the old and new values, and r is the relaxation factor. Note that if $t_{ii} = 0$ or $t_{ii} - T_{ii} = 0$, no value of $\bar{B}_j$ can be obtained.

4.3.4 Flow Unsteadiness and Numerical Instability

As was pointed out in section 1.2, flow unsteadiness is an important feature of turbulence, therefore its large scale portion should be captured in the LES. On the other hand, flow unsteadiness often causes numerical instability and consequently disrupts the simulation procedure. We are facing a challenge of simulating a physical procedure which may be locally unstable with a numerical method which is absolutely intolerable to instability. A careful comparison between a physical and a numerical realization of fluid motion shows that the latter has a significantly longer response time to a sudden local change of flow fields; it needs at least several time-steps (iterations) to adjust the flow fields to follow the change which has happened. If other sudden local changes occur during the above "adjustment" time period, the numerical method may fail to handle them and leads to numerical divergence.

Many previous researchers of the LES method use the positive SGS eddy diffusivity to alleviate the problem of numerical instability described above (see section 1.2). The positive SGS eddy diffusivity smears out acute local changes of the flow fields and thus stablizes the simulation procedure. However, this approach is not favoured by the author, because it may considerably distort the unsteadiness feature of the flow under consideration. In the present study, a special "clipping" algorithm was designed to prevent the magnitude of the sum of a resolvable field and the RMS of its corresponding SGS fluctuation from exceeding a specifically pre-determined value. We describe in detail this special "clipping" algorithm in the following paragraph.

First of all, the "clipping" acts on the SGS Reynolds stress τ_{ij} and the SGS turbulent heat flux σ_j only. After the values of τ_{ij} and σ_j are calculated (denoted by "*"),

they are revised by multiplying them by the coefficients R_v and $R_t{}^j$ as follows:

$$\tau_{ij} = R_v \tau_{ij}^*$$

$$\sigma_j = R_t{}^j \sqrt{R_v} \sigma_j^*$$

where R_v and $R_t{}^j$ are calculated by

$$R_v = \begin{cases} 0 & V_{max}^2 - \tilde{V}_{total}^2 \leq 0 \\ \frac{V_{max}^2 - \tilde{V}_{total}^2}{v_{rms}^2} & v_{rms}^2 > V_{max}^2 - \tilde{V}_{total}^2 > 0 \\ 1 & \text{otherwise} \end{cases} \tag{4.29}$$

and

$$R_t{}^j = \begin{cases} 0 & \Theta_{max} \leq \tilde{\Theta} \text{ or } \Theta_{min} \geq \tilde{\Theta} \\ \frac{\min(\Theta_{max} - \tilde{\Theta}, \tilde{\Theta} - \Theta_{min})}{\theta_{rms}} & \Theta_{max} > \tilde{\Theta} > \Theta_{min},\ \theta_{rms} > \min(\Theta_{max} - \tilde{\Theta}, \tilde{\Theta} - \Theta_{min}) \\ 1 & \text{otherwise} \end{cases} \tag{4.30}$$

In equations 4.29 and 4.30, $\tilde{V}_{total}$ is the magnitude of the resolvable velocity; v_{rms} is the RMS of the SGS velocity fluctuation, *i.e.*

$$v_{rms}^2 = -\tau_{11} - \tau_{22} - \tau_{33},$$

and θ_{rms} is the RMS of the SGS temperature fluctuation. All of these values are calculable in the simulation. On the other hand, V_{max}, the magnitude of the maximum possible instantaneous velocity, Θ_{max} , the magnitude of the maximum possible temperature, and Θ_{min} , the magnitude of the minimum possible temperature should be specified based on flow configurations. For example, in LDC flows, $V_{max} = U_0$

(the driving velocity), while in BDC flows $V_{max} = U_b/2$ (half of the buoyant velocity scale), $\Theta_{max} = \Theta_{hot}$ (the hot wall temperature), and $\Theta_{min} = \Theta_{cold}$ (the cold wall temperature).

4.4 Boundary Conditions

In the grid configuration for the present study, the boundaries of the flow domain are all coincident with the surfaces of control volumes, and no node points are placed on the boundaries. Thus, boundary conditions are specified by setting values of field quantities at two fictitious nodes located outside of the domain near boundaries (see Figure 4.3). Note that using two fictitious nodes is a requirement of the QUICK scheme. In the present study, the locations of the two fictitious nodes are selected so that: 1) the boundary is located midway between the first fictitious node and the first interior node; 2) the first fictitious node is located midway between the the second fictitious node and the first interior node. In LES practice, there are generally three kinds of boundaries, *i.e.* solid walls, inflow boundaries, and outflow boundaries. The so called homogeneous (or zero-gradient) boundary condition is also applied when one simulates flows with symmetry or two-dimensional flows. Numerical implementation of the boundary conditions of different kinds are discussed below.

4.4.1 Solid Walls

On solid walls, the no penetration and no-slip condition is always assumed, so that no convective transport exists through solid wall boundaries. Thus, field values for the second fictitious nodes are not used. Velocities at the first fictitious nodes are simply set as

$$U_i^{(-1)} = 2U_i^{(b)} - U_i^{(1)} \quad .$$

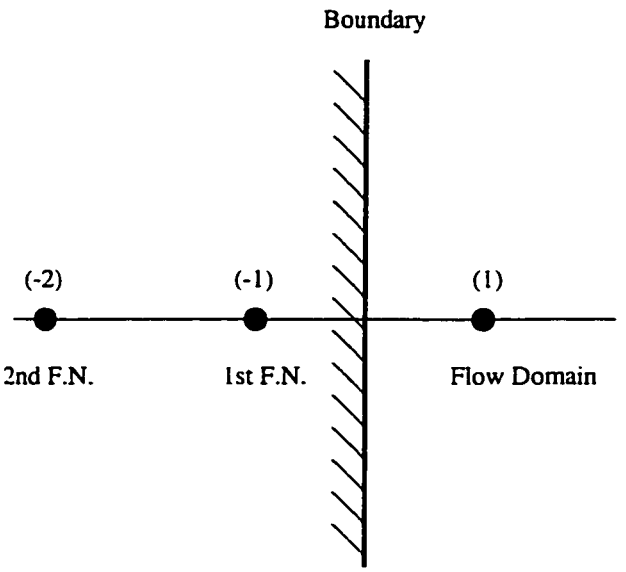

Figure 4.3: Fictitious nodes for boundary condition specification

Temperature boundary conditions for solid walls can be classified as: 1) fixed wall temperature; or 2) fixed normal wall heat flux. The corresponding setting of the temperatures at the first fictitious nodes are, respectively,

$$\Theta^{(-1)} = 2\Theta^{(b)} - \Theta^{(1)}$$

and

$$\Theta^{(-1)} = \Theta^{(1)} + \frac{\Delta x_i^{(b)} q'^{(b)}}{k}$$

where $\Theta^{(b)}$ and $q'^{(b)}$ are, respectively, the temperature and in-flow heat flux on the solid wall; k is the thermal conductivity of the fluid; $\Delta x_i^{(b)}$ is the distance between the first fictitious node and its interior neighbour.

When the collocated scheme is employed, no boundary condition is required for pressure on solid walls, because flux velocities on the wall are exactly zero. Since values of τ_{ij}, σ_j, α_j, on solid wall boundaries are all zero (no turbulence), we can set

their values at the first fictitious nodes as

$$\tau_{ij}^{(-1)} = -\tau_{ij}^{(1)}; \quad \sigma_j^{(-1)} = -\sigma_j^{(1)}; \quad \alpha_j^{(-1)} = -\alpha_j^{(1)}$$

4.4.2 Homogeneous Boundaries

A homogeneous boundary is not a real boundary of a flow domain, but an imaginary bounding plane representing the plane of symmetry for a symmetrical flow, or the transverse boundary for a 2-D flow. The equations for the field values at the fictitious nodes for the homogeneous boundaries are

$$\Phi^{(-1)} = \Phi^{(-2)} = \Phi^{(1)} \tag{4.31}$$

where Φ represents any field quantity.

We allow non-zero fluxes across homogeneous boundaries which can be applied in the Poisson equation for the pressure correction fields. Of course, the pressure field values and coefficients a_P at the first fictitious nodes are set as

$$P^{(-1)} = P^{(1)} \tag{4.32}$$

$$a_P{}^{(-1)} = a_P{}^{(1)}. \tag{4.33}$$

When a homogeneous boundary condition is applied to a field quantity Φ on a boundary, we say that Φ is open on the boundary. Otherwise, when a specific value is set for Φ on a boundary, we say that Φ is closed.

4.4.3 Inflow and Outflow Boundaries

In dealing with inflow and outflow boundaries, one should avoid over-specifying the boundary conditions. For example, if pressure values on inflow or outflow boundaries are closed, velocity boundary conditions there should be opened, because velocity values on inflow and outflow boundaries are solely determined by the pressure values there, and vice versa. Since pressure values on inflow and outflow boundaries are difficult to measure experimentally, most people prefer using closed velocity boundary conditions, but open pressure boundary conditions on inflow or out flow boundaries. Furthermore, if all pressure boundary conditions on inflow and outflow boundaries are opened, we still can not use closed velocity boundary conditions over the entire boundary, because we have the problem of over-specifying the problem. To avoid over-specifying, one can arbitrarily select at least one point on the inflow or outflow boundaries, and open the velocity boundary condition there. In practice, we can use open velocity boundary conditions at more than one point on the inflow and out flow boundaries in the case that closed boundary conditions are not available. However, generally the more numerous the open velocity boundary conditions applied, the poorer the accuracy of the final simulation result.

In the present study, we avoid using closed pressure boundary conditions on inflow and outflow boundaries, because pressure fields are far more difficult to measure than velocity fields in practice. If the velocity boundary conditions on inflow and outflow boundaries are opened, equation (4.31) is used to specify field quantity values at fictitious nodes. Otherwise, the following expression is applied:

$$\Phi^{(-1)} = \Phi^{(-2)} = \Phi^{(b)} \tag{4.34}$$

Note that we actually set boundary values at the ficticious nodes instead of exactly on the inlet or outlet boundaries. The homogeneous pressure boundary condition setting expressed in equations (4.32) and (4.33) is still employed. Most people prefer to close

inflow boundary conditions, but to open outflow boundary conditions, which assumes that the flow in the domain is mainly affected by inflow boundaries. However, we try to treat inflow and outflow boundaries equally in problems of low speed flow, because in some cases the effect of outflow boundaries may be dominant.

In the case of turbulent inflow or outflow, $\Phi^{(b)}$ are time-dependent quantities, so that inflow or outflow boundary conditions are always changing during the simulation procedure. Thus, $\Phi^{(b)}$ should be updated in each time step. We approximate $\Phi^{(b)}$ by the following function,

$$\Phi^{(b)} = \overline{\Phi^{(b)}} + \phi^{(b)} \sin(\vartheta_0 + 2\pi f \Delta t)$$

where $\overline{\Phi^{(b)}}$ is the time mean of $\Phi^{(b)}$; $\phi^{(b)}$ is the amplitude of the turbulent fluctuation of $\Phi^{(b)}$; ϑ_0 is the initial phase for a sine function; f is the dominant frequency of the turbulent fluctuation. The initial phase ϑ_0 is produced randomly prior to simulation, updated in each time step using the following formula, and saved for calculation of $\Phi^{(b)}$ in the next time step.

$$\vartheta_0^{(1)} = mod[\vartheta_0^{(0)} + 2\pi f \Delta t,\ 2\pi].$$

4.5 LES-3DROOM Code

Using the numerical techniques described above, the VAT for turbulent flow simulation was coded using FORTRAN 77 under the title "LES-3DROOM". LES-3DROOM consists of three codes which are, respectively, LES-PREPR, LES-MAIN, and LES-POSTPR. The functions of these codes are shown in Table 4.1.

The mainline, LES-MAIN, calls directly five subroutines *i.e.*: LES-SGS, LES-

FALSE, LES-SOLVER, LES-CPR, and LES-LOCAL. The objectives of these subroutines are shown in Table 4.2. A flow chart to show main procedures in the LES-MAIN is given in Figure 4.4. A flow chater for each subroutine is shown in Appendix B.

Table 4.1: Functions of three codes in LES-3DROOM

Code	Functions
LES-PREPR	Pre-processing *i.e.* specifying solution domain, grid and initial condition
LES-MAIN	Main body of LES-3DROOM
LES-POSTPR	Post-processing *i.e.* output fields for the software package FIELDVIEW

Table 4.2: Objectives of five subroutines called by LES-MAIN

Subroutine	Objectives
LES-LOCAL	Solving the momentum equation, update pressure and velocity fields at each each node point
LES-SGS	Calculating the SGS Reynolds stress, turbulent heat flux, and eddy diffusivities at each node point
LES-FALSE	Setting field values at each fictitious node
LES-CPR	Calculating surface flux velocities for each control volume and coefficients for the pressure correction equation
LES-SOLVER	Solving the 3-D linear equations for the pressure correction field and the temperature fields

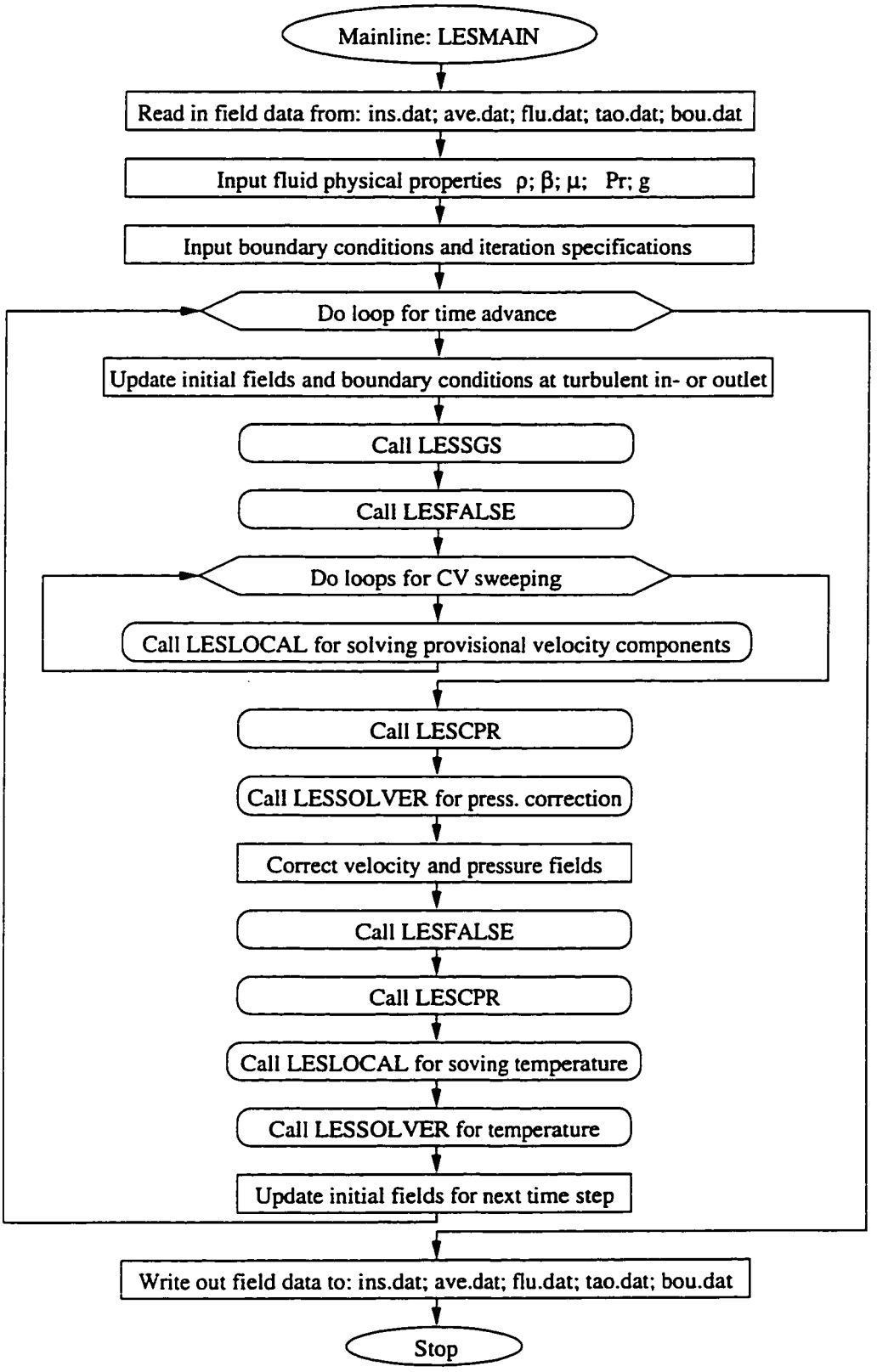

Figure 4.4: Flow chart for the code LES-MAIN

4.6 Summary

In this chapter, we discussed the numerical method developed for the VAT. In addition, the computer code designed for realization of the technique was briefly described. Although the fractional-step scheme, SIMPLE, QUICK, and PRIME schemes on which the numerical method in the present study is based are well known in the CFD community, the combination of these schemes with collocated storage of the resolved fields represents a novel solution strategy. Furthermore, the numerical method is implemented in a code specifically designed for (but not limited to) the LES using the FSS SGS model.

In the next chapter, we present the benchmark test results of this newly developed numerical method in the context of high Reynolds and Rayleigh number laminar flows.

Chapter 5

Benchmark Tests for Numerical Schemes

5.1 Introduction

In this chapter, we show the performance of the proposed numerical schemes, especially the collocated scheme, by applying them to simulations of laminar flows without using the SGS model. These laminar flows have been extensively investigated experimentally or numerically, and broadly accepted benchmark results for the flows are available. Comparison of the present simulation results to the corresponding benchmark ones provide us information for estimating the validity of the schemes applied.

The laminar flows to be simulated are: 1) 2-D lid-driven cavity flow; 2) 3-D lid-driven cavity flow; 2) 3-D buoyancy-driven cavity flow. From a numerical viewpoint,

2- and 3-D flows in cavities serve as ideal prototype problems for testing numerical schemes. Geometric simplicity and well defined flow structures make these flows especially attractive as benchmarks for new numerical techniques, including new differencing schemes and problem formulations. In addition, they represent typical flow patterns in an air-conditioned room.

Since the high Reynolds number performance of the schemes is critical for turbulent flow simulation, the Reynolds number for the 2-D lid-driven cavity flow is selected to be relatively high ($Re = 1000$). The Reynolds or Rayleigh numbers selected for the 3-D simulations are lower ($Re = 400$, $Ra = 10^6$) to limit the computational effort required. Of course, in order to remove the effect of the SGS modelling, the Reynolds and Rayleigh numbers of the flows are selected to ensure that the simulated flows are absolutely in the laminar regime. The simulations were all performed on a SUN SPARCstation 5 of the CFD group at the University of Saskatchewan. The normalized mass and pressure correction equation residuals and related CPU times for all the simulations are presented in Table 5.1.

Table 5.1: Residuals and CPU times of each simulation

Flow	Computer(Dou. Pre.)	CPU (hr.)	R_m	R_p
2-D LDC $Re = 1000$	SUN SPARC-5	50	6.9×10^{-11}	9.4×10^{-14}
3-D LDC $Re = 400$	SUN SPARC-5	25	5.3×10^{-11}	6.7×10^{-14}
3-D BDC $Re = 10^6$	SUN SPARC-5	40	3.0×10^{-10}	8.1×10^{-14}

5.2 2-D Lid-Driven Cavity Flows, $Re = 1000$

The 2-D lid-driven cavity flow and coordinate system on which the flow domain is defined are shown schematically in Figure 5.1. The solution domain is a square cavity with a top lid moving at a velocity U_0. L denotes the length scale of the cavity. No-slip and impermeable boundary conditions are applied to all solid walls. The flow is

characterised by the Reynolds number defined as $Re = \frac{U_0 L}{\nu}$ which was selected in the simulation to be 1000.

The 2-D flow was simulated using our 3-D code "LES-3DROOM" with a $61 \times 3 \times 61$ grid. Note that in order to achieve a 2-D configuration with a 3-D code, only three control volumes are applied along the diminished y-direction, and homogeneous boundary conditions applied on the two side walls.

The final results of the simulation are shown in Figure 5.2 for streamlines, and in Figures 5.3 and 5.4 for centerline velocity profiles. The peak values in the centerline velocity profiles obtained in the present simulation are compared with those from the previous simulations of the same flow in Table 5.2. Although less than a quarter of the total number of grid points were applied, the results of the present simulation are more accurate than those obtained by Chen *et al.* (1984), Bruneau *et al.* (1990), Ghia *et al.* (1982), and Deng *et al.* (1994). Therefore, the advantage of the present code is apparent.

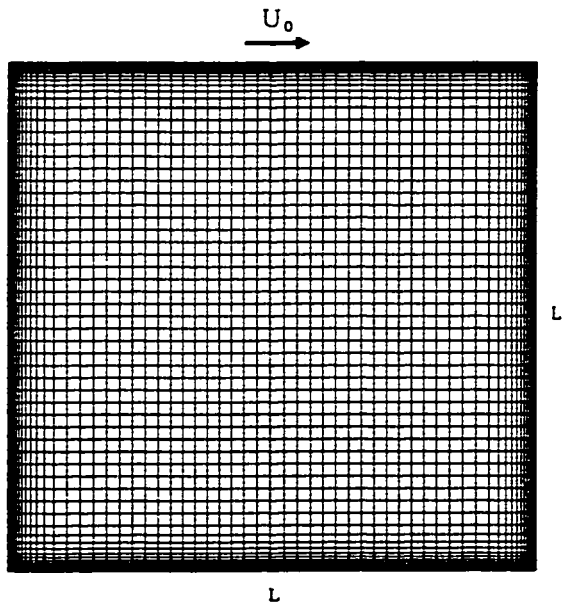

Figure 5.1: Grid and configuration for 2-D lid-driven flow in a square cavity

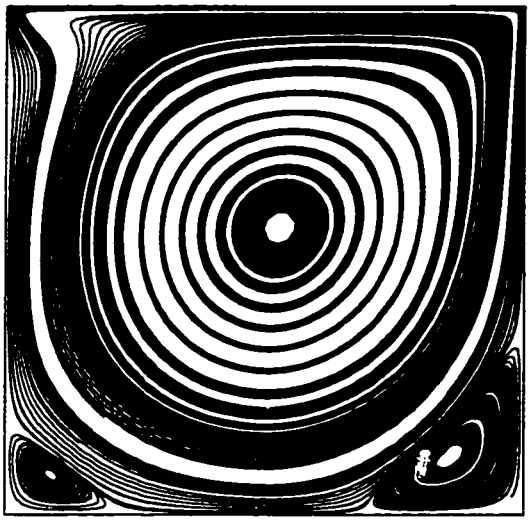

Figure 5.2: Streamlines of 2-D LDC flow at $Re = 1000$

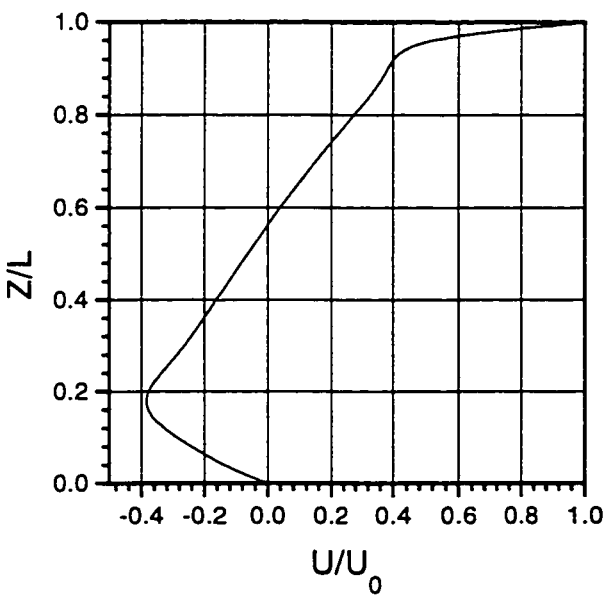

Figure 5.3: U-velocity profile of 2-D LDC flow at $Re = 1000$ along $X/L = 0.5$

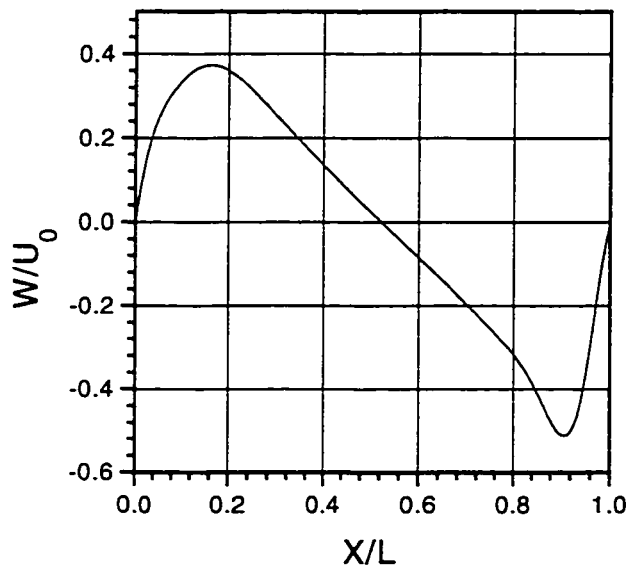

Figure 5.4: W-velocity profile of 2-D LDC flow at $Re = 1000$ along $Z/L = 0.5$

Table 5.2: Characteristic values for 2-D LDC flow at $Re = 1000$

Method	Grid	U_{min}	W_{min}	W_{max}
Present	61×61	-0.3854	-0.5256	0.3753
Deng *et al.* (1994)	128×128	-0.38511	-0.52280	0.37369
Ghia *et al.* (1982)	129×129	-0.38289	-0.51550	0.37095
Bruneau *et al.* (1990)	256×256	-0.3764	-0.5208	0.3665
Chen *et al.* (1984)	128×128	-0.3689	-0.5037	0.3553
Estimate exact (by Deng *et al.*)	–	-0.38867	-0.52724	0.37702

5.3 3-D Lid-Driven Cavity Flow, $Re = 400$

In order to test the ability of the code "LES-3DROOM" to capture 3-D features of flows, a 3-D lid-driven flow and a 3-D buoyancy-driven flow in a cubic cavity were selected as the targets of the second and third benchmark simulations. Both simulations employed the same non-uniform grid with 31 × 31 × 31 control volumes over a 1 m × 1 m × 1 m cubic solution domain (see Figure 5.5).

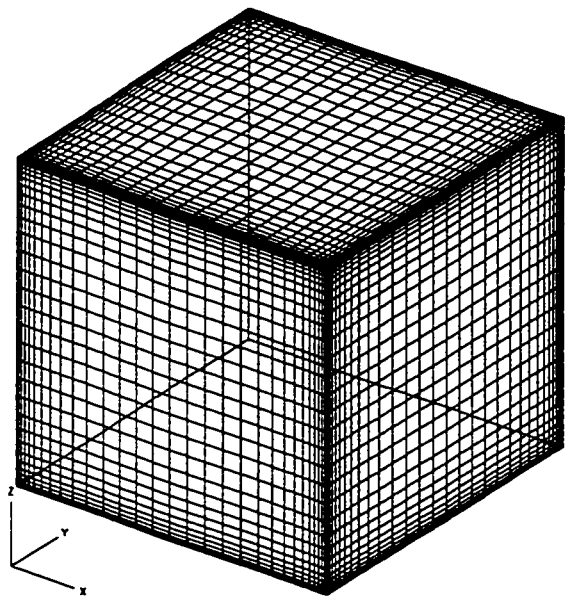

Figure 5.5: Grid for 3-D lid-driven and buoyancy-driven flows in a cubic cavity

We consider the 3-D lid-driven cubic cavity flow in this section, which is shown schematically in Figure 5.6. As in the 2-D case, the top lid moves horizontally with a speed U_0. The no-slip and no-penetration boundary conditions are applied to all the walls. Due to the effect of side walls, strong secondary vortices exist in the flow. The 3-D lid-driven cubic cavity flow has been investigated numerically by Ku *et al.* (1987) using the pseudo-spectral method, Deng *et al.* (1994) using the CPI schemes, and Babu & Korpela (1994) using Abdalah's (1987) non-staggered scheme.

Ku *et al.*'s (1987) results have been generally viewed as the benchmark, because the pseudo-spectral method has the reputation of being more accurate than the finite difference schemes. The simulations by Ku *et al.* (1987) and by Babu & Korpela (1994) were carried out in half of the flow domain using, respectively, $25 \times 13 \times 25$ modes and a grid of $63 \times 33 \times 63$ control volumes, while Deng *et al.*'s (1994) simulation was performed in whole flow domain using a grid of $64 \times 64 \times 64$ control volumes. Therefore, the present simulation employed a significantly coarser grid which has less than one eighth of the control volumes employed by Deng *et al.* (1994) or of those employed by Babu & Korpela (1994).

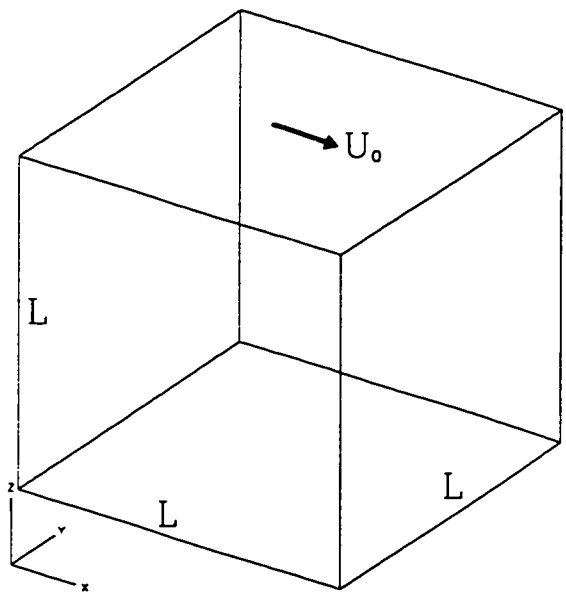

Figure 5.6: Configuration for 3-D lid-driven flow in a cubic cavity

The final results of the present simulation are exhibited as follows. Primary and secondary patterns of the flow are shown in terms of vector plots in Figures 5.7 through 5.9. Note that in order to show fine strucure of the secondary flow patterns, vector length in Figures 5.8 and 5.9 are enlarged by a ratio of 2. All the vector plots are similar to those predicted by Ku *et al.* (1987) and Babu & Korpela (1994). The locations of the primary and secondary vortices closely match those of Ku *et al.*

(1987). The longitudinal and vertical velocity component profiles along the vertical and horizontal centerlines are shown in Figures 5.10 and 5.11. The characteristic velocities (peak values) in the profiles are compared with those from the previous simulations of the same flow in Table 5.3. If Ku *et al.*'s (1987) results are viewed as the benchmark, Table 5.3 shows that the present results are as good as Deng *et al.*'s (1994) and far better than Babu & Korpela's (1994) results.

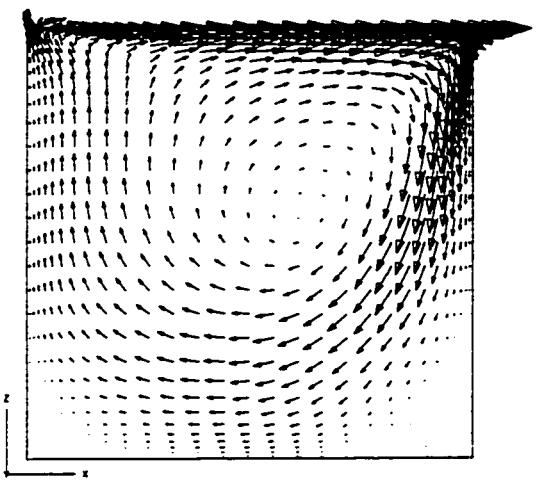

Figure 5.7: Vector plot (U,W) for 3-D LDC flow at $Y/L = 0.5$

Table 5.3: Characteristic values for 3-D LDC flow at $Re = 400$

Method	Grid/Modes	U_{min}	W_{min}	W_{max}
Present	31×31×31	-0.2321	-0.3798	0.2048
Deng *et al.* (1994)	64×64×64	-0.2330	-0.3765	0.2046
Babu *et al.* (1994)	63×33×63	-0.2083	-0.3087	0.1773
Ku *et al.* (1987)	25×13×25 Modes	-0.2378	-0.3791	0.2053

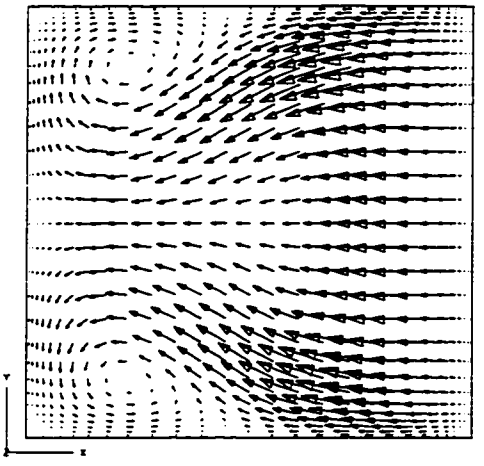

Figure 5.8: Vector plot (U,V) for 3-D LDC flow at $Z/L = 0.5$

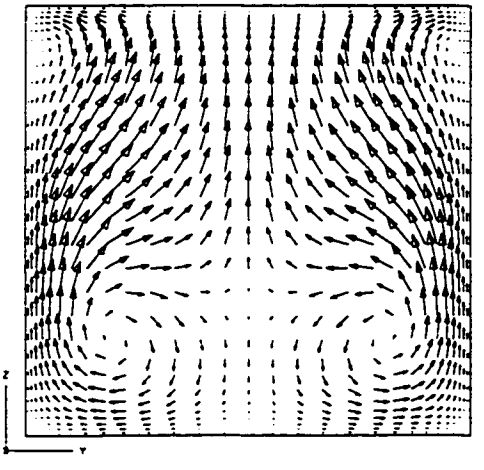

Figure 5.9: Vector plot (V,W) for 3-D LDC flow at $X/L = 0.5$

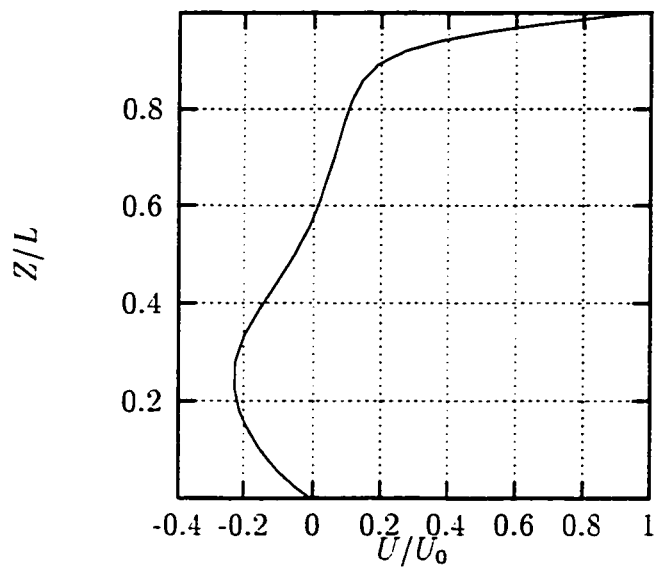

Figure 5.10: Profile of U/U_0 of 3-D LDC flow along vertical mid-line

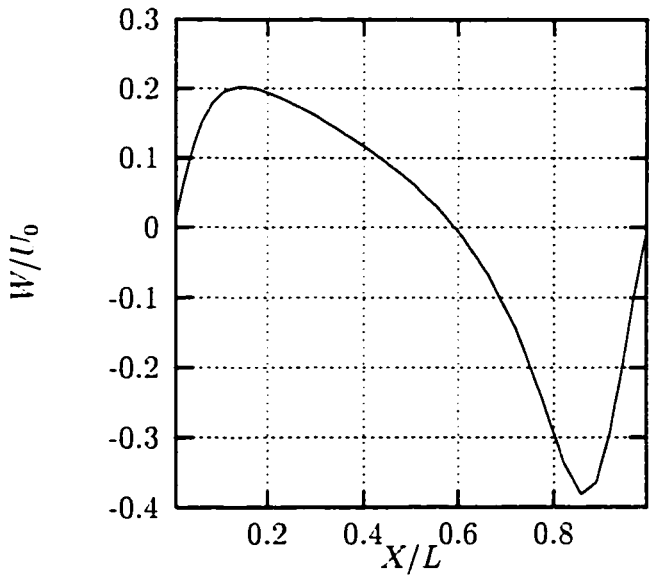

Figure 5.11: Profile of W/U_0 of 3-D LDC flow along horizontal mid-line

5.4 3-D Buoyancy-Driven Cavity Flow, $Ra = 10^6$

The configuration of the 3-D buoyancy-driven cavity flow is shown in Figure 5.12. The solution domain is identical to that of the 3-D lid-driven cavity flow, while the flow is driven by the buoyancy force initiated by the temperature difference $\Delta\Theta$ between two opposite walls at $x = 0$ and $x = L$. The flow is characterised by the Rayleigh number defined as

$$Ra = \frac{gL^3\beta\Delta\Theta}{\nu\alpha} \tag{5.1}$$

which was selected to be 10^6 in the simulation.

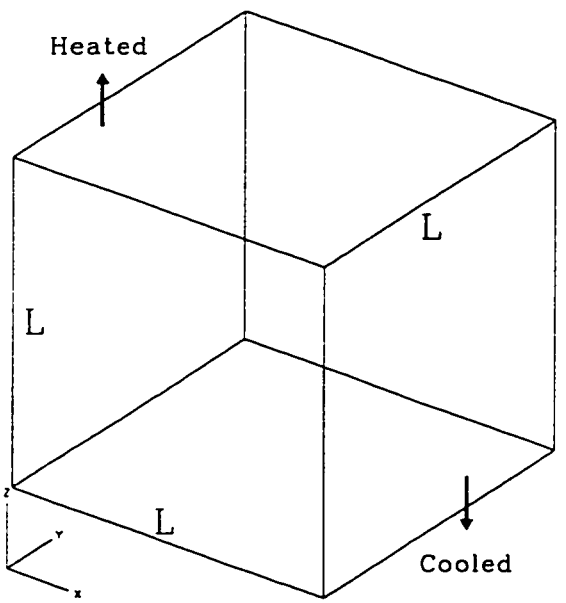

Figure 5.12: Configuration for 3-D buoyancy-driven flow in a cubic cavity

Previous investigations of the 3-D buoyancy-driven cubic cavity flow have been performed numerically by Lankhorst & Hoogendoorn (1988) using a grid of 45 × 20 × 45 control volumes (half of flow domain) and by Fusegi *et al.* (1991) using a grid of 62 × 62 × 62 control volumes. Previous experimental investigations have only focused on high aspect ratio (≥ 5) cavities to justify the 2-D approximation, such as

that performed by Bilski *et al.* (1986) who acquired both velocity and temperature distributions along horizontal and vertical centerlines of a cavity of aspect ratio 5 at $Ra = 1.03 \times 10^5$ and $Ra = 1.13 \times 10^6$. The benchmarks selected for the present simulation are the numerical results of Fusegi *et al.* (1991) and the experimental results by Bilski *et al.* (1986).

Firstly, primary and secondary patterns of the flow are shown in terms of vector plots in Figures 5.13 through 5.15. In order to show the fine strucure of the secondary flow patterns, vector length in Figures 5.14 and 5.15 are enlarged by a ratio of 3. The temperature field of the flow is shown in terms of isothermal lines and surfaces in Figures 5.16 and 5.17, respectively. It is noted that the 3-D buoyancy-driven cubic cavity flow at $Ra = 10^6$ is more two-dimensional than the 3-D lid-driven cubic cavity flow at $Re = 400$; it has weaker secondary flows (see Figures 5.15 and 5.14) and an almost uniform distribution of temperature along transverse y-direction (see Figure 5.17). This feature of the flow was also exhibited by the simulation results of Fusegi *et al.* (1991).

The quantitative results of the simulation are shown in Figures 5.18 through 5.21. The obtained profiles of U and W velocity components along, respectively, vertical and horizontal centerlines of the cavity are compared with their counterparts from the simulation of Fusegi *et al.* (1991) and from the experiment of Bilski *et al.* (1986). It is again noted that, although a coarser grid is employed, the present simulation results are as good as Fusegi *et al.*'s (1991) results. The significant difference in the profiles of the U velocity component along the vertical centerlines between the results of both simulations and the experiment is probably due to the effect of side walls (see Figure 5.18). The experimental data were from a cavity with aspect ratio of 5, whereas the aspect ratio of the cavities for both simulations is 1.

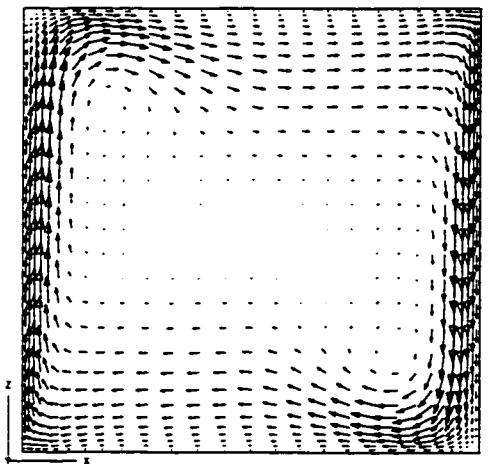

Figure 5.13: Vector plot (U,W) for 3-D BDC flow at $Y/L = 0.5$

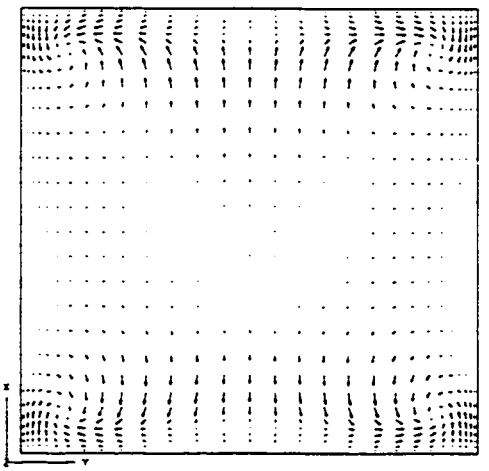

Figure 5.14: Vector plot (U,V) for 3-D BDC flow at $Z/L = 0.5$

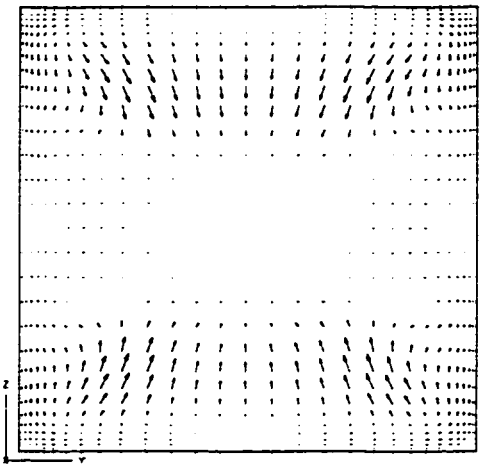

Figure 5.15: Vector plot (V,W) for 3-D BDC flow at $X/L = 0.5$

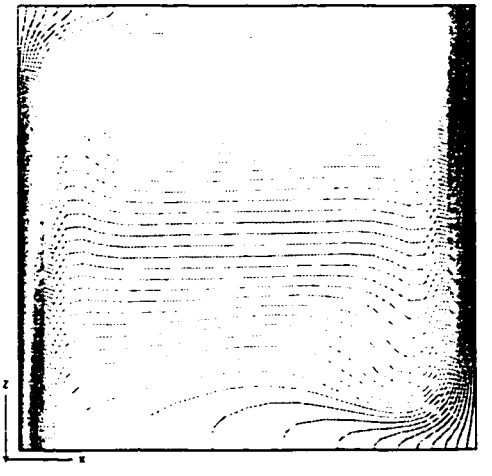

Figure 5.16: Isothermal lines for 3-D BDC flow at $Y/L = 0.5$

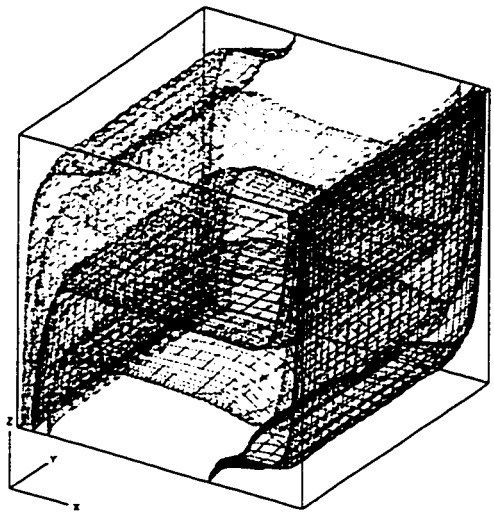

Figure 5.17: Isothermal surfaces of 3-D BDC flow

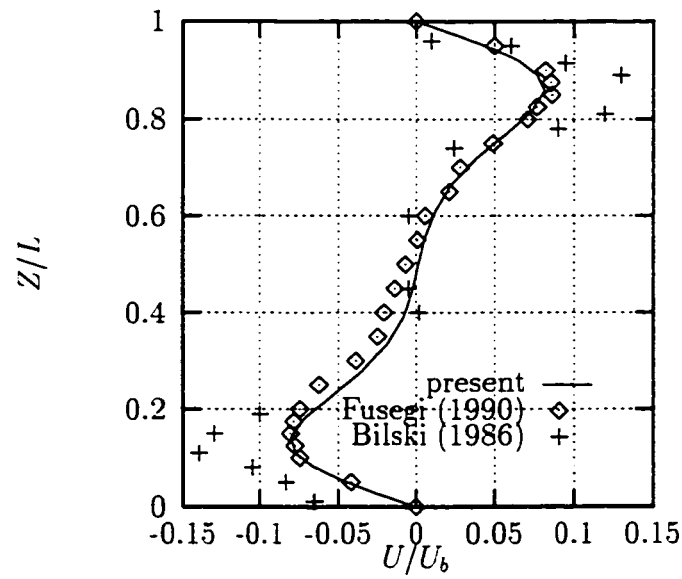

Figure 5.18: Profile of U/U_b of 3-D BDC flow along vertical mid-line

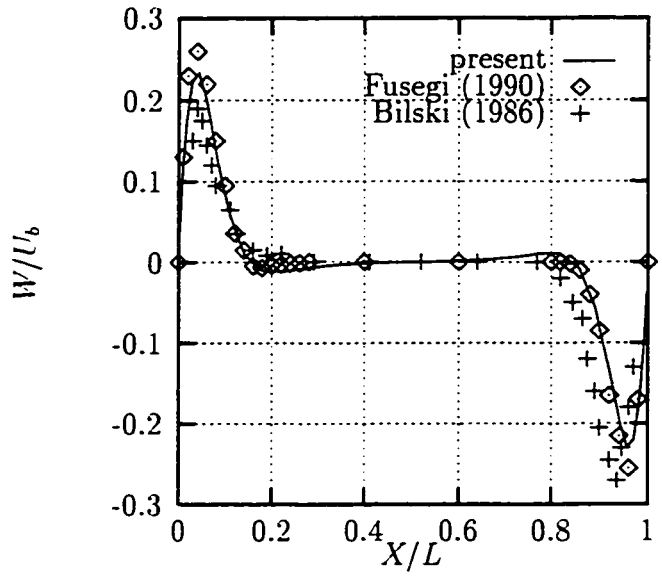

Figure 5.19: Profile of W/U_b of 3-D BDC flow along horizontal mid-line

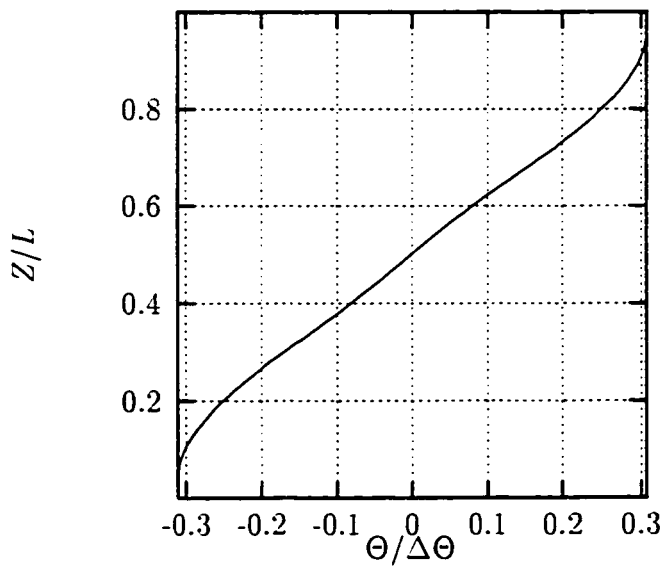

Figure 5.20: Profile of $\Theta/\Delta\Theta$ of 3-D BDC flow along vertical mid-line

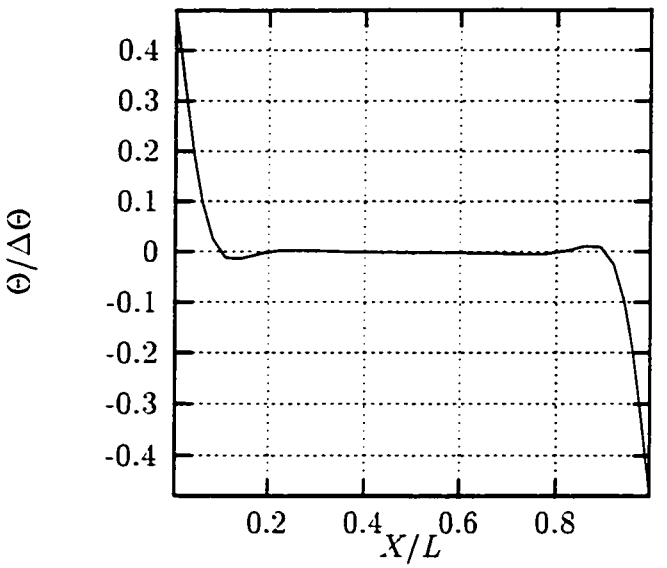

Figure 5.21: Profile of $\Theta/\Delta\Theta$ of 3-D BDC flow along horizontal mid-line

5.5 Summary

Benchmark tests of the numerical schemes, particularly the collocated scheme, developed in Chapter 4 have been performed on three specifically selected laminar flows. All of the results obtained show that the scheme performs well for highly convective and 3-D flow simulation. Additionally, compared with some other schemes developed for solving viscous incompressible fluid motion, the collocated scheme can obtain at least the same level of simulation accuracy using approximately only one-half of the regular number of cells per dimension.

The results of benchmark tests of the SGS model in the VAT are presented in the next chapter. Since the flows considered there are turbulent, they are definitely more convection-dominant than the flows considered in the present chapter. Success in the simulation of turbulent flow will not only validate the SGS model applied, but also confirm the performance of the numerical schemes identified above.

Chapter 6

Benchmark Tests for SGS Model

6.1 Introduction

In this chapter, we discuss the benchmark test results to demonstrate the performance of the VAT for turbulent flow simulation. To this end, we choose two different turbulent flows as benchmarks: 1) a lid-driven turbulent flow in a 3-D cavity at $Re = 10^4$; 2) a buoyancy-driven turbulent flow in a 3-D cavity at $Ra = 10^{10}$. The reason for this choice is two-fold. Firstly, both flows have been studied using experimental and/or numerical techniques and limited results for them are available. Secondly, the flows can be viewed as building blocks of room airflow which are considered in Chapter 7. These flows were simulated with the VAT, and the results obtained are compared with the corresponding benchmark data.

In order to capture turbulent fluctuations, fine non-uniform grids were employed in simulations of both the lid-driven and buoyancy-driven turbulent flows. The physical

properties of the fluid in both simulations are selected as: dynamic viscosity $\mu = 1.983 \times 10^{-6}$ (kg/ms); density $\rho = 1.1774$ (kg/m^3); coefficient of volumetric thermal expansion $\beta = 0.00333$ (K^{-1}); and Prandtl number $Pr = 0.76$.

In order to save CPU time, both simulations started from zero 2-D initial fields, and were first simulated two dimensionally using a time step increment of Δt ($\Delta t = 0.1$ (sec) for the LDC flow and $\Delta t = 0.01$ (sec) for the BDC flow) until steady states had been reached. This procedure took approximately 8,000 time steps. Then, the 2-D data fields obtained were applied as the initial conditions for 3-D simulations, which were pushed forward three dimensionally for another 2,000 time steps (using $\Delta t = 0.05$ (sec) for the LDC flow and $\Delta t = 0.005$ (sec) for the BDC flow). The weighting factor f_w for time averaging was selected to be 0.5 at the beginning of the 2-D simulations, and then was increased in three steps to 0.9995 when steady states had been reached. After switching to 3-D simulations, f_w was reduced to 0.5 for the first 200 time steps (the dynamic length scale range is still calculated based on $f_w = 0.9995$) and then increased to 0.9995. The 3-D simulation took approximately 300 CPU hours for the LDC flow and 450 CPU hours for the buoyancy-driven cavity flow on the SUN SPARCstation 5. In the following two sections, the results of the two simulations are presented and discussed in detail.

6.2 3-D Lid-Driven Cavity Flow, $Re = 10^4$

6.2.1 Flow Configuration

The solution domain of the 3-D lid-driven turbulent cavity flow is a cuboid box of size $L_x \times L_y \times L_z$, as shown in Figure 6.1. We chose $L_x = L_z = 1\ m$ and $L_y = 0.5\ m$ in the simulation. All boundaries of the domain are solid walls at rest except the top lid which moves horizontally at a speed U_0. We selected $U_0 = 0.01684\ m/s$ to ensure

the Reynolds number based on the driving speed U_0 and the length scale L_x or L_z to be 10^4.

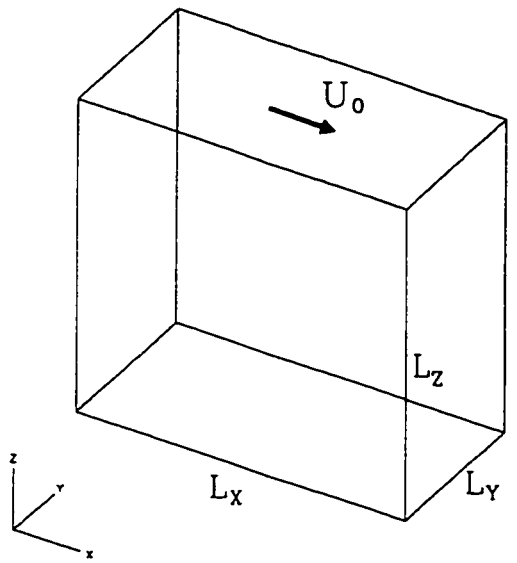

Figure 6.1: Solution domain of 3-D lid-driven turbulent cavity flow

The grid applied for the 3-D lid-driven turbulent cavity flow simulation involves $51 \times 21 \times 51$ control volumes, which is shown in Figure 6.2. The grid is refined near the walls. The maximum aspect ratio of the control volumes is 18:1 which occurs close to the centres of the top, bottom, upstream, and downstream walls.

Some previous investigations of turbulent 3-D lid-drive cavity flows, both numerical and experimental, have been reported. For example, numerical investigations of the flow were performed using the LES method with the Smagorinsky SGS model by Jordan & Ragab (1994), which showed that the transition of the flow from laminar to turbulence occurs at $Re \sim 5000$, and it is definitely turbulent at $Re = 10^4$. Flows of different aspect ratio and Reynolds number (up to 10^4) were investigated experimentally by Prasad & Koseff (1989), and numerically using the LES method with the dynamic and mixed SGS models by Zang *et al.* (1993a) and Zang *et al.*

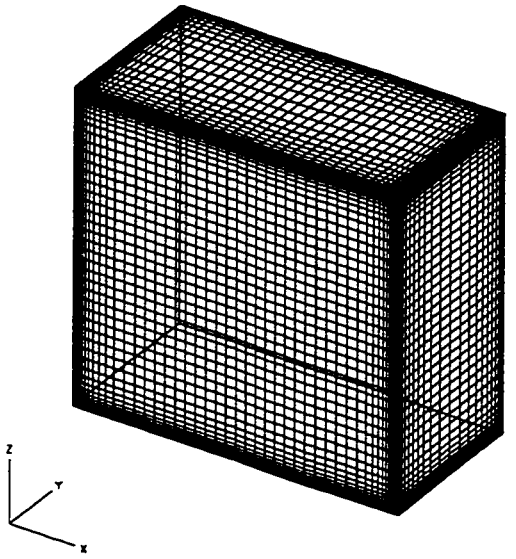

Figure 6.2: Grid for solution of 3-D turbulent LDC flow

(1993b) at Stanford University. The experimental results of Prasad & Koseff (1989) are considered as a benchmark for the present simulation.

6.2.2 Results and Discussion

First of all, the patterns of the time-averaged resolvable flow fields are displayed in terms of vector plots in Figures 6.3 through 6.5. Since no such vector plots pertaining to previous experimental or numerical investigation of this turbulent LDC flow are found in the literature, no benchmark comparison can be made. However, we still can give some general comments on them. Figure 6.3 shows the primary circulation pattern of the flow and two corner vortices near the bottom of the cavity. Compared with those in laminar LDC flows, the bottom corner vortices in the turbulent LDC flow are much stronger. A significant distortion (flattening) of the main circulation flow

field appears at the location where the right hand side bottom corner vortex and the main circulation flow contact. Figures 6.4 and 6.5 show the secondary flow pattern of the flow on vertical mid-planes normal to, respectively, the x- and y-directions. A slight asymmetry of the flow pattern is displayed, which is probably due to the limited averaging time in the simulation. Only an extremely weak corner vortex and the accompanying TGL vortex can be identified in the vicinity of the left portion of the bottom (see Figure 6.4), which implies that the low aspect ratio of the LDC flow may strengthen the inter-action between clockwise and anti-clockwise corner or TGL vortices, and therefore significantly weaken all of them.

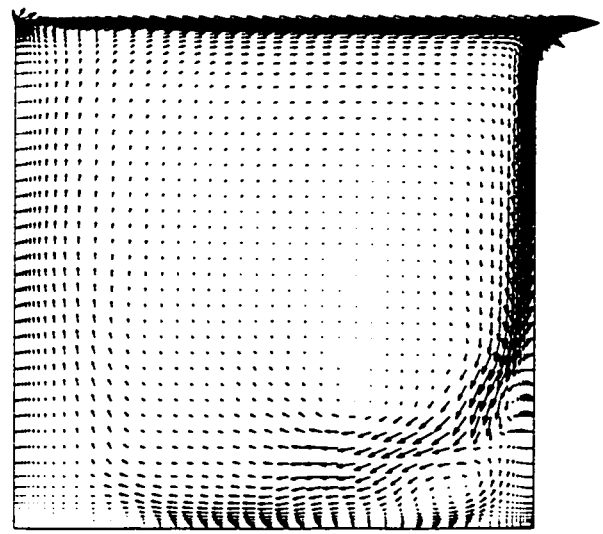

Figure 6.3: Velocity vector $(\overline{\tilde{U}}, \overline{\tilde{W}})$ of 3-D turbulent LDC flow at $y/L_y = 0.5$

The pressure field of the flow is shown in Figure 6.6. As was expected, the maximum pressure occurs at the downstream end of the lid, which is the main driving mechanism of the clockwise recirculation of the flow. The second highest pressure occurs at the location where the downward flow contacts the bottom of the cavity, which drives a portion of the flow backward forming the strong right corner vortex.

The instantaneous values of the SGS Reynolds stress tensor τ_{ij} and the SGS eddy diffusivities α_j represent a total of 12 field parameters in the present simulation. We

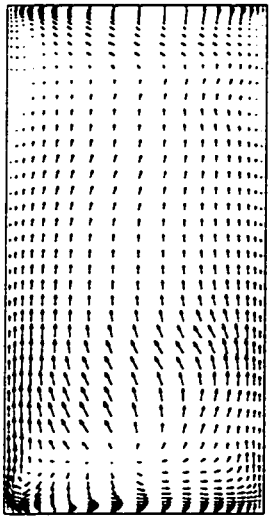

Figure 6.4: Velocity vector $(\overline{\tilde{V}}, \overline{\tilde{W}})$ of 3-D turbulent LDC flow at $x/L_x = 0.5$

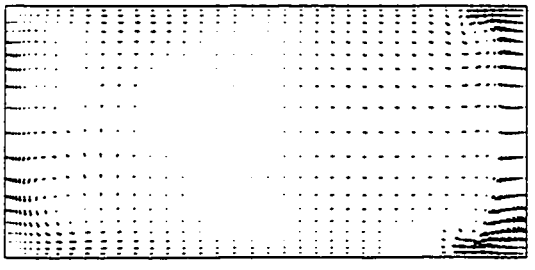

Figure 6.5: Velocity vector $(\overline{\tilde{V}}, \overline{\tilde{W}})$ of 3-D turbulent LDC flow at $z/L_z = 0.5$

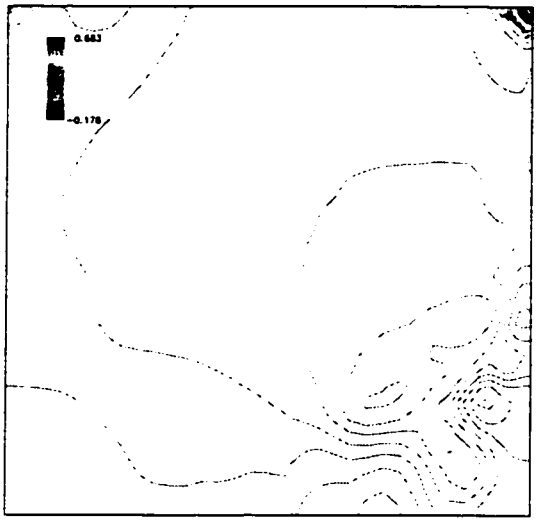

Figure 6.6: Pressure ($\tilde{P}$) of 3-D turbulent LDC flow at $y/L_y = 0.5$

list in Table 6.1 the ranges of the values of each of these parameters taken at the last time step of the simulation. Note that all values shown are normalised by the velocity U_0. It is found that the SGS turbulent fluctuation level of the present turbulent LDC flow simulation is approximately ten times lower than that of the turbulent BDC flow simulation described in the next section. Additionally, in Figures 6.7 and 6.8, the contours of the two selected parameters, τ_{13} and α_1, at the mid-plane normal to the y-direction are displayed. In general, the SGS turbulence of the flow is stronger after the separation point of the downward boundary layer on the end wall of the cavity, but weaker near the top lid. The former behaviour is reasonable, but the latter contradicts the experimental results of Prasad & Koseff (1989), in which the peak value of $< u'^2 >$, the auto-correlation of the turbulent fluctuation, appears close to the top lid (see Figure 6 of Prasad & Koseff (1989)). The reason for this contradiction could be that the clipping algorithm applied in the present simulation to avoid numerical divergence is too 'strong' in regions close to the top lid.

The profile of $\overline{\tilde{W}}$ across the horizontal centreline and that of $\overline{\tilde{U}}$ across the vertical centre-line are plotted, respectively, in Figures 6.9 and 6.10. The corresponding results

Table 6.1: Ranges of normalised values of SGS-related parameters (3-D turbulent LDC flow)

Parameter	Minimum	Maximum
τ_{11}	-5.506×10^{-3}	$0.\times10^{0}$
τ_{12}	-2.675×10^{-3}	8.512×10^{-4}
τ_{13}	-4.344×10^{-4}	3.336×10^{-3}
τ_{21}	-2.675×10^{-3}	8.512×10^{-4}
τ_{22}	-5.449×10^{-3}	$0.\times10^{0}$
τ_{23}	-1.894×10^{-3}	1.739×10^{-3}
τ_{31}	-4.344×10^{-4}	3.336×10^{-3}
τ_{32}	-1.894×10^{-3}	1.739×10^{-3}
τ_{33}	-2.691×10^{-2}	$0.\times10^{0}$
α_1	$0.\times10^{0}$	6.384×10^{0}
α_2	$0.\times10^{0}$	4.398×10^{0}
α_3	$0.\times10^{0}$	7.190×10^{0}

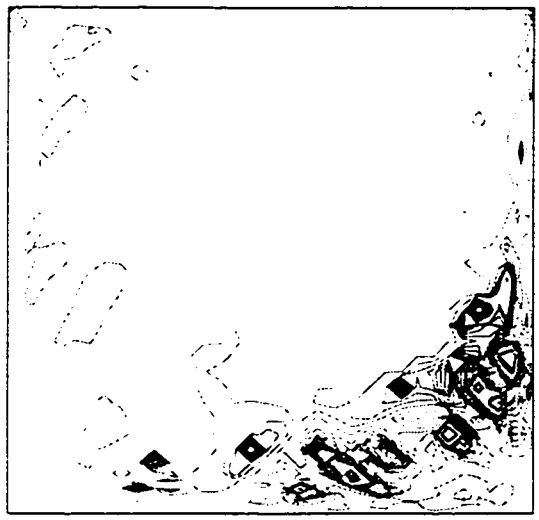

Figure 6.7: τ_{13} of 3-D turbulent LDC flow at $y/L_y = 0.5$

Figure 6.8: α_1 of 3-D turbulent LDC flow at $y/L_y = 0.5$

from the experiment of Prasad & Koseff (1989) are also plotted for comparison. It is found that the present simulation matches reasonably well with the experiment in both plots. Comparison of the above profiles with the corresponding profiles obtained from the LES of Zhang *et al.* (1993) (see Figure 5 of the publication) shows that both obtained good predictions of the velocity profile near the lid and downward boundary layer. The present simulation predicts a better profile in the left side upward boundary layer, while Zhang *et al.* (1993) obtained a better profile in the bottom leftward boundary layer.

The time histories of the four resolvable fields, *i.e.* $\tilde{U}$, $\tilde{V}$, $\tilde{W}$, $\tilde{P}$ at a point 0.06 m from the bottom of the cavity during the last 800 time steps are plotted in Figure 6.11. Although the time period of "recording" is not long enough, the temporal fluctuation of the resolvable fields are captured. It is found that the time history plots for the resolvable velocity field is smoother than that for the resolvable pressure, indicating that pressure plays an important role in turbulence production.

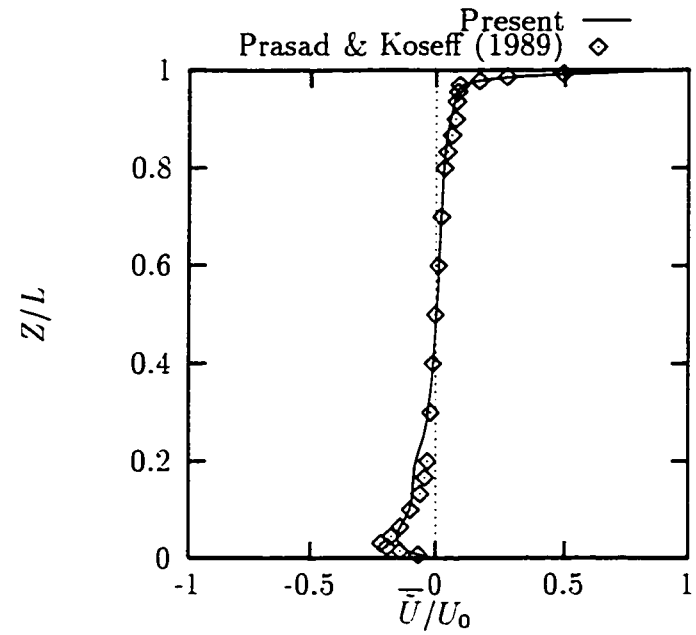

Figure 6.9: Profile of $\overline{\tilde{U}}$ of 3-D turbulent LDC flow along vertical mid-line

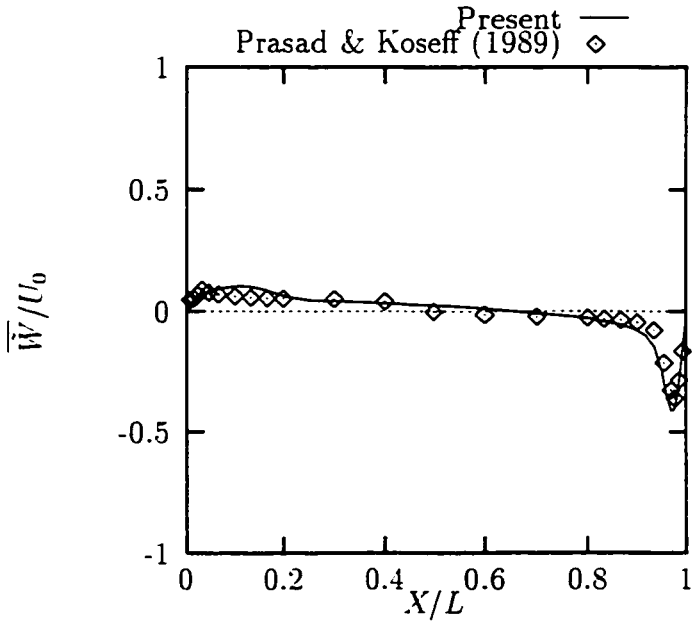

Figure 6.10: Profile of $\overline{\tilde{W}}$ of 3-D turbulent LDC flow along horizontal mid-line

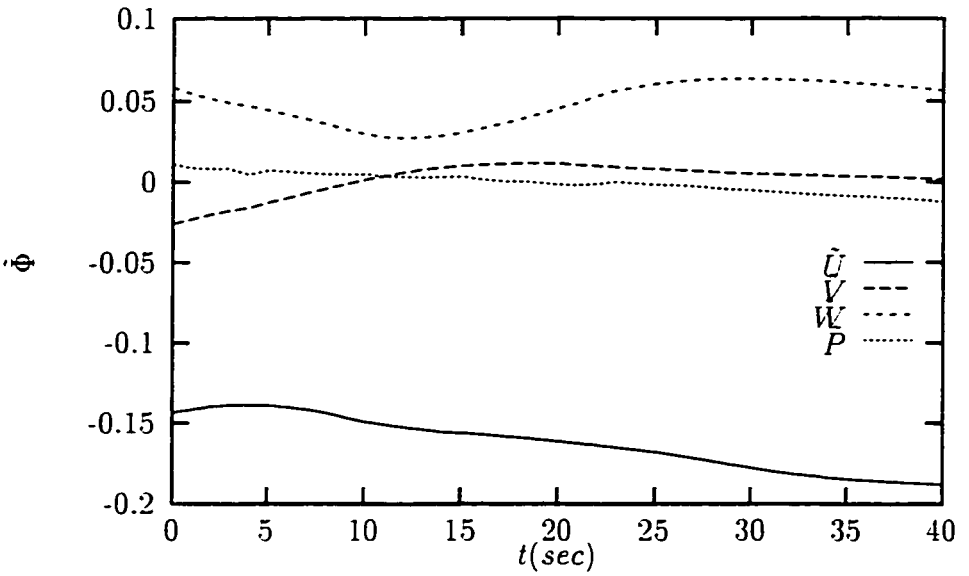

Figure 6.11: Time history of the fields $\tilde{U}$, $\tilde{V}$, $\tilde{W}$, $\tilde{P}$ at node (26,11,10)

6.3 3-D Buoyancy-Driven Cavity Flow, $Ra = 10^{10}$

6.3.1 Flow Configuration

The solution domain of the 3-D buoyancy-driven turbulent cavity flow is also a cuboid of size $L_x \times L_y \times L_z$, as shown in Figure 6.12.

We selected $L_x = L_z = 1\ m$, and $L_y = 0.8\ m$ which is slightly larger than that for the lid-driven case. All boundaries of the domain are solid walls without motion, at which the no-slip condition is applied. Both the hot wall (at $x = 0$) and cold wall (at $x = L_x$) are isothermal and the temperature difference between them is $\Delta\Theta$. All other walls are assumed to be adiabatic. The Rayleigh number of the flow has been defined in equation (5.1), while the characteristic length here is defined as $L = L_x = L_z$. In order to obtain significant turbulent flow, we chose $Ra = 10^{10}$ which corresponds to $\Delta\Theta = 1.143\ K$. The flow is believed to show some features of turbulence when the Rayleigh number exceeds 10^8.

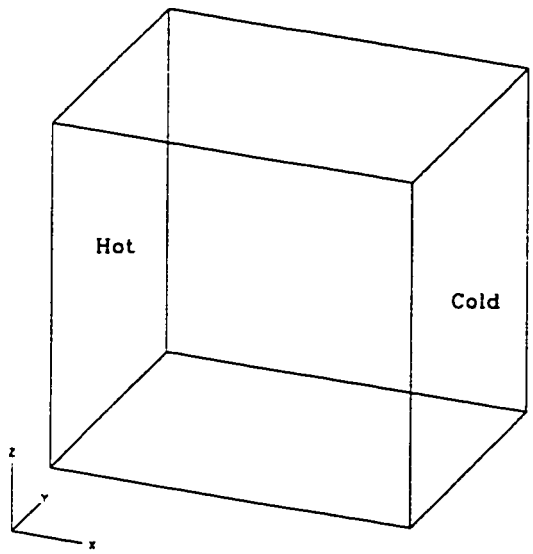

Figure 6.12: Solution domain of 3-D buoyancy-driven turbulent cavity flow

One challenge in simulating high Rayleigh number buoyancy-driven cavity flow is that, due to low values of the molecular diffusivities, boundary layers on both hot and cold vertical walls are extremely thin. The horizontal profile of the vertical velocity component has two polar points which are very close to, respectively, the hot and cold walls. This requires a high near-wall-resolution in the grid to place a sufficient number of cells between the wall and the polar points. Therefore, we employed a relatively fine grid with $61 \times 41 \times 61$ control volumes as shown in Figure 6.13. It is noted that the grid is highly refined near the cavity walls, which causes high aspect ratios (with a maximum 180:1) for control volumes there. Application of the grid requires 78 MB memory (double precision) in a SUN SPARCstation 5 (with maximum virtual memory of 216 MB) of the CFD group at the University of Saskatchewan.

The turbulent BDC flow and its 2-D counterpart has been investigated numerically using methods other than the LES. First of all, the DNS method was employed by several researchers. Among them are: Paolucci (1990) who simulated the 2-D flow

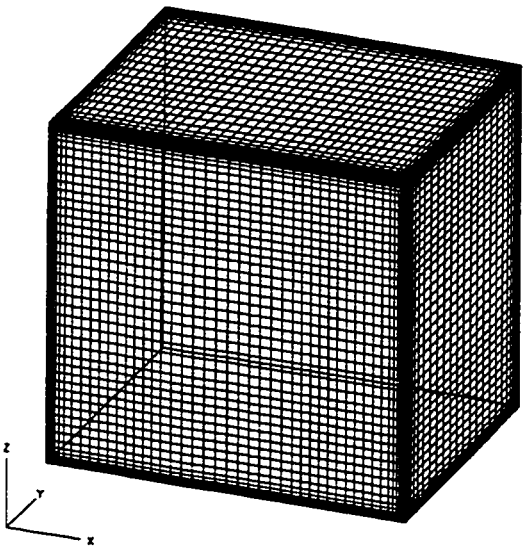

Figure 6.13: Grid for solution of 3-D turbulent BDC flow

with a grid of 121 × 121 control volumes; Fusegi *et al.* (1991) who simulated the 3-D flow with a relatively coarse grid (121 × 62 × 62 resolution) for Rayleigh numbers from $Ra = 10^3$ up to $Ra = 10^{10}$; Xin & Le Quere (1994) who simulated the 2-D flow on a very fine grid of 256 × 321 control volumes; and Xin & Le Quere (1995) who simulated the 2-D flow with an aspect ratio 1/4 at a Rayleigh number based on the cavity height of $Ra_h = 10^{10}$. It should be pointed out that turbulence in the 2-D BDC flow is still a 3-D phenomenon which should be simulated three-dimensionally. However, in order to save computer resources, all of the above simulations of the 2-D BDC flow were performed with 2-D numerical schemes. This simplification may result in considerable errors in the final results of the simulation. Secondly, the RAM method was also employed to simulate the turbulent BDC flow. Hanjalic and Vasic (1993) simulated the 2-D flow up to $Ra = 10^{12}$ using the RAM method with an algebraic closure model. Barakos & Mitsoulis (1993) simulated the 2-D flow up to $Ra = 10^{10}$ using both the DNS method (implicit time stepping) and the RAM method (the $k - \epsilon$ models with and without wall-function). On the other hand, due to difficulties

associated with experimental realization of the thermal boundary conditions, only a limited number of experimental investigations on this or similar flows have been reported. Cheesewright *et al.* (1986) studied experimentally the buoyancy driven flow in a 2-D cavity with an aspect ratio of 1/5 at $Ra_h = 7.1 \times 10^{10}$. More recently, Hoogendoorn *et al.* (1996) provided experimental measurement results for the 3-D flow in an almost cubic cavity at $Ra = 4.9 \times 10^{10}$.

6.3.2 Results and Discussion

Firstly, some qualitative results of the simulation are shown in the form of contour and vector plots. Figures 6.14 through 6.17 show the time averaged resolvable fields at specific cross sections in the solution domain. The benchmarks, with which these qualitative results of the simulation can be compared are the simulation results of Paolucci (1990), Fusegi *et al.* (1991), and Barakos *et al.* (1994). The pattern of the primary velocity field obtained by the present simulation (Figure 6.14) is extraordinarily similar to that of Paolucci (1990). Both show strong vortices near the top and bottom walls of the cavity and the locations of these vortices match well with each other. Secondly, the primary temperature fields obtained (see Figure 6.15) also closely resemble Paolucci's (1990) prediction. However, the tiny "hook" flow pattern caused by sinusoidal disturbances of small amplitudes near vertical surfaces shown in Paolucci's (1990) temperature contours does not appear in the temperature contour of the present simulation. This is probably due to the lower grid resolution applied in the present simulation. On the other hand, the primary flow pattern and temperature contour of the present simulation do not match those of Fusegi *et al.* (1991) and Barakos *et al.* (1994). Their temperature contours show thinner boundary layers near hot and cold walls, and are strongly stratified along the vertical direction (refer to Plate 3 in Fusegi *et al.* (1991) and Figure 6 in Barakos *et al.* (1994)). No top or bottom vortex appears in the velocity vector plot of Barakos *et al.* (1994). These laminar-like features of the flow fields suggest that, without using the SGS model, the

80×80 grid employed by Barakos *et al.* (1994) or the $121 \times 61 \times 61$ grid employed by Fusegi *et al.* (1991) are still too coarse to fully capture the turbulent effect of this flow in simulation, even though the grids are already finer than what was employed by the present simulation. Three-dimensionality of the obtained flow fields is weak; it is apparent only in regions close to the corners of the cavity. Three-dimensionality of the temperature field is exhibited in Figures 6.16 and 6.17.

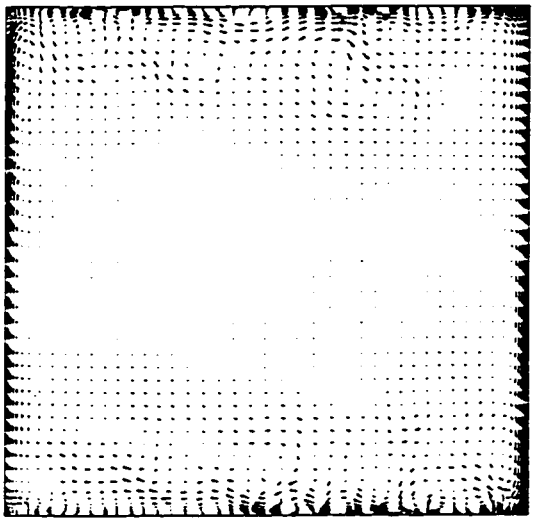

Figure 6.14: Velocity ($\overline{\tilde{U}_i}$) vector of 3-D turbulent BDC flow at $y/L_y = 0.5$

The contour of the pressure field (normalised by the buoyancy velocity U_b) is exhibited in Figure 6.18 which shows high pressure regions near the top corner of the hot wall and bottom corner of the cold wall indicating that horizontal motion of the flow is driven mainly by the pressure gradients built up there.

The instantaneous fields of the SGS Reynolds stress tensor τ_{ij}, the SGS turbulent heat flux σ_j, and the eddy diffusivities α_j are unique to the present simulation. We list in Table 6.2 the ranges of the values of each of these parameters taken at the last time step of the simulation (normalised by the buoyancy velocity U_b and/or the temperatur difference $\Delta\Theta$). It is noted that the magnitudes of even the normalised SGS turbulence parameters for the BDC turbulent flow are more than 10 times larger

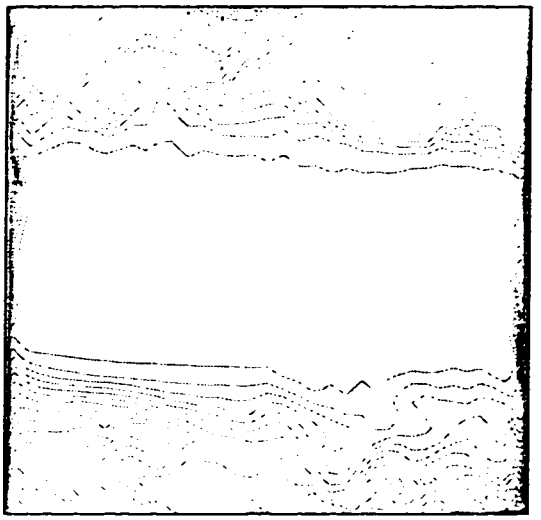

Figure 6.15: Isothermal ($\overline{\Theta}$) of 3-D turbulent BDC flow at $y/L_y = 0.5$

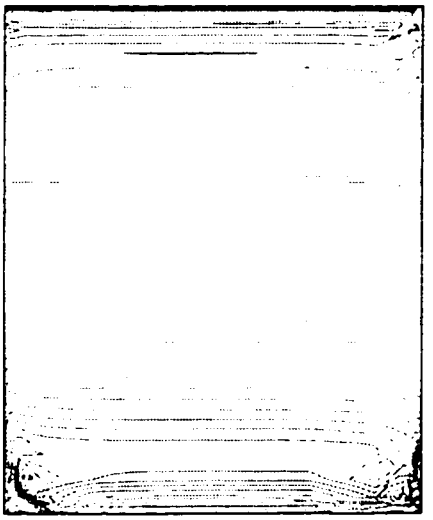

Figure 6.16: Isothermal ($\overline{\Theta}$) of 3-D turbulent BDC flow at $x/L_x = 0.0042$

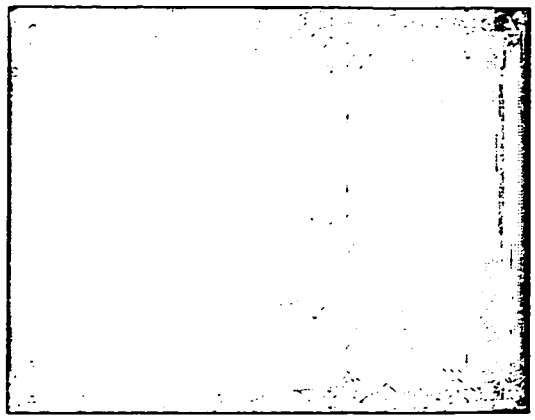

Figure 6.17: Isothermal ($\overline{\Theta}$) of 3-D turbulent BDC flow at $z/L_z = 0.0042$

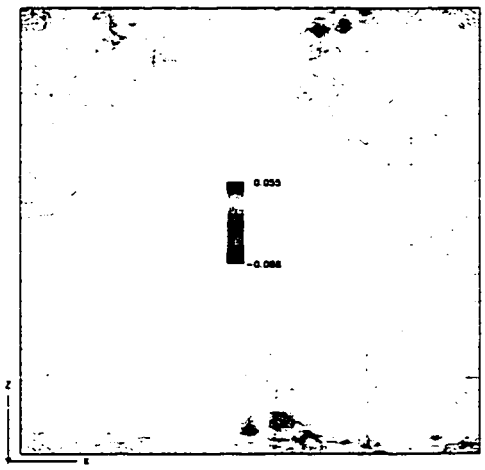

Figure 6.18: Pressure ($\tilde{P}$, normalised by $\rho_0 {U_b}^2$) of 3-D turbulent BDC flow at $y/L_y = 0.5$

than those for the LDC turbulent flow discussed above (the velocity scale for normalization in the BDC flow is approximately 12 times that of the LDC flow), indicating that turbulence is a strong nonlinear process. Additionally, in Figures 6.19 through 6.21, the contours of the three selected parameters at the mid-plane normal to the y-direction are displayed. It is found that magnitudes of the SGS turbulence parameters are high near the top and bottom wall, low near the hot and cold walls, and almost zero in the centre region of the cavity.

Table 6.2: Ranges of normalised values of SGS-related parameters (3-D turbulent BDC flow)

Parameter	Minimum	Maximum
τ_{11}	-2.175×10^{-1}	$0.\times10^{0}$
τ_{12}	-7.603×10^{-2}	7.110×10^{-2}
τ_{13}	-6.745×10^{-2}	5.960×10^{-2}
τ_{21}	-7.603×10^{-2}	7.110×10^{-2}
τ_{22}	-2.005×10^{-1}	$0.\times10^{0}$
τ_{23}	-4.355×10^{-2}	6.504×10^{-2}
τ_{31}	-6.745×10^{-2}	5.960×10^{-2}
τ_{32}	-4.355×10^{-2}	6.504×10^{-2}
τ_{33}	-1.898×10^{-1}	$0.\times10^{0}$
σ_1	-8.866×10^{-2}	6.081×10^{-2}
σ_2	-6.144×10^{-2}	3.549×10^{-2}
σ_3	-3.534×10^{-2}	4.615×10^{-2}
α_1	$0.\times10^{0}$	2.876×10^{2}
α_2	$0.\times10^{0}$	1.734×10^{2}
α_3	$0.\times10^{0}$	2.625×10^{2}

The quantitative results are shown in terms of the averaged temperature and vertical velocity component profiles across the horizontal centre-line from the hot to cold walls (Figures 6.22 and 6.23). In order to show their near wall detail, 'blown up' profiles near the hot wall are shown in Figures 6.24 and 6.25. The corresponding results from Paolucci (1990), Xin & Le Quere (1994) (2-D simulations), and Hoogendoorn (1996) (3-D experiment) are also plotted for comparison. The present vertical velocity component profile matches quite well with that from Paolucci's (1990) simulation, but is different from that of Xin & Le Quere (1994). It seems that the flow field ex-

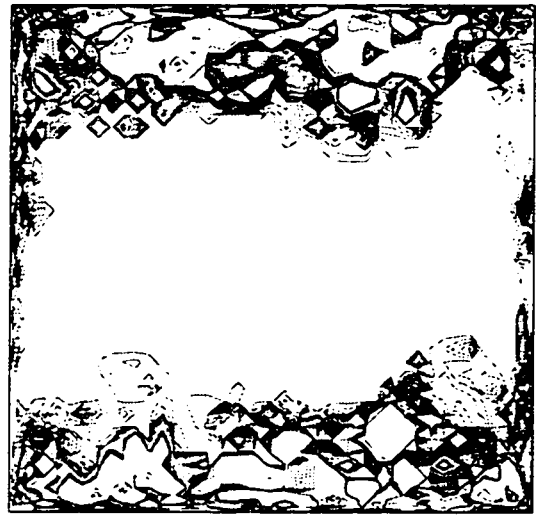

Figure 6.19: τ_{13} of 3-D turbulent BDC flow at $y/L_y = 0.5$

Figure 6.20: σ_3 of 3-D turbulent BDC flow at $y/L_y = 0.5$

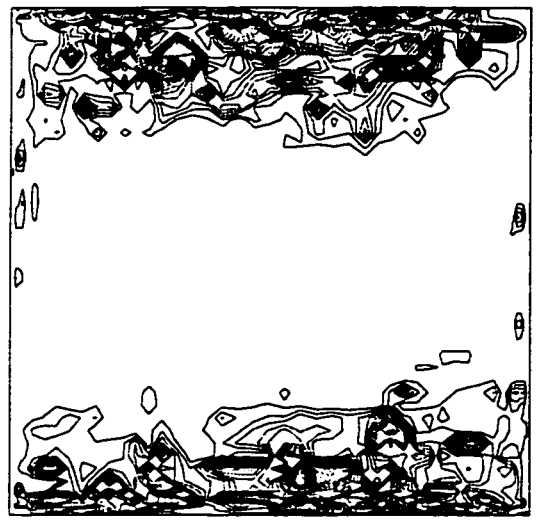

Figure 6.21: α_1 of 3-D turbulent BDC flow at $y/L_y = 0.5$

hibited by Xin & Le Quere (1994) is not yet fully developed, since the most turbulent regions in their last predicted flow fields are still next to the vertical surfaces rather than near the top and bottom walls (see Figure 6 in Xin & Le Quere (1994)). The author of thesis also observed such an intermediate field in his simulation procedure. It is noted that Xin & Le Quere (1994) employed a grid of extremely fine resolution to satisfy the requirement of the DNS method. However, the trade-off in doing this is a significant increase in computing burden and systematic (machine round-off) error involved. This drawback of the DNS method was mentioned in section 2.2.

Finally, all resolvable fields at a specific node approximately 0.03 m below the top wall of the cavity versus time are plotted in Figure 6.26 for the last 1000 simulation time steps to show the temporal fluctuations. It is found that the fluctuation of the resolvable fields is not as violent as those of the instantaneous fields obtained from the DNS of Paolucci (1990) and Xin & Le Quere (1994). This is appearently due to the effect of the volume average approach. Again, it is found that the resolvable pressure fields fluctuate more than the other resolvable fields.

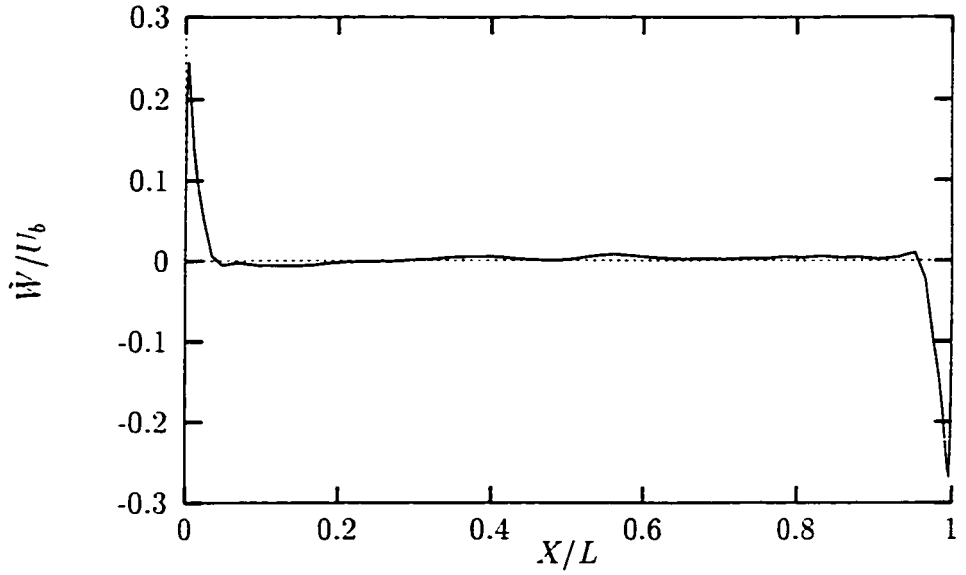

Figure 6.22: Profile of $\overline{\bar{W}}$ of 3-D turbulent BDC flow along horizontal mid-line

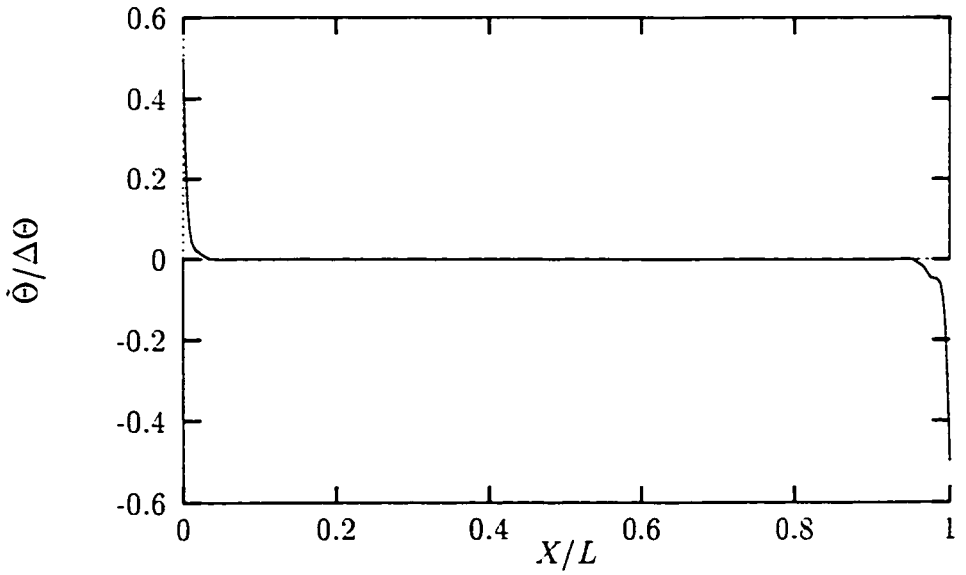

Figure 6.23: Profile of $\overline{\bar{\Theta}}$ of 3-D turbulent BDC flow along horizontal mid-line

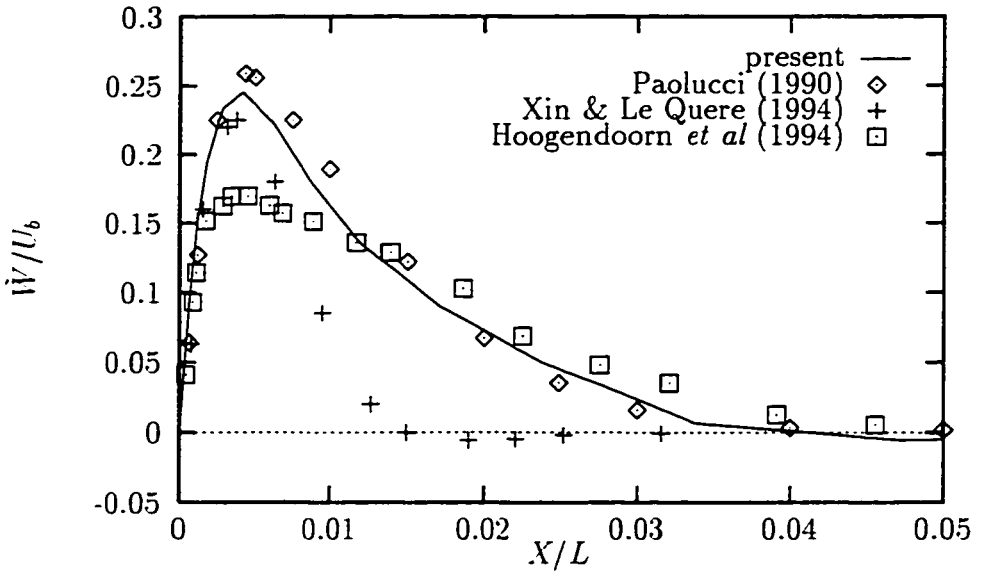

Figure 6.24: Profile of $\overline{\dot{W}}$ of 3-D turbulent BDC flow along horizontal mid-line near hot wall

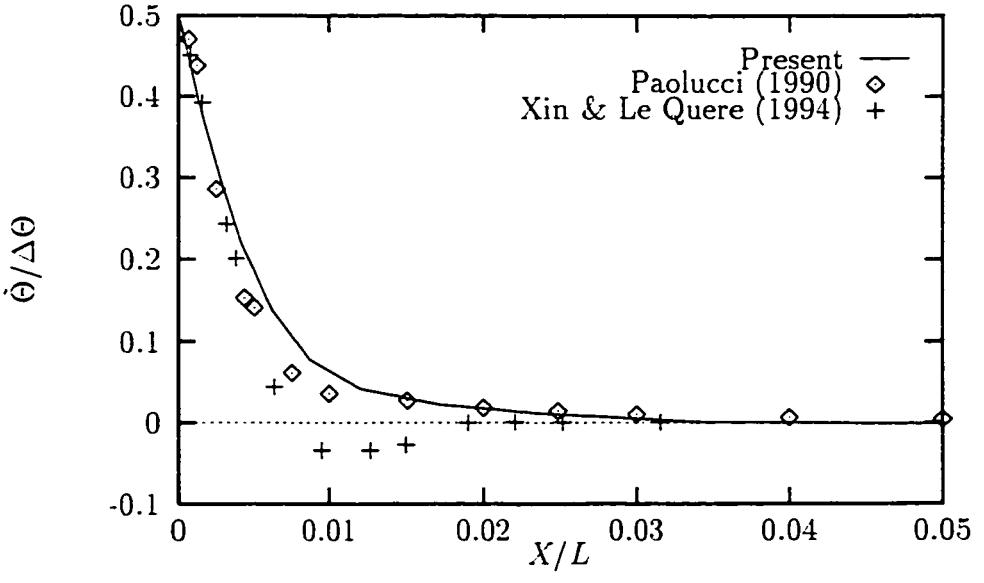

Figure 6.25: Profile of $\overline{\Theta}$ of 3-D turbulent BDC flow along horizontal mid-line near hot wall

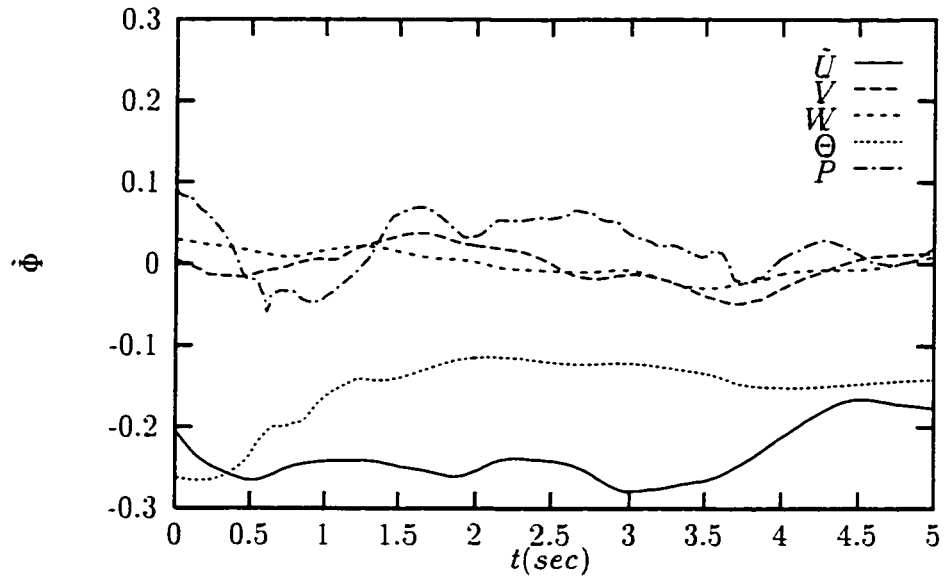

Figure 6.26: Time history of the fields $\tilde{U}$, $\tilde{V}$, $\tilde{W}$, $\tilde{\Theta}$, $\tilde{P}$ at node (31,21,54)

6.4 Summary

Preliminary benchmark tests for the VAT have been carried out by applying it to the LES of LDC and BDC turbulent flows. Although relatively coarse grids were employed (in the sense of the conventional LES), both of the simulations obtained reasonable predictions for the resolved fields (time averaged) and their temporal fluctuations. The predicted magnitudes and distributions of the SGS turbulence parameters for both simulations are exhibited and discussed.

An application of the VAT to room airflow prediction is discussed in the next chapter. Although we call it "application", the main purpose of that simulation is still to test the VAT developed. An added feature of the room airflow is that it is more three-dimentional and convective.

Chapter 7

Room Airflow Prediction

7.1 Introduction

As was pointed out in Section 1.3, airflow in air-conditioned rooms is a kind of fluid motion, possibly with multiple regimes, which is difficult to simulate accurately using the RAM method due to its inherent limitations. The LES method is free from these limitations, and therefore potentially a promising numerical tool for room airflow predictions.

In this chapter, we present the results of an application of the VAT, a newly developed technique of the LES method, to room airflow simulation. First of all, previous work pertaining to room airflow predictions, both numerical and experimental, is briefly reviewed. The room airflow considered in the present chapter is one which has been experimentally investigated, so that our simulation results can be compared against the corresponding experimental data, even though they are limited.

7.2 Brief Review of Previous Work

7.2.1 Numerical Predictions

The prediction of airflow in rooms started in the 1970's. Most of the earlier simulation work pertaining to airflow in a room was carried out using the $k-\epsilon$ models or low-Reynolds-number $k-\epsilon$ models, as reviewed by Rhodes (1989) and Chen & Jiang (1992). The technique has been applied to study velocity, temperature, turbulence intensity, humidity, and contaminant concentration fields in rooms of various configurations.

In the late 1970's, Nielsen *et al.* (1978) proposed to develop a standard benchmark to validate and compare different simulation models for room airflow prediction. An isothermal airflow in a quasi 2-D room, shown in Figure 7.1, was selected and used by the IEA (International Research Team). Detailed experimental investigation on the flow was carried out using LDA (Laser Doppler Anemometry), and the experimental data obtained served as the benchmark for validation of simulation models. However, this flow is in fact far removed from a real room airflow. It is actually a 2-D wall jet in a wall-bounded enclosure and exhibits flow patterns similar to those of 2-D lid-driven cavity flow or back-step flow. Although most reported $k-\epsilon$ model simulations of this standard 2-D room case achieved encouraging results (see Chen & Jiang, 1992), the semi-empirical nature of the $k-\epsilon$ model makes it unsuitable for simulations of other more complicated room airflow, *e.g.* 3-D or non-isothermal flows. This fact has been confirmed by some more recent $k-\epsilon$ model simulations of room airflow with increased complexity. Among them are the simulations of William *et al.* (1992), Weather *et al.* (1993)), Said *et al.* (1995), Murakami *et al.* (1991), Haghighat *et al.* (1991), and Gan (1995). It seems that the $k-\epsilon$ models may perform well for specific flow conditions and lead to simulation results that agree well with the corresponding experimental data. However, this is not always the case. When flow conditions change, the $k-\epsilon$

models may lead to a poor agreement between simulation results and the experimental counterparts.

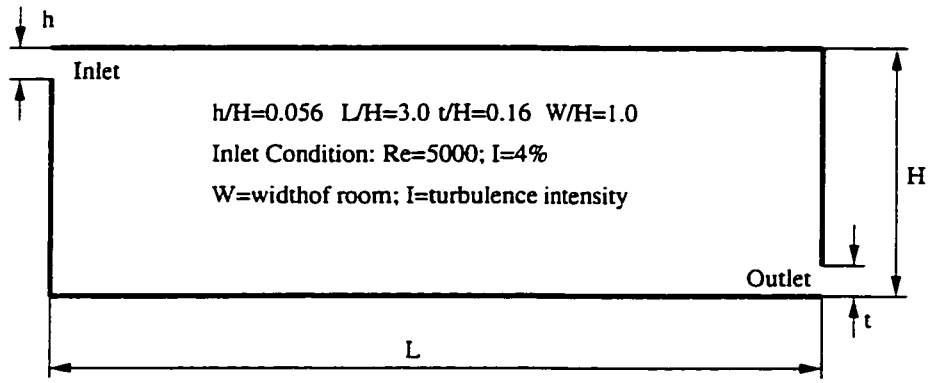

Figure 7.1: Sketch of quasi 2-D case used by IEA

Application of the SMC (Second Moment Closure) model to room airflow prediction started in the 1990's. The model was first used by Murakami *et al.* (1990) and Renz & Terhaag (1990) to simulate airflow in a room with jets. More recent work was reported by Murakami *et al.* (1992), Kato *et al.* (1993), and Chen *et al.* (1996). Comparisons with the $k-\epsilon$ model made in the above SMC model simulations were generally favourable to the SMC model, which shows the advantage of the SMC model over the $k-\epsilon$ model in simulations of room airflow with a simple recirculating flow pattern. However, the SMC model shares with the $k-\epsilon$ model the problems of inappropriate assumptions and empirically determined coefficients, and more computing effort is required by the SMC model. Therefore, it is difficult to conclude that the SMC model is more reliable than the $k-\epsilon$ model for prediction of real-world complex room airflow.

To the author's knowledge, application of the LES method to room airflow prediction is just beginning. The only published work is that by Davidson (1997) who used a dynamic one-equation SGS eddy viscosity model to simulate an isothermal wall-jet-driven recirculating flow in a 9 m × 3 m × 3 m room with 96 × 64 × 64 grid. Some encouraging results were obtained. However, since the flow configuration considered is simple, the advantage of the LES method were not apparent in this study.

7.2.2 Experimental Measurements

Let's turn to experimental measurements of room air flow in this subsection. Only experimental investigations of room airflow which provide benchmark data for verifying numerical models are discussed. The experimental measurements of the quasi 2-D case shown in Figures 7.1 is one of the earliest investigations. As was pointed out above, the experimental results of this flow have been broadly employed as a benchmark to test simulation models, and they are still in use (Davidson, 1997 and Chen, 1996). Since experimental measurements with high resolution of the temperature, pressure, and velocity fields in a full size air conditioned room requires a tremendous investment in equipment and installation, only a few full size experiments have been reported. Some of these are described below. (Describing these studies will retain the use of the British unit system where it was originally employed, even though the SI unit system is applied throughout this thesis.)

Similar experiments on a slightly different room airflow configuration than that of Nielsen *et al.* (1978) were performed by Zhang *et al.* (1992) and Hawkins *et al.* (1995). Figure 7.2 is a sketch of the room airflow experiment by Zhang *et al.* (1992). The Q represents a heat source (cooling load) on the room floor, so that the flow is closer to real ventilation than Nielsen *et al.*'s (1978) quasi 2-D case. The experimental results were employed by Nady *et al.* (1995) and Zhang *et al.* (1993) to check the validity of their simulation results. Figure 7.3 shows another strongly 2-D room airflow configuration studied experimentally by Hawkins *et al.* (1995).

An experiment on a full size 3-D room airflow configuration was performed by Weather & Spitler (1993). Measurements were made in a $15' \times 9' \times 9'$ room with a sidewall inlet (see Figure 7.4). The flow rate in the room was varied between 15 and 100 ACH (Air Changes per Hour). The inlet flow temperature was kept at 21°C, which is lower than or equal to the side wall temperature. The measured results were employed to test the numerical model of Weather & Spitler (1993), and that of Williams *et al.* (1994).

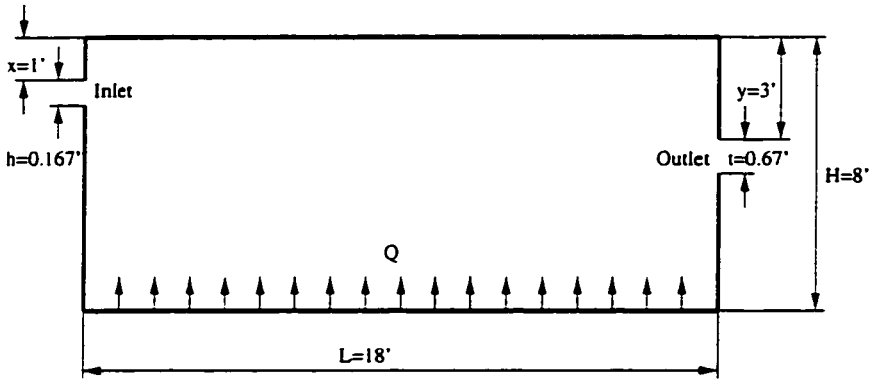

Figure 7.2: Quasi 2-D room airflow measured by Zhang *et al.* (1992)

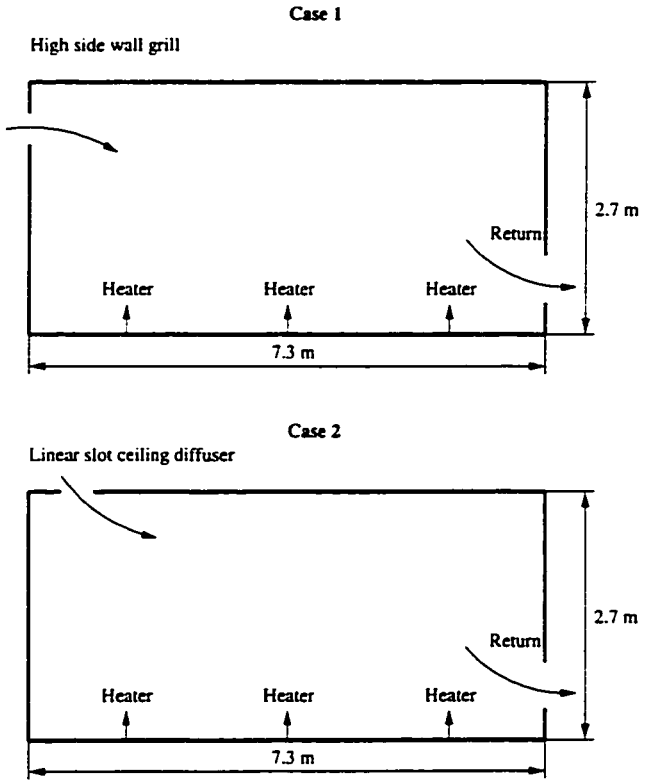

Figure 7.3: Quasi 2-D room airflow measured by Hawkins *et al.* (1995)

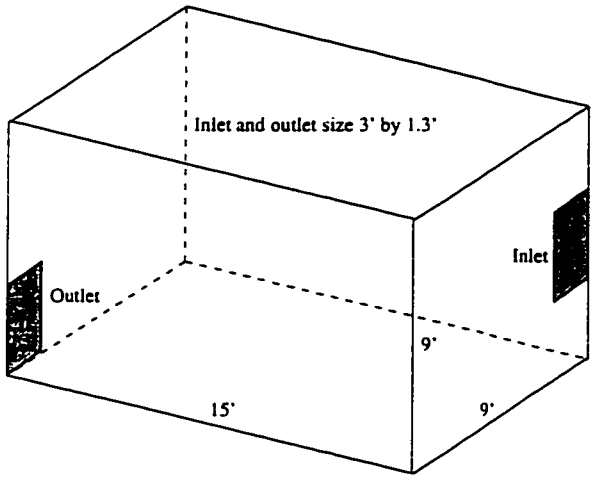

Figure 7.4: 3-D room airflow measured by Weather & Spitler (1993)

Isothermal air flow in a full size room with ceiling mounted supply and return diffusers was experimentally investigated by Jouini *et al.* (1994), whose configuration is shown schematically in Figure 7.5. In this experimental study, only the velocity, turbulent fluctuation and turbulence intensity on the measurement plane were obtained. Thus, the data obtained in this experiment are effectively 2-D rather than 3-D.

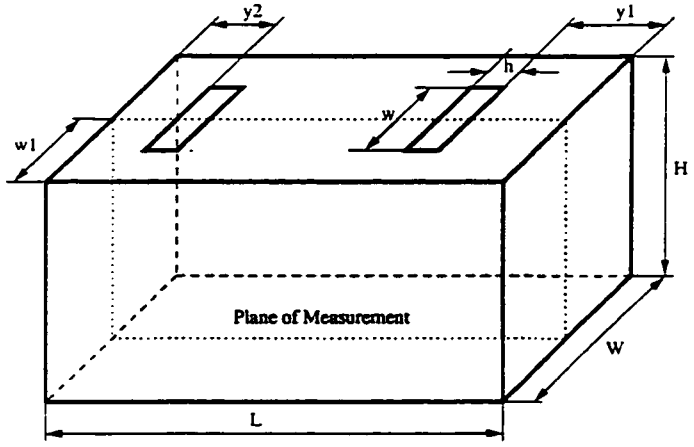

L=4.75 m, H=2.87 m, W=4.87 m, w=1.016 m, h=0.0127 m, y1=2.141 m, y2=0.806 m, w1=2.335 m

Figure 7.5: 3-D room airflow measured by Jouini *et al.* (1994)

In summary, only the room airflow experiment performed by Weather & Spitler (1993) can be viewed as a real 3-D experiment. Numerical simulations of this flow has been reported by at least two groups of researchers, namely William *et al.* (1994) and Weather & Spitler (1993). Therefore, it is the most suitable candidate for us to

simulate using the VAT developed in the present study. In the following sections, the VAT simulation of the flow is discussed in detail.

7.3 Room Airflow Configuration

Although in Weather & Spitler's experiment a wide range of discharge flow rates (from 15 to 100 ACH) and wall temperatures were tested, only one of the cases was selected for the present simulation. This case was also selected for the simulation of Williams *et al.* (1994). The inlet conditions for the simulation are given in Table 7.1. The mean inlet velocities have only x-direction components and are assumed to be uniformly distributed over the inlet area. Since no turbulence fluctuation data are available from the experiment, the frequencies of the dominant turbulent fluctuation are assumed to be determined by the inlet mean velocity V_{in} and the length scale of the inlet grille grid (L_g) which is set to be $0.05m$ in the simulation. The inlet turbulence intensity I_t are estimated based on equation (3.41) by assuming that the magnitude of turbulent diffusion is 29 times that of the molecular diffusion (see Appendix A.3). This assumption was also adopted in the simulation of Williams *et al.* (1994).

Table 7.1: Inlet conditions of simulation

$Q_{in}(ACH)$	$V_{in}(m/s)$	$\Theta_i(°K)$	I_t	$f_t(Hz)$
30	0.8	-5.56	2.44%	$\frac{V_{in}}{L_g}$

The outlet mean velocities are specified except at the corner of the room where the velocity boundary condition is opened to avoid over-specification. The specified outlet mean velocities also have only x-direction components and are assumed to be uniformly distributed over the outlet area. The value of the outlet mean velocity V_{out}

is calculated according to global continuity requirement of the flow as

$$V_{out} = V_{in}\frac{A_{in}}{A_{out}} = 1.013645224 V_{in}$$

where 1.013645224 is the exact ratio of the areas of the inlet and outlet of the room. No turbulent fluctuation is specified and the zero-normal-gradient boundary condition is applied for temperature on the outlet. The temperatures of all the walls are set to be $\Theta_w = 0\ K$.

A non-uniform $31 \times 61 \times 61$ grid is employed for the present room airflow simulation as illustrated in Figure 7.6. Also shown in the figure are the RHS inlet, LHS outlet, and the Cartesian coordinate system. Our grid for the LES of the flow has a total cell number which is approximately 5.7 times that of Williams *et al.*'s (1994) simulation ($21 \times 31 \times 31$) and 2.8 times that of Weather & Spitler's (1993) simulation ($46 \times 30 \times 30$).

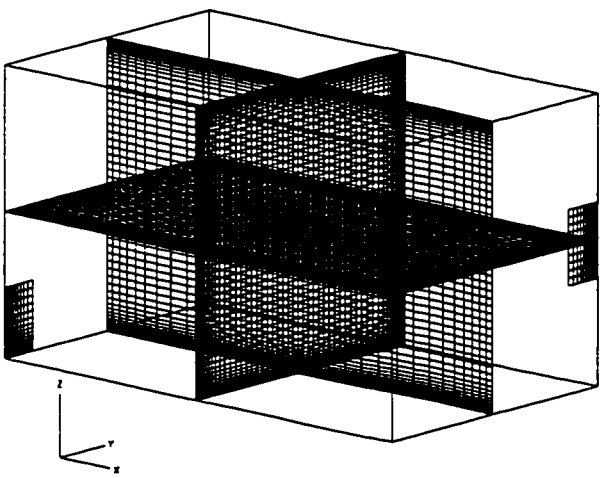

Figure 7.6: Grid configuration for room airflow simulation

7.4 Results and Discussion

The simulation was performed on a SUN-ULTRA workstation of the CFD group at the University of Saskatchewan, which is approximately 1.5 times faster than a SUN-SPARCstation 5. Starting from zero initial fields, the room airflow was first solved three-dimensionally without using the SGS model for 1000 time steps ($\Delta t = 0.01$ *sec*). Then, the SGS model was switched on and the flow was further simulated for another 2800 time steps ($\Delta t = 0.002$ *sec*). As we have done in the turbulent cavity flow simulations described in Chapter 6, different values of the weighting factors f_w for time averaging were applied in the simulation procedure of the present room airflow simulation. The f_w was selected to be 0.5 for the first 1000 time steps, 0.995 for the next 1000 time steps, and increased to 0.9995 for the final 1800 time steps. The entire simulation took approximately 250 CPU hours.

It is noted that airflow in an air-conditioned room is generally unsteady due to switching on and off the heating/cooling devices according to heating/cooling loads, motions of occupants inside the room, or the phenomenon of multiple solutions. Additionally, engineers in the HVAC community are interested in not only the ensemble averages but also the large scale fluctuations of turbulent fields in room airflow, since the latter also have significant effects on the thermal comfort (see Wang (1993) for definition). Therefore, the resolvable fields of the present LES room airflow simulation are practically as significant as their time averaged counterparts. To take advantage of the LES method, the final results of the present room airflow simulation are exhibited mostly based on the resolvable fields in this section.

Firstly, the complexity of the room airflow patterns are shown in terms of vector plots on vertical and horizontal centre planes of the inlet and outlet (see Figures 7.7 through 7.10). From Figure 7.7, the inlet jet appears to hit the floor approximately two thirds of the way across the room. Thereafter, the jet moves mainly forward along the floor to hit the opposite wall. The strong upward flow near the opposite wall is caused by residual momentum of the inlet jet and buoyancy force due to the

temperature gradient near the wall. The upward flow produces a clockwise vortex near the opposite wall. The inlet jet has no significant expansion. This feature is clearly shown in Figure 7.8 where the inlet flow velocity vectors retain their initial direction for at least one third of the way across the room. In contrast, the flow pattern near the outlet is more complex (see Figures 7.9 and 7.10). The flow "scatter" after the inlet jet contacts the floor is clearly shown in Figure 7.10.

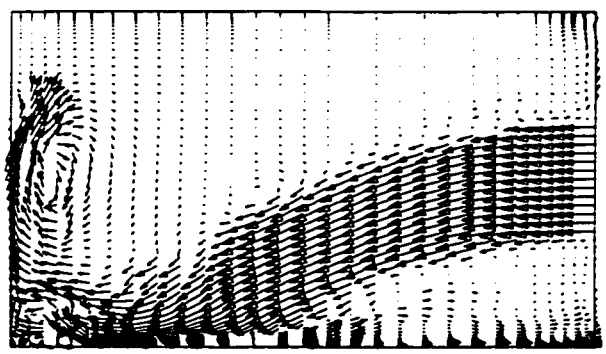

Figure 7.7: Vector plot of (U,W) velocity on vertical centre plane of inlet

The strong three-dimensionality of the final resolvable fields is exhibited in Figures 7.11 and 7.12 for airflow speed, in Figures 7.13 and 7.14 for temperature, and in Figures 7.15 through 7.17 for pressure. The airflow speed and pressure are nomalized by the inlet average speed, while the airflow temperature is nomalized by the difference between inlet flow temperature and the wall temperature. (For legends of the speed, temperature, and pressure contours see, respectively, Figures 7.11, 7.13, and 7.15.) The following features of the flow can be identified from these contours:

1) It is shown in Figures 7.11 and 7.12 that the inlet flow jet has no significant

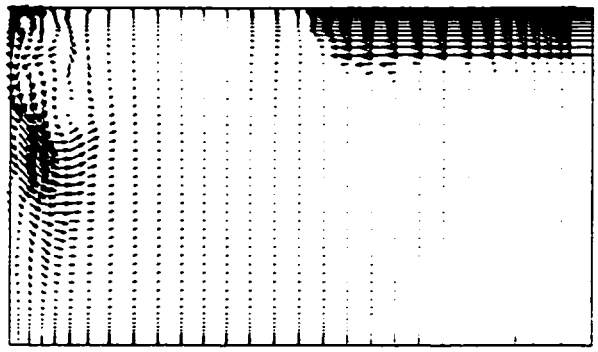

Figure 7.8: Vector plot of (U,V) velocity on horizontal centre plane of inlet

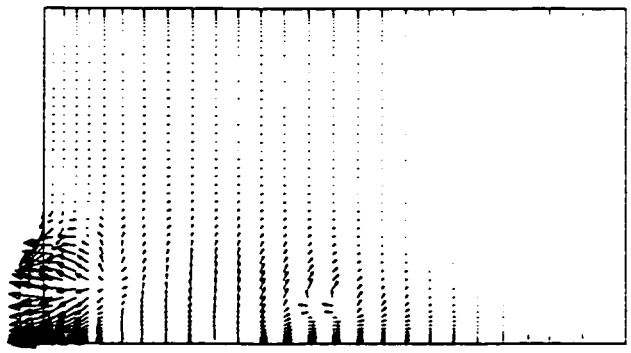

Figure 7.9: Vector plot of (U,W) velocity on vertical centre plane of outlet

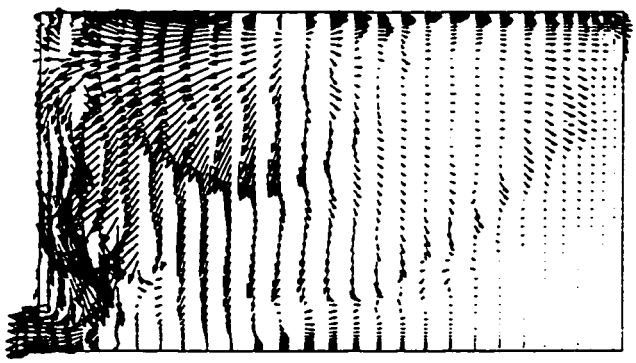

Figure 7.10: Vector plot of (U,V) velocity on horizontal centre plane of outlet

expansion in the transverse direction. This is mainly due to weak turbulent transport and a weak adverse pressure gradient inside the room. The latter is caused by the use of a closed outlet velocity boundary condition, which avoids building up high pressure near the outlet to drive the airflow out. Buoyancy drives the inlet jet significantly downward. The throw of the jet first hits the floor rather than the opposite wall. After hitting the floor, the jet slides forward to meet the opposite wall and creates a strong upward and a relatively weak sideward secondary flow.

2) Flow speed inside the room can be higher than the inlet flow speed in regions near the floor and opposite wall (maximum is 1.62). This is due to the driving mechanism of the buoyancy force.

3) The momentum and energy transfers in the flow are definitely convection dominant. This can be confirmed by the fact that the low temperature region is nearly coincident with the high speed region inside the room.

4) The highest pressure occurs near the corner ($X = 0\ m, Y = 2.7\ m, Z = 0\ m$) of the room, while the next highest pressure peak is at the contact point of the inlet jet with the floor (see Figures Figures 7.15 through 7.17).

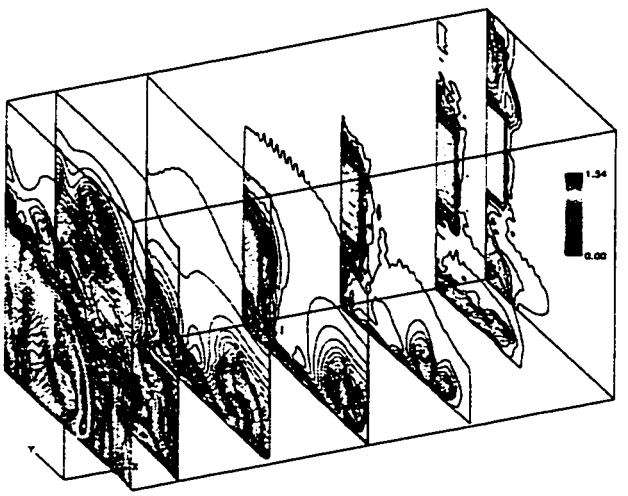

Figure 7.11: Contours of airflow speed on planes normal to x-direction

From the point of view of HVAC engineering, this room airflow configuration is a very poor "design" for cooling a room. This is not surprising, because the flow configuration was originally designed to simplify both experiments and simulations, rather than for human comfort inside the room. The poor cooling performance of the flow configuration is clearly identified by iso-surfaces exhibited in Figures 7.18 and 7.19. Both figures show that a large portion (almost a half) of the room space close to the ceiling and one corner ($X = 4.6\ m, Y = Z = 0\ m$) is virtually untouched by the inlet jet (a dead region). It appears that mounting vanes on the inlet to throw a portion of the inlet airflow transversely to the corner ($X = 4.6\ m, Y = Z = 0\ m$) will considerably improve the airflow and temperature distribution in the room.

The poor ventilation performance of the airflow configuration is exhibited in terms of streak lines in Figures 7.20 and 7.21. Figure 7.20 shows three streak lines for three seed particales situated near the outlet. All of these three streak lines trail back to

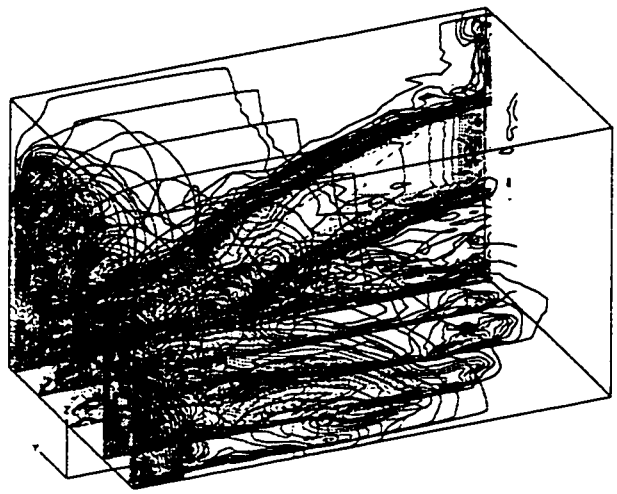

Figure 7.12: Contours of airflow speed on planes normal to y-direction

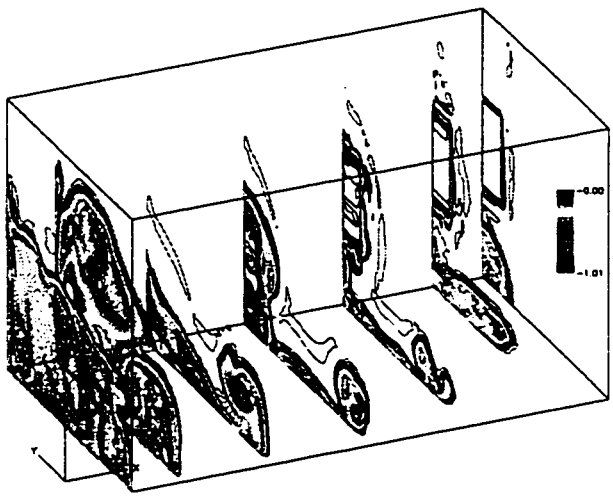

Figure 7.13: Contours of airflow temperature on planes normal to x-direction

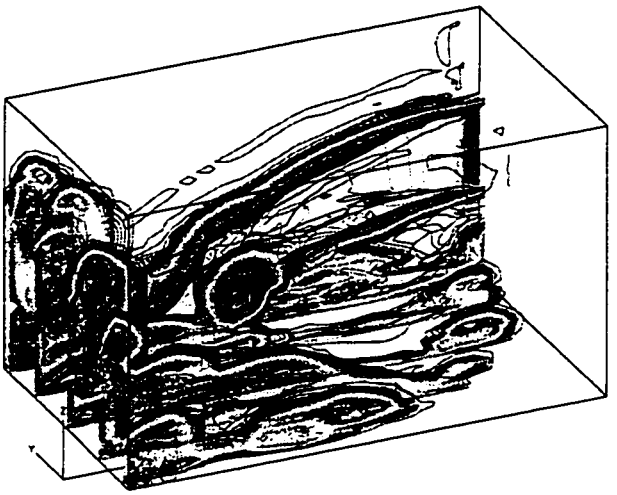

Figure 7.14: Contours of airflow temperature on planes normal to y-direction

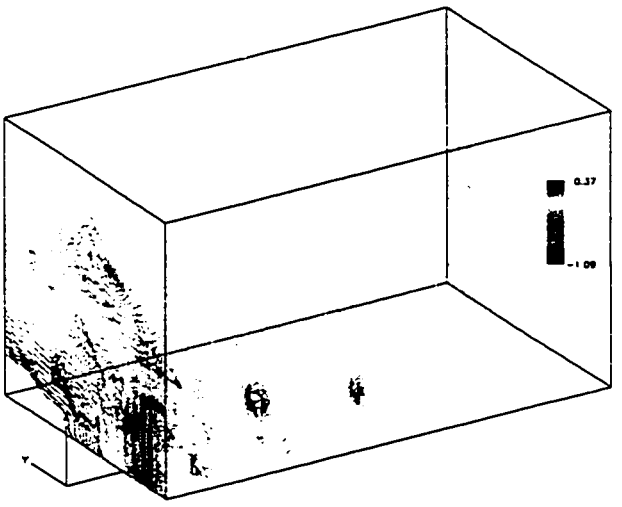

Figure 7.15: Contours of pressure on planes normal to x-direction

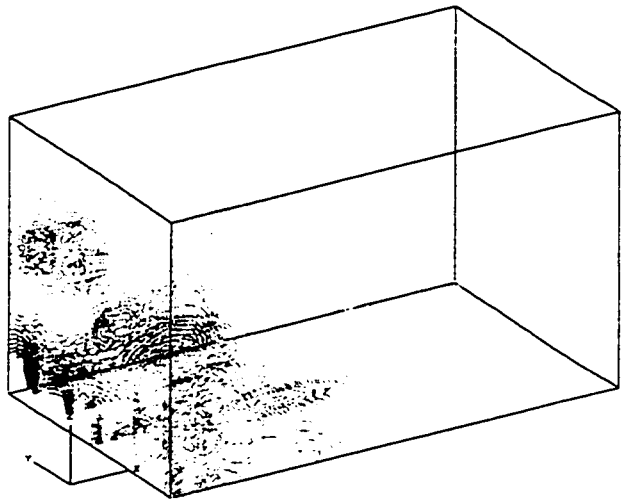

Figure 7.16: Contours of pressure on planes normal to y-direction

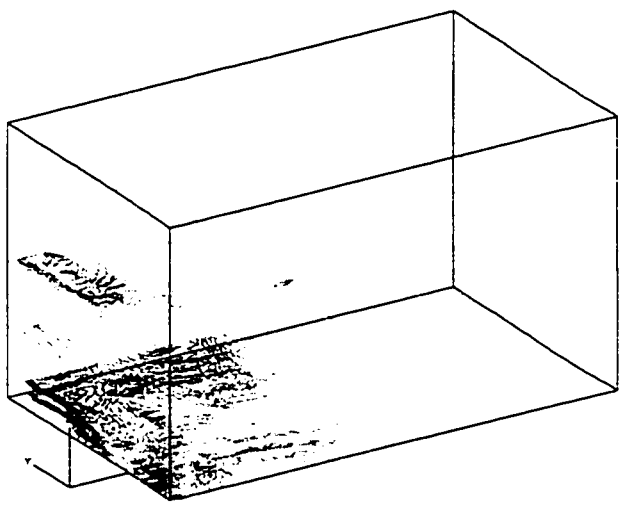

Figure 7.17: Contours of pressure on planes normal to z-direction

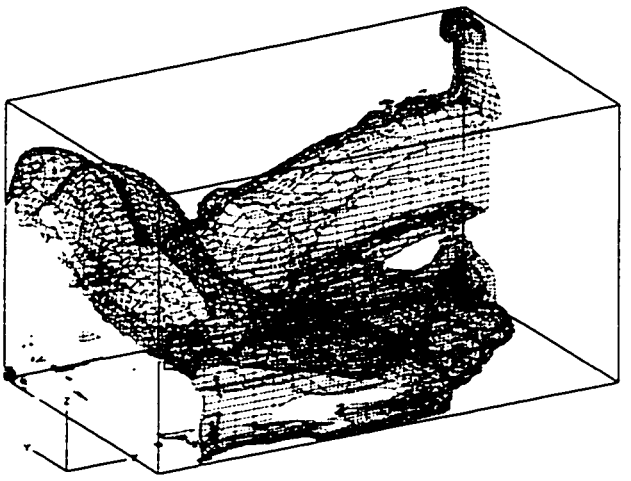

Figure 7.18: Iso-surface of airflow speed 0.1 (normalised)

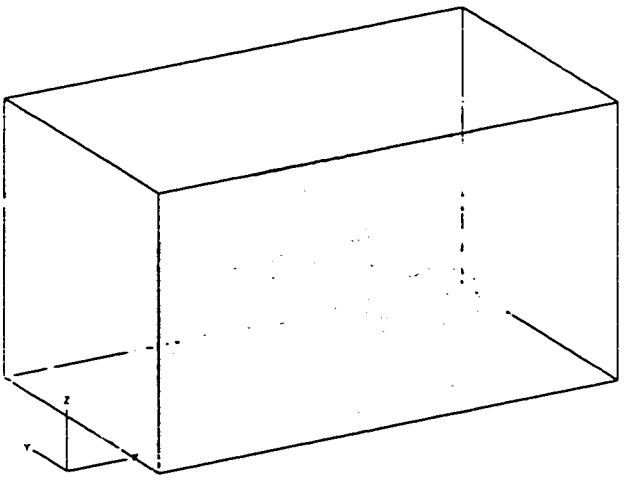

Figure 7.19: Iso-surface of airflow temperature −0.1 (normalised)

the inlet, which means that the inlet airflow does not mix effectively with the air inside the room. Figure 7.21 shows a streak line starting from a seed situated in the "dead region" of the room. After many circulation 'cycles', the streak line still can not reach the outlet. Streak lines approximate path lines of fluid particles for a quasi-steady flow. Thus, Figure 7.21 tells us that the room airflow configuration is inefficient at removing contaminants from the "dead region".

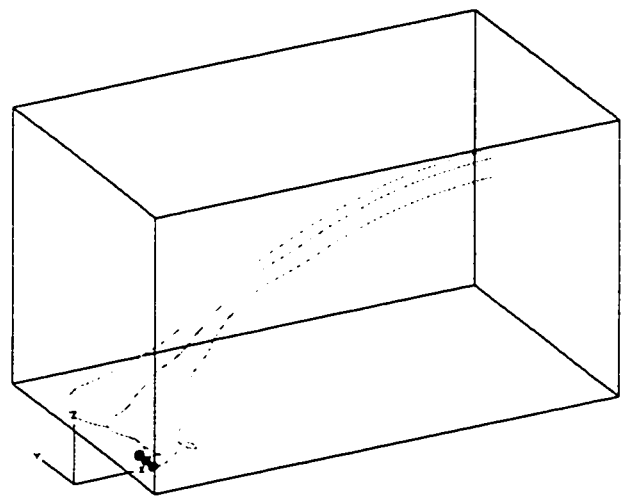

Figure 7.20: Streak lines ending at 3 seeds situated near outlet

The ranges of the values of each of the instantaneous fields of the SGS Reynolds stress tensor τ_{ij}, the SGS turbulent heat flux σ_j, and the eddy diffusivities α_j taken at the last time step of the simulation are presented in Table 7.2. In order to illustrate their distributions in the room, contours for two of these parameters, *i.e.* τ_{13} and α_1, are presented in Figures 7.22 through 7.27. It seems that the SGS scale turbulence is strong in regions close to the floor and opposite wall (the maximum value of α_1 occurs near the lower portion of the opposite wall), but relatively weak near the inlet and in the low-flow-speed regions. This may explain why the inlet jet has no significant expansion before hitting the floor.

Finally, let's compare the results of the present room airflow simulation with their

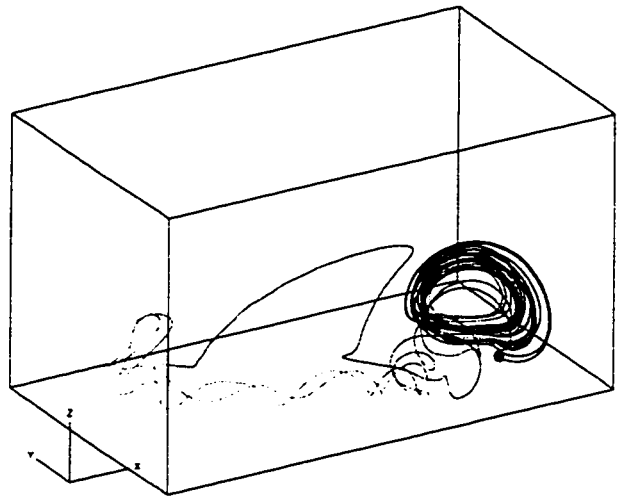

Figure 7.21: Streak lines starting from a seed situated in "dead region"

Table 7.2: Ranges of normalised values of SGS-related parameters (room airflow)

Parameter	Minimum	Maximum
τ_{11}	-8.312×10^{-1}	$0.\times10^{0}$
τ_{12}	-2.545×10^{-1}	1.351×10^{-1}
τ_{13}	-2.644×10^{-1}	1.567×10^{-1}
τ_{21}	-2.545×10^{-1}	1.351×10^{-1}
τ_{22}	-6.896×10^{-1}	$0.\times10^{0}$
τ_{23}	-1.027×10^{-1}	6.786×10^{-2}
τ_{31}	-2.644×10^{-1}	1.567×10^{-1}
τ_{32}	-1.027×10^{-1}	6.786×10^{-2}
τ_{33}	-4.555×10^{-1}	$0.\times10^{0}$
σ_1	-1.399×10^{-1}	1.542×10^{-1}
σ_2	-1.388×10^{-1}	9.927×10^{-2}
σ_3	-1.296×10^{-1}	8.122×10^{-2}
α_1	$0.\times10^{0}$	5.692×10^{2}
α_2	$0.\times10^{0}$	4.825×10^{2}
α_3	$0.\times10^{0}$	5.722×10^{2}

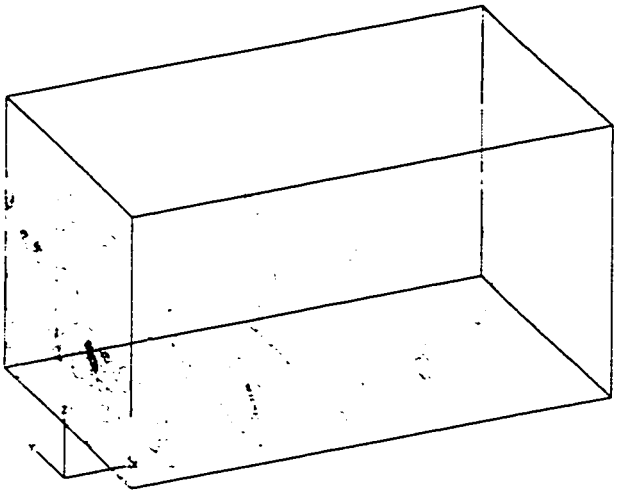

Figure 7.22: Contours of τ_{13} on planes normal to x-direction

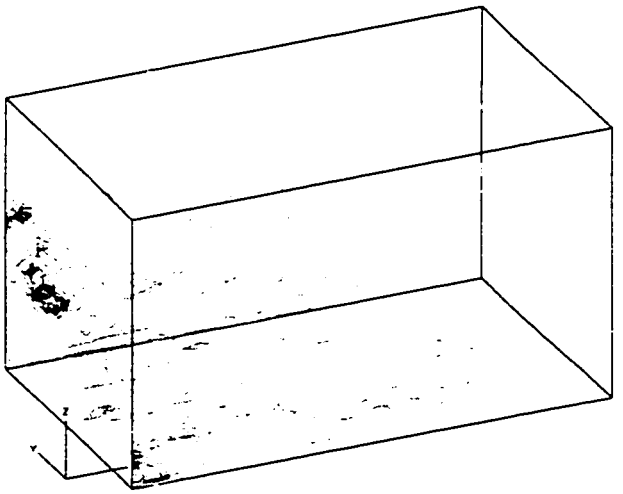

Figure 7.23: Contours of τ_{13} on planes normal to y-direction

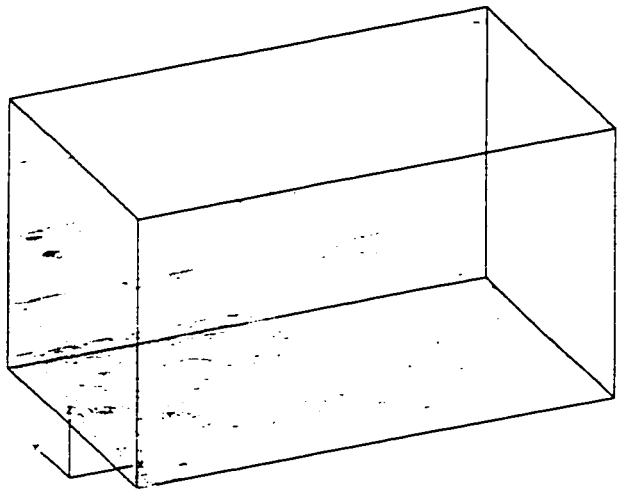

Figure 7.24: Contours of τ_{13} on planes normal to z-direction

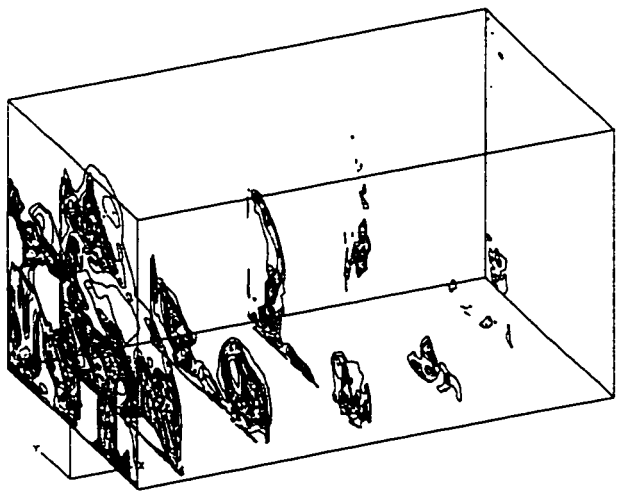

Figure 7.25: Contours of α_1 on planes normal to x-direction

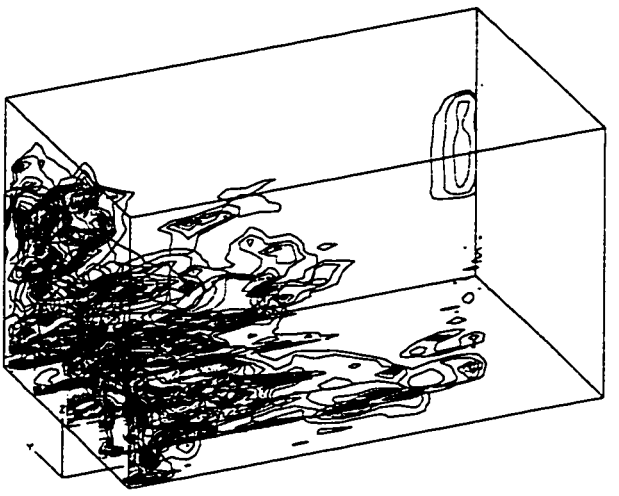

Figure 7.26: Contours of α_1 on planes normal to y-direction

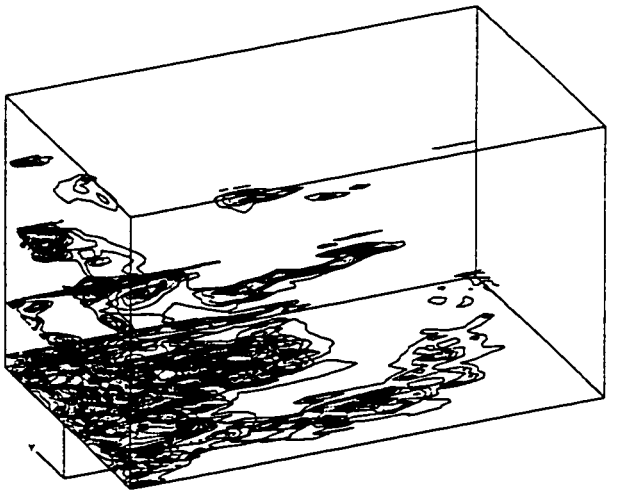

Figure 7.27: Contours of α_1 on planes normal to z-direction

counterparts from the experimental investigation of Weather & Spitler (1993). A gray-scale graph illustrating the distribution of the room airflow speed in the vertical inlet center plane is shown in Figure 7.28, which can be compared with a similar plot obtained from measurements shown in Figure 2-b of Weather & Spitler (1993). This figure has poor resolution, and is replotted in Figure 7.29. It is found that the present result closely matches that of the measurements. The maximum speed obtained from the measurements is 1.27 m/s (250 fpm) (Weather & Spitler, 1993) which is close to the maximum speed 1.32 m/s in the present simulation. The throw distance of the inlet jet (the horizontal distance from the inlet to the contact point with the floor) estimated from Figure 7.28 and that from Figure 7.29 are almost the same. The only identifiable difference between the two figures is that the present LES simulation predicted a high airflow speed region near the opposite wall, which the measurements do not confirm. One possible reason for this discrepency is that the vertically extended roller chain used to mount the spherical, heated thermistor air velocity transducers in Weather & Spitler's (1993) experiment hinder the accurate measurement of vertical air velocity near the opposite wall (see Spitler & Pederson, 1991). It is neccesary to remind us here that the "multiple solution" feature of room airflow may bring in some differences among results from different simulation/experiments, or even from different sampling times of a single simulation/experiment. Therefore, a part of the above presented discrepency might come from the "multiple solutions".

A similar comparison might be made between Figure 7.28 and its counterpart obtained from the simulation of Weather & Spitler (1993). However, Weather & Spitler's (1993) simulation results for the 30 ACH case are not realistic; as the authors themselves put it, comparison of their results with the measurements indicated neither qualitative nor quantitative agreement. The low temperature inlet jet in Weather & Spitler's (1993) simulation is rising rather than sinking in the room, which seems contrary to common sense.

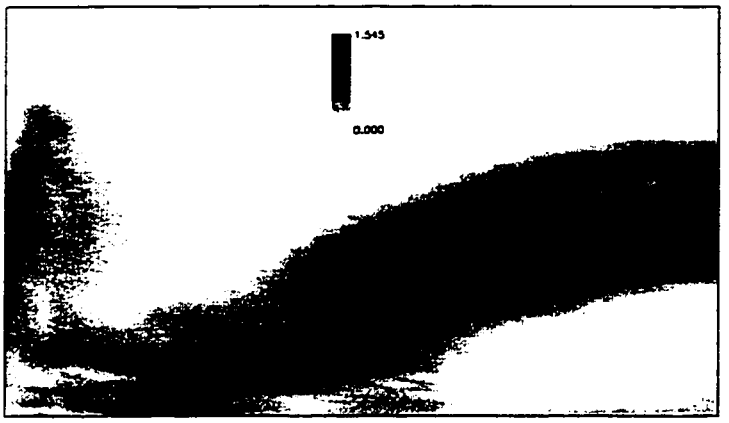

Figure 7.28: Grey-scale graph of airflow speed in vertical inlet centerplane

Figure 7.29: Figure 2-b in Weather & Spitler (1993)

7.5 Summary

Using a grid of $31 \times 61 \times 61$ cells, the VAT for turbulent flow simulation has been succesfully applied to predict the velocity and temperature fields in a 4.6 $m \times 2.7$ $m \times 2.7m$ room with a cooling inlet and wall-mounted cooling load. The final simulation results were presented using high-quality field display graphic software. Three-dimensionality of the resolvable fields and the SGS fluctuations of the flow were captured by the VAT, and displayed in terms of contour and vector plots. A comparison of one of the simulation results with its counterpart from Weather & Spitler's experiment shows good agreement.

Chapter 8

Conclusions

8.1 Summary

8.1.1 Historical Remarks

The original objective of the present research, which was set up five years ago by the supervisory committee of the author's Ph.D. program, was to apply the conventional LES method to room airflow predictions. Therefore, at the beginning of the research, the author assumed that the LES technique had been well developed, and focused most of the attention on the engineering application of this technique. However, during the process of the literature search and computer program development, many unexpected problems appeared.

Firstly, it was found that most existing numerical schemes were not suitable for

the LES technique. Therefore, it took about two years to develop a 3-D collocated scheme for the LES method. Rhie & Chow's (1983) scheme was first combined with the SIMPLE scheme. This hybrid scheme failed to obtain accurate results in the simulation of a 3-D laminar LDC flow. Then, the idea of the CPI method was proposed and implemented in a SIMPLE-like scheme in the simulation of a 3-D laminar LDC flow. The results were encouraging because they were much better than those obtained by Babu *et al.* (1993) with a finer grid, even though it was found later that the idea of the CPI scheme in the context of finite difference scheme had already been published by Deng *et al.* (1994). Further investigation of the collocated scheme based on the CPI scheme and SIMPLE showed that it did not work well in simulation of time-dependent flows, which means that it can not be applied in the LES. Therefore, a collocated scheme combining FSM and SIMPLE was proposed, and applied as a standard numerical tool for the VAT in the present study.

It took another two years to develop the VAT. At the beginning of the research, we planned to use Germano *et al.*'s (1991) dynamic SGS model to simulate room airflow. However, preliminary runs of the computer program showed no evidence of any fluctuation of the resolvable fields, which was, from the author's point of view, probably due to the coarse grid applied. To solve this problem, we tried to use the supercomputer resources accessible for us in Canada and USA. We were fortunate to be awarded 120 CPU hours in total on a Fujistu VPX-240 vector supercomputer by the HPCC in Calgary. However, resources of this supercomputer were still insufficient for a computer program in its developing stage. Large amounts of CPU time were required to test, debug, and revise the code. Additionally, it was found during the period of developing the computer program on the VPX-240 that vectorisation was the key to achieve high efficiency of computation, but to vectorise the code would take a large amount of time and effort. In the end, for practical reason, the LES model and code was extensively tested using our own workstations, which limited the size of problem which could be handled. Therefore, the focal point of the research switched from primarily application to a theoretical development with limited application.

8.1.2 Summary of Present Study

The finalised objective of the present study can be summarised as follows: to develop a new LES technique and apply it to the simulation of room airflow with the computer resources provided by a high performance workstation. The achievements of the present study are as follows.

Some deficiencies in previously developed techniques for the LES method, particularly those associated with the SGS modelling, have been identified. Prominent among these are: 1) the eddy diffusivity representation for the SGS effect of turbulence in most SGS models, which is not universally valid; 2) in conventional dynamic SGS modelling methods, often the method used to obtain the volume averaged fields on the TGS level from those on the SGS level does not discriminate real turbulent spatial fluctuation from non-fluctuating spatial inhomogeneity of the flow; and 3) Bardina's scale similarity SGS model dissipates little or no energy and is too crude in its derivation to justify the use of a constant coefficient.

In order to overcome these drawbacks, a new so called Volume Average Technique (VAT) for turbulent flow simulation has been proposed. The main features of the VAT can be summarised as follows:

1) The volume averaging approach instead of the more common filtering approach is employed to define solvable scale fields, so that coarse-graining in the LES and space discretization of the numerical scheme are achieved in a single procedure.

2) All components of the SGS Reynolds stress and SGS turbulent heat flux are modelled dynamically using the newly proposed Functional Scale Similarity (FSS) SGS model. The modelling coefficients of the FSS SGS model are determined dynamically, and non-fluctuating spatial inhomogeneity of the flow is removed by involving the time averaged fields in the modelling procedure. Therefore, the SGS model should be applicable to highly inhomogeneous and/or anisotropic turbulence as well as weak or multi-regime turbulent flows using a relatively coarse grid.

3) The so-called SGS turbulent diffusion is identified and modelled as a separate mechanism to that of the SGS turbulent flux represented by the SGS Reynolds stress and SGS turbulent heat flux. The SGS turbulent diffusion is defined in the coarse-graining procedure, and is responsible for most of the energy dissipation.

4) A new 3-D collocated scheme for the solution of viscous incompressible fluid flow, based on the SIMPLE and fractional-step method, is developed for the LES.

FORTRAN 77 codes (over 5000 lines) to realize numerically the VAT have been developed on two platforms, VMS-VAX mainframe and SUN workstation, at the University of Saskatchewan. The codes include a preprocessor called LES-PREPR, a mainline called LES-MAIN, a post-processor called LES-POSTPR, and various subroutines (LESLOCAL, LESSGS, LESFALSE, LESCPR, LESSOLVER) used by the mainline.

Benchmark tests of the VAT have been performed based on lid-driven and buoyancy-driven cavity flows. Firstly, 2-D and 3-D lid-driven cavity flows at $Re = 1000$ and $Re = 400$, and a 3-D buoyancy-driven cavity flow at $Ra = 10^6$, were simulated without using the SGS model. Since all of these flows are in the laminar regime, the objective of this simulation was to test the numerical schemes developed in the present study. Next, 3-D lid-driven and 3-D buoyancy-driven cavity turbulent flows at $Re = 10^4$ and $Ra = 10^{10}$ were simulated with the SGS model turned on. All results of the benchmark test simulations have been compared to their numerical or experimental counterparts found in the literature.

Finally, as an example of a practical calculation, the VAT has been applied to the LES of airflow in an enclosed air-conditioned room of size $4.6\ m \times 2.7\ m \times 2.7\ m$ with a wall-mounted cooling inlet and an opposing outlet. The results obtained have been compared with their counterparts from an experimental investigation of the same airflow reported by Weather & Spitler (1993).

8.2 Conclusions

In this section we present conclusions based on the LES technique development and simulation results obtained in the research. In order to be consistent with the content of the thesis, the presentation is subdivided into two parts, *i.e.* conclusions pertaining to the theory of the LES method and those pertaining to its application.

8.2.1 LES Theory

Based on the theoretical development of the present study, the following two conclusions are drawn:

1) Most of the problems associated with the conventional LES techniques have been either solved or partially solved in the VAT proposed by the present study. They are:

- The coarse-graining of instantaneous fields in the LES and the solution domain discretization of the FV scheme are combined as a single procedure in the VAT, so that some inconsistencies of LES methods based on the filtering approach are avoided.
- The SGS flux and SGS diffusion are distinguished and modelled separately in the VAT. The latter represents most of energy dissipation that Bardina *et al.*'s (1980) scale similarity SGS model failed to capture.
- The VAT totally gives up the eddy viscosity hypothesis. It dynamically models the full-component SGS Reynolds stress and turbulent heat flux, and the SGS turbulent diffusion as well. Therefore, it is appropriate for many complex flows of engineering and scientific significance.
- The problem of confusing turbulent fluctuation with spatial inhomogeneity of

fields in the conventional dynamic SGS modelling methods has been solved in the VAT. It has been shown that the VAT allows using a relatively coarse grid, and therefore alleviates the problem of memory shortage in simulation.

- The contradiction between physical instability of a turbulent flow and numerical instability is partially solved (but needs further research) by using a special "clipping" algorithm in the VAT.
- The characteristic length scales of the LES are calculated based on the length scales of control volume surfaces in the VAT to account for the anisotropic features of volume averages.

Preliminary benchmark tests of the VAT show that it performs well in capturing large scale time fluctuations of resolvable fields and predicting their time-averaged values.

2) The collocated scheme developed in the present study plays an important role in the VAT. The accuracy and efficiency of this 3-D incompressible scheme has been conclusively demonstrated. This scheme can be applied to a wide range of incompressible or slightly compressible flows occurring in natural science and engineering.

8.2.2 Applications

Another three conclusions can be drawn based on benchmark simulations and a real room airflow simulation carried out in the present study. They are:

1) From the point of view of application, the most important advantage of the VAT is that it can be applied to perform a real LES with a relatively coarse grid. A direct consequence of this, of course, is considerable saving of computer memory for the LES, which greatly increases the feasibility of extending the LES method to commercial applications.

2) Compared with most conventional LES techniques, the VAT requires more time steps (iterations) to complete a simulation. This is due to the use of time averages of the resolvable flow fields in the FSS SGS model, which are accurate only when the flow under consideration is fully developed. However, this does not necessarily mean that the use of the VAT needs more CPU time to complete a simulation, because the VAT's feature of being applicable with a relatively coarser grid can save a large amount of CPU time in simulation.

3) With the VAT developed, it will soon (perhaps in five years) be possible to use the LES method to simulate a real flow of engineering interest with the computer resource provided by a workstation. It can be estimated based on the room airflow simulation carried out in the present study that a grid of $100 \times 100 \times 100$ cells, which is approximately 8 times finer than that employed for the room airflow simulation, can satisfy the grid requirement of the LES of many engineering related flows of moderate complexity. The memory requirement corresponding to this grid is approximately 400 MB; a SUN-ULTRA workstation can handle a maximum of 662 MB (virtual) memory. The only worry about the LES of a flow in a workstation is the low CPU speed, which means that a simulation may take weeks to complete. However, the author believe that the CPU speed of workstations will quickly increase in the near future. Thus, the running time required for a complete LES will soon decrease to something on the order of one week, which is acceptable for many engineering applications.

Finally, based on the author's experience accumulated during the numerical simulations carried out in the present study, the following two conclusions can be drawn:

1) Since turbulent flows are strongly convection dominant, their simulation results are very sensitive to the initial flow conditions applied. Different initial flow conditions may lead to different final results. This is especially the case for flows with "dead regions" in the solution domain, where the flow quantities have no significant transport with the outer boundaries, and the flow pattern inside is strongly affected by the initial condition. This is actually one manifestation of the multiple solution

phenomenon described in section 1.3.

2) If the number of control volumes involved in a grid system for LES is doubled, the computing effort required to finish the LES is far more than doubled. A further doubling of the effort is necessary to account for a half time step decrease for satisfying the CFL condition, and another doubling of the effort is necessary to account for the additional iterations required in the ADLGS solver. Thus, increasing the number of control volumes by a factor of two can lead to an increase of computing effort by a factor of eight. Therefore, unnecessary grid refinement should be avoided in the LES practice.

8.3 Contributions

The contributions of the present study broadly relate to the technique and its application. It should be noted that the assessment of the contributions of the present study in this section are based on the author's knowledge of previous work in the area of the LES, which may be incomplete.

Let's first consider the contributions related to the VAT. One of the most important contributions in this regard is the development of the FSS SGS model. The author considers what follows to be unique features of the model: 1) removing flow inhomogeneity by subtracting from the solvable fields their time averaged values; 2) dynamic determination of the modelling coefficients using a postulated functional distribution of the auto-correlation components of the SGS Reynolds stress or that of the SGS temperature fluctuation; 3) anisotropic definition of the characteristic width of the volume average based on the surface length scales of the control volume; and 4) consideration in the model of the effect of the time step and that of time averaging the solvable fields via the concept of the dynamic length scale range of the model.

Another important contribution associated with the VAT is the identification of

the SGS turbulent diffusion as a different transport enhancement mechanism than the SGS turbulent flux. The idea is innovative, and the SGS turbulent diffusion model developed in the present study is far different from any previously developed eddy diffusivity SGS models.

The 3-D collocated scheme developed for the VAT in the present study has some unique features. For laminar flows, the scheme achieves surprisingly accurate results compared to those from other numerical simulations. The fractional-step handling of the velocity field components in the context of a SIMPLE-like solution strategy on a non-staggered gird system is a contribution of the present study.

As to the contributions related to applications, the successful LES of a 3-D buoyancy-drive cavity flow at Rayleigh number of $Ra = 10^{10}$ achieved in the present study is significant; no such simulation has been reported thus far. The LES of the 3-D non-isothermal room airflow using the computer resource provided by a workstation in the present study is also unprecedented.

8.4 Future Work

As a turbulent flow simulation technique, the VAT was first proposed in the present study. Due to time limitation of the Ph.D. program, only some preliminary benchmark tests on this technique have been performed thus far. Therefore, immediate future work should consider testing the technique by simulating benchmark flows other than cavity turbulence. The most suitable flows for such benchmark tests are channel and duct flows, both of which have been investigated thoroughly using both experimental and numerical methods for more than half a century. Some features of the flows have been well understood, *e.g.* the log-law velocity profile in near-wall regions which is an ideal benchmark to test the performance of the VAT in simulating wall damping of the flow. A unique feature of channel or duct flows is that almost

all the turbulence is wall-generated, thus the length scales of the turbulence near the walls of channel or duct flows are extremely small. A related challenge is that one should use a very fine grid in order to capture features of the near wall turbulence. It is therefore of great significance to determine if the problem associated with the fine grid requirement can be even partially alleviated by using the VAT in the LES of channel or duct flows.

An assumption on which the VAT is based is that the turbulent flow under consideration is statistically stationary, so that the ensemble averages of the instantaneous flow fields can be substituted by their time averaged counterparts in the simulation. This assumption will cause no problem if the frequency of temporal change of the flow fields is several orders of magnitude lower than frequencies of the turbulent fluctuations. Otherwise, a specific algorithm should be designed to eliminate the effect of the flow unsteadiness from the time averages of the fields, possibly in a similar way to what we have done in the present study in eliminating the effect of flow inhomogeneity from volume averages of the flow fields.

Viewing the turbulent diffusion or the SGS turbulent diffusion as a different transport enhancement mechanism than the SGS turbulent flux is a new approach proposed in the present study. Although the fact that 1) the rationale is based on an analogy to molecular diffusion and 2) reasonable simulation results were obtained both support the concept, further studies, both numerical and experimental, on this new concept are recommended. Additionally, the author is personally not very satisfied with the "clipping" algorithm designed in the VAT to avoid numerical divergence during simulation. Further studies may be carried out to improve it or to design a new one which is more "reasonable".

Extension of the VAT to orthogonal coordinate systems other than the Cartesian system, and to curvilinear coordinate systems is another project for future work. Doing this will significantly broaden the application area of the VAT, because more complex solution domains can be handled by general orthogonal coordinate systems

or curvilinear coordinate systems. Most of the tasks in this regard are routine, but will nevertheless complicate the solution procedures. However, the extension of the VAT to the cylindrical system is relatively simple and can be tried first.

As a long term future work, one may consider the extension of the VAT to compressible flows and furthermore to flows with combustion or chemical reactions. The author is personally interested in the LES of flows in the combustion chamber of a power plant boiler furnace. The success of such a simulation can provide guidance of how to locate burners correctly around the combustion chamber.

References

Aldama, AA. (1990). Filtering Techniques for Turbulent Flow Simulation. *Lecture Notes in Engineering*, **56**, Springer-Verlag.

Akselvoll, K. & Moin, P. (1996). Large-Eddy Simulation of Turbulent Confined Coannular Jets *J. Fluid Mech.*, **315**, 387-411.

Antonopoulos-Domis (1981). Large-Eddy Simulation of Passive Scalar in Isotropic Turbulence. *J. Fluid Mech.*, **104**, 55-79.

Armfield, SW. (1991). Finite Difference Solutions of The Navier-Stokes Equations on Staggered and Non-Staggered Grids. *Comp. Fluids*, **20**, 1-17.

Babajimopoulos, C. & Bedford, K. (1980). Formulating Lake Models which Preserve Spectral Statistics. *J. Hydr. Div.*, **106**, 1-19.

Baetke, F., Werner, H., & Wengle, H. (1990). Numerical Simulation of Turbulent Flow over Surface-Mounted Obstacles with Sharp Edges and Corners. *J. Wind Engrg. Industrial Aerodynamics*, **35**, 129-147.

Barakos, G., Mitsoulis, E., & Assimacopolos, D. (1994). Natural Convection Flow in a Square Cavity Revisited: Laminar and Turbulent Models with Wall Functions. *Int. J. Numer. Meth. Fluids*, **18**, 695-719.

Bardina, J., Ferziger, JH., & Reynolds, WC. (1980). Improved Subgrid Models for Large Eddy Simulation. AIAA Paper, No.80-1358.

Babu, V. & Korpela, SA. (1994). Numerical Study of Three-Dimensional Navier-Stokes Equations. *Comp. Fluids*, **23**, 675-691.

Bardina, J., Ferziger, JH., & Reynolds, WC. (1983). Improved Turbulence Models Based on Large Eddy Simulation of Homogeneous, Incompressible Turbulent Flows. *Rep. TF-19*, Dept. of Mech. Engrg., Stanford University, Stanford, CA.

Barsamian, HR. & Hassan, YA. (1994). Modified Subgrid Scale Model for Large Eddy Simulation of Tube Bundle. *Flow-Induced Vibration, Pressure Vessels and Piping Division*, **273**, ASME, New York, NY, USA, 283-288.

Bedford, KW. & Dakhoul, Y. (1982). Applying LES Turbulence Modelling to Open Channel Flow. *Proc. of the 1982 ASCE Hydr. Division Speciality Conf.*, Jackson, MI.

Boersma, BJ. & Nieuwstadt, FTM. (1996). Large-Eddy Simulation of Turbulent Flow in A Curved Pipe. *J. Fluids Engrg., Trans. of ASME*, **118**, 248-245.

Bedford, K. & Dakhol Y. (1982). Applying LES Turbulence Modelling to Open Channel Flow. *Proc. of the 1982 ASCE Hydr. Div. Speciality Conf.*, Jackson, MI.

Bilski, SM., Lloyd, JR., & Yang, KT. (1986). An Experimental Investigation of the Laminar Natural Convection Velocity in Square Partitioned Enclosures. *Proc. 8th Int. Heat Transfer Conf.*, **4**, 1513-1518.

Boris, JP., Grinstein, FF., Oran, ES., & Kolbe, RL. (1992). New Insight into Large Eddy Simulation. *Fluid Dynamic Res.*, **10**, 199-228.

Breuer M. & Rodi W. (1994). Large-Eddy Simulation of Turbulent Flow Through Straight and Curved Ducts. *ERCOFTAC Bull*, **22**, 26-29.

Bruneau, CH. & Jouron, C. (1990). An Efficient Scheme for Solving Steady Incompressible Navier-Stokes Equations. *J. Comp. Phys.*, **89**, 389-.

Cain, AB., Reynolds, WC., & Ferziger, JH. (1981). A Three-Dimensional Simulation of Transition and Early Turbulence in A Time-Developing Mixing Layer. *Rep. TF-14*, Dept. of Mech. Engrg., Stanford University, Stanford, CA.

Cheesewright, R & Ziai, S. (1986). Distribution of Temperature and Local Heat Transfer in Turbulent Natural Convection. *Proc. 8th Int. Heat Transfer Conf.*, San Francisco, 1465-1470.

Chen, CJ. & Chen, HC. (1984). Finite-Analytic Numerical Solution for Unsteady Two-Dimensional Navier-Stokes Equations. *J. Comp. Phys.*, **53**, 209-.

Chen, Q. & Jiang Z. (1992). Significant Questions in Predicting Room Air Motion. *ASHRAE Transactions*, **98**, Part 1, 929-938.

Chen, Q. (1996). Prediction of Room Air Motion by Reynolds-Stress Models. *Building and Environment*, **31**, 233-244.

Chorin, AJ. (1968). Numerical Solution of The Navier-Stokes Equation. Math. Comp., **22**, 745-762.

Clark, RA., Ferziger, JH., & Reynolds, WC. (1979). Evaluation of Subgrid-Scale Models Using an Accurately Simulated Turbulent Flow. *J. Fluid Mech.*, **91**, 1-16.

Comte-Bellot, G & Corrsin, S. (1971). Simple Eulerian Time Correlation of Full- and Narrow-band Velocity Signals in Grid-Generated "Isotropic" Turbulence. *J. Fluid Mech.*, **48**, 273-337.

Dai, Y., Kobayashi, T., & Taniguchi, N. (1994). Large Eddy Simulation of Plane Turbulent Jet Flow Using a New Outflow Velocity Boundary Condition. *JSME Int. J. Series B: Fluids and Thermal Engrg.*, **37**, 242-253.

Dakhoul, YM. (1983). Improved Averaging Method for Turbulent Flow Simulation. Ph.D. Thesis, The Ohio State University.

Dakhoul, YM. & Bedford, KW. (1986). Improved Averaging Method For Turbulent Flow Simulation. Part I: Theoretical Development and Application to Burgers Transport. *Int. J. Numerical Methods in Fluids*, **6**, 49-64.

Davidson, L. (1997). LES of Recirculation Flow without Any Homogeneous Direction: A Dynamic One-Equation Subgrid Model. *2nd Int. Symposium on Turbulence, Heat and Mass Transfer*, Delf University Press. 481-491.

Deardoff, JW. (1970). A Numerical Study of Three-Dimensional Turbulent Channel Flow at Large Reynolds Numbers. *J. Fluid Mech.*, **41**, 453-480.

Deardoff, JW. (1971). On the Magnitude of The Subgrid Scale Eddy Coefficient. J. Comput. Phys., **7**, 120-133.

Deardoff, JW. (1973). Simulation of Turbulent Channel Flow. *J. Fluids Engrg*, **95**, 429-.

Denaro, FM. (1996). Towards A New Model-Free Simulation of High-Reynolds-Flows: Local Average Direct Numerical Simulation. *Int. J. Numerical Methods in Fluids*, **23**, 125-142.

Deng, GB., Piquet, J., Queutey, P., & Visonneau, M. (1994). Incompressible Flow Calculations with a Consistent Physical Interpolation Finite Volume Approach. *Computer & Fluids*, **23**, 1029-1047.

Eggels, JGM. (1996). Direct and Large-Eddy Simulation of Turbulent Fluid Flow Using The lattice-Boltzmann Scheme. *Int. J. Heat & Mass Transfer*, **39**, 307-323.

Ferziger, JH. (1977). Large Eddy Numerical Simulation of Turbulent Flow. *AIAA Journal*, **15**, 1261-.

Ferziger, JH. (1980). Homogeneous Turbulent Flow: A Review and Evaluation. *1980-81 Stanford-AFOSR-HTTM conf. on Complex Turbulent Flows*, Dept. of Mech. Engrg., Stanford University, Stanford, CA.

Ferziger, JH. (1983). High Level Simulation of Turbulent Flows. *Computational Methods for Turbulent, Transonic, and Viscous Dlows*, Springer-Verlag, 93-182.

Ferziger, JH. (1993). Subgrid-Scale Modelling. *Large Eddy Simulation of Complex Engineering and Geophysical Flows*, Cambridge University Press, 37-54.

Frank, W. & Mauch, H. (1993). Large-Eddy-Simulation of The Flow Around Building Models. *J. Wind Engrg and Industrial Aerodynamics*, **46-47**, 213-218.

Fusegi, T., Hyun, JM., Kuwahara, K., & Farouk, B. (1991). A Numerical Study of Three-Dimensional Natural Convection in a Differentially Heated Cubical Enclosure. *Int. J. Heat Transfer*, **34**, 1543-1557.

Gan, G. (1995). Evaluation of Room Air Distribution Systems Using Computational Fluid Dynamics. *Energy & Buildings*, **23**, 83-93.

Germano, M., Piomelli, U., Moin, P., & Cabot, WH. (1991). A Dynamic Subgrid-scale Eddy Viscosity Model. *Phys. Fluids A*, **3**, 1760-1765.

Ghia, U., Ghia, KN., & Shin, CT. (1982). High-Re Solutions for Incompressible Flow Using the Navier-Stokes Equations and Multigrid method. *J. Comp. Phys.*, **48**, 387-.

Goutorbe, T., Laurence, D., Maupu, V. (1994). A Priori Test of A Subgrid Scale Stress Tensor Model Including Anisotropy and Backscatter Effects. *Direct and Large Eddy Simulation I*, Kluwer Academic Publishers, 121-131.

Grotzbach, G. (1977). Direkte Numerische Simulation Turbulenter Geschwindigkeits, Druck und Temperaturfelder bei Kanalstromungen. *Dissertation, Univ. of Karlsrube.*

Grotzbach, G. (1978). Direct Numerical Simulation of Secondary Currents in Turbulent Channel Flows. *Lecture Notes in Physics*, **76**, Springer-Verlag, 308-319.

Grotzbach, G. (1979). Numerical Investigation of Radial Mixing Capability in Strongly Buoyancy-Influenced Vertical Turbulent Channel Flows. *Nucl. Engrg. Design*, **54**, 49-66.

Grotzbach, G. (1986). Direct Numerical and Large Eddy Simulation of Turbulent Channel Flows. *Handbook of Fluid Mechanics*, Gulf Pub. Co. Book Division, 1337-1389.

Hanjalic, K. & Vasic, S. (1993). Computation of Turbulent Natural Convection in Rectangular Enclosures with an Algebraic Flux Model. *Int. J. Heat Mass Transfer*, **36**, 3603-3624.

Harlow, FH. & Nakayama, PI. (1968). Transport of Turbulence Energy Decay Rate. LA Report No.3854.

Hassan, YA., Bagwell, TG., & Steininger, DA. (1991). Large Eddy Simulation of Fluctuating Forces on A Square Pitched Tube Array and Comparison with Experiment. *Pressure Vessels and Piping Division*, **189**. ASME, New York, NY, USA, 45-49.

Hassan, YA., Lee, S., Steininger, DA., & Srikantiah, G. (1993). Large Eddy Turbulent Simulation of Three Dimensional Bundle Flows. *Steam Generator Thermal Hydraulics, Heat Transfer Division*, **251** ASME, New York, NY, USA, 43-47.

Hassan, YA. & Barsamian, HR. (1994). Velocity Field Predictions Across Flow Bundles by Large Eddy Simulation. *Thermal Hydraulics of Advanced Steam Generators and Heat Exchangers, Nuclear Engineering Division***15**, ASME, New York, NY, USA, 29-33.

Hawkin, AN., Hosni, MH., & Jones, BW. (1995). Comparison of Room Air Motion in A Full Size Test Room Using Different Diffusers and Operating Conditions. *ASHRAE Transactions*, **101**, Part 2, 81-100.

He, J. & Song, Charles CS. (1995). Wind Load Computation of Building Complex with Large Eddy Simulation. *Restructuring: America and Beyond Structures*

Congress, ASCE, New York, NY, USA, 1431-1434.

Hinze, JO. (1975). *Turbulence* (2nd edn.) McGraw-Hill, New York.

Hoogendoorn, CJ., Opstelten, IJ., & Dol, HS. (1996). Turbulent Natural Convection in A Cubical Cavity. *Proc. Turbulent Heat Transfer Conference*, San Diego.

Herring, JR. & Kerr, RM. (1993). Some Contributions of Two-Point Closure to Large Eddy Simulation. *Large Eddy Simulation of Complex Engineering and Geophysical Flows*, Cambridge University Press, 80-104.

Horiuti, K. & Yoshizawa, A. (1985). Large Eddy Simulation of Turbulent Channel Flow by 1-equation Model. *Finite Approximations in Fluid Mechanics*, Vieweg, 119-134.

Jordan, SA. (1994). Use of The Large-Eddy Simulation Dynamic Model for Turbulent Shear-Driven Cavity Flows. *Boundary Layer and Free Shear Flows ASME, FED*, **184**, New York, NY, USA., 141-150.

Jordan, SA. & Ragab, SA. (1994). Large-eddy Simulation of the Near Wake of A Circular Cylinder. *Turbulence in Complex Flows American Society of Mechanical Engineers, Fluids Engineering Division*, **203**, ASME, 1-9.

Joshi, DS., Vanka, SP., & Tafti, D.K. (1994). Large Eddy Simulation of The Wake of A Normal Flat Plate. *Boundary Layer and Free Shear Flows, Fluids Engineering Division*, **184**, ASME, 231-242.

Jouini, DB., Said, MN., Plett, EG. (1994). Measurements of Room Air Distribution in A Ventilated Office Environment. *Building & Environment*, **29**, 511-521.

Kajishima, T. & Miyake, Y. (1992a). Large Eddy Simulation of A Turbulent Channel Flow with A Periodic Pressure Gradient. *JSME Int. J., Series 2: Fluids Engrg.*, **35**, 23-28.

Kajishima & T., Miyake, Y. (1992b). Discussion on Eddy Viscosity Models on the Basis of The Large Eddy Simulation of Turbulent Flow in A Square Duct. *Comp. Fluids*, **21**, 151-161.

Kaltenbach, HJ., Gerz, T., & Schumann, U. (1994). Large-eddy Simulation of Homogeneous Turbulence and Diffusion in Stably Stratified Shear Flow. *J. Fluid Mech.*, **280**, 1-40.

Kato, S., Murakami, S., & Kondo, Y. (1994). Numerical Simulation of Two-Dimensional Room Airflow with and Without Buoyancy by Means of ASM. *ASHRAE Transactions*, **100**, Part 1.

Kawamura, T. & Kuwahara, K. (1984). Computation of High Reynolds Number Flow around A Circular Cylinder with Surface Roughness. *AIAA Paper*, No.84-0340.

Kin, HT. & Moin, P. (1979). Large Eddy Simulation of Turbulent Channel Flow. *AGARD Symposium on Turbulent Boundary Layers*, The Hague.

Kline, SJ., Reynolds, WC., Schraub, FA., & Runstadler, PW. (1967). The Structure of Turbulent Boundary Layers. *J. Fluid Mech.*, **30**, 741-773.

Kolmogoroff, AN. (1949). On the disintegration of drops in turbulent flow. Doklady Akad. Nauk. S.S.S.R., **66**, 825-.

Ku, HC., Hirsh, RS., & Taylor, TD. (1987). A Pseudospectral Method for Solution of the Three-Dimensional Incompressible Navier-Stokes Equations. *J. Comp. Phys.*, **70**, 439-462.

Kwak, D., Reynolds, WC., & Ferziger, JH. (1975). Three-Dimensional Time Dependent Computation of Turbulent Flow. *Rep. TF-5*, Dept. of Mech. Engrg., Stanford University, Stanford, CA.

Ladyzhenskaya, OA. (1969). *The Mathematical Theory of Viscous Incompressible Flow*, Gordon and Breach, New York.

Launder, BE. & Spalding, DB. (1974). The Numerical Computation of Turbulent Flows. *Comp. Method in Applied Mechanics and Energy*, **3**, 268-289.

Leonard, A. (1974). Energy Cascade in Large Eddy Simulations of Turbulent Fluid Flows. *Adv. in Geophysics*, **18A**, 237-.

Lesieur, M., Metais, O., Normand, X., & Silveira-Neto, A. (1993). Spectral Large Eddy Simulation of Turbulent Shear Flows. *Large Eddy Simulation of Complex Engineering and Geophysical Flows*, Cambridge University Press, 179-192.

Lesieur, M. & Metais, O. (1996). New Trends in Large-Eddy Simulations of Turbulence. *Ann. Rev. Fluid Mech.*, **28**, 45-82.

Lesieur, M. (1996). Large-Eddy Simulations of Shear Layers. *Exp. Thermal Fluid Sci.*, **12**, 197-208.

Leslie, DC. & Quarini, GL. (1979). The Application of Turbulence Theory to The Formulation of Subgrid Modelling Procedures. *J. Fluid Mech.*, **91**, 65-91.

Leslie, DC. (1982). Simulation Method for Turbulent Flows. *Numerical Methods for Dluid Dynamics*. Academic Press, London, 63-80.

Lilly DK. (1992). A Proposed Modification of The Germano Subgrid-Scale Closure Method. *Phys. Fluids A*, **4**, 633-635.

Love, MD. & Leslie, DC. (1977). Studies of Subgrid Modelling with Classical Closures and Burger's Equation. Proc. Symp. Turbulent Shear Flows, PA.

Love, MD. (1980). Subgrid Modelling Studies with Burger's Equation. *J. Fluid Mech.*, **100**, 87-100.

Lui, S., Meneveau C., & Katz J. (1994). On the Properties of similarity Subgrid-Scale Models as Deduced from Measurements in Turbulent Jet. *J. Fluid Mech.*, **275**, 83-119.

Lund, TS., Ghosal, S., Moin, P. (1993). Numerical Experiments with Highly-Variable Eddy Viscosity Models. *Engineering Applications to Large Eddy Simulation*, New York, ASME, 7-11.

Lund, TS. & Moin, P. (1997). Large-Eddy Simulation of A Concave Wall Boundary Layer. *Int. J. Heat and Fluid Flow*, **17**, 290-295.

Mansour, NN., Ferziger, JH., & Moin, P., Reynolds, WC. (1978). Large-Eddy Simulation of A Turbulent Mixing Layer. *Rep. TF-11*, Dept. of Mech. Engrg., Stanford University, Stanford, CA.

Mansour, NN., Moin, P., Reynolds, WC., & Ferziger, JH. (1979). Improved Methods for Large Eddy Simulations of Turbulence. *Turbulent Shear Flows I*, Springer-Verlag, 386-401.

Majumdar, S. (1988). Role of Underrelaxation in Momentum Interpolation for Calculation of Flow with Nonstaggered Grids. *Numerical Heat Transfer*, **13**, 125-.

McGrattan, KB., Baum, HR., Rehm, RG. (1996). Numerical Simulation of Smoke Plumes from Large Oil Fires. *Atmospheric Environment*, **30**, 4125-4136.

McMillan, OJ., Ferziger, JH., & Rogallo, RS. (1980). Test of New Subgrid Scale Models in Strained Turbulence. AIAA paper No.80-1339.

Meneveau, C., Lund, TS., & Cabot, W. (1994). A Lagrangian dynamic Subgrid-Scale Model of Turbulence. Proc. of the Summer Program 1994, Centre for Turbulence Res., 271-299.

Menon, S., Yeung, P., & Kim, W. (1996). Effect of subgrid models on the computed interscale energy transfer in isotropic turbulence. *Comp. Fluids*, **25**, 165-180.

Meszaros, E, Mersich, I., & Szentimrey, T. (1987). Large Eddy Simulation of Buoyant and Non-Buoyant Plume Dispersion in The Atmospheric Boundary Layer. *Atmospheric Environment*, **21**, 2573-2587.

Miller, TF. & Schmidt, FW. (1988). Use of a Pressure-Weighted Interpolation Method for The Solution of Incompressible Navier-Stokes Equations on a Non-staggered Grid System. *Numerical Heat Transfer*, **14**, 213-233.

Milane, RE., & Nourazar, S. (1995). On The Turbulent Diffusion Velocity in Mixing Layer Simulated Using The Vortex Method and The Subgrid Scale Vorticity Model. *Mech. Res. Communications*, **22**, 327-333.

Moin, P., Reynolds, WC., & Ferziger, JH. (1978). Large Eddy Simulation of an Incompressible Turbulent Channel Flow. *Rep. TF-12*, Dept. of Mech. Engrg., Stanford University, Stanford, CA.

Moin, P. & Kim J. (1982). Numerical Investigation of Turbulent Channel Flow. *J. Fluid Mech.*, **118**, 341-377.

Mochida, A., Murakami, S., Shoji, M., & Ishida, Y. (1993). Numerical Simulation of Flowfield around Texas Tech Building by Large Eddy Simulation. *J. Wind Engrg. Industrial Aerodynamics*, **46-47**, 455-460.

Murakami, S., Hibi, K., & Mochida, A. (1986). Visualization of Computer-Generated Turbulent Flowfield around Cubic Model. *Conference of Fluid Control & Measurements*, **2**, Pergamon Press, Oxford, Engl & New York, USA, 739-744.

Murakami, S., Mochida, A., & Hibi, K. (1987). Three-Dimensional Numerical Simulation of Air Flow around A Cubic Model by Means of Larege Eddy Simulation. *J. Wind Engrg. Industrial Aerodynamics*, **25**, 291-305.

Murakami, S.& Mochida, A. (1995). Turbulent Vortex Shedding Flow Fast 2D Square Cylinder Predicted by CFD. *J. Wind Engrg. Industrial Aerodynamics*, **54-55**, 191-211.

Murakami, S., Mochida, A., & Hayashi, Y. (1995). Validation of Turbulence Models Applied to Flow around Building. *Restructuring: America and Beyond Structures Congress*, ASCE, New York, NY, USA, 1273-1276.

Murakami, S., Mochida, A., Ooka, R., Kato, S., & Iizuka, S. (1996). Numerical Prediction of Flow around a Building with Various Turbulence Models: Comparison of k-ϵ EVM, ASM, DSM, and LES with Wind Tunnel Tests. *ASHRAE Transactions*, **102**, 741-753.

Murakami, S., Kata, S., & Ooka, R. (1994). Comparison of Numerical Prediction of Horizontal Non-Isothermal Jet in a Room with Three Turbulence Models — $k-\epsilon$ EVM, ASM and DSM. *ASHRAE Transactions*, **100** Part 2, 679-704.

Orszag, SA. (1977). Lectures on The Statistical Theory of Turbulence. *Fluid Dynamics*, Dordon and Breach, New York.

Ortega, MA., de Azevedo, & Joao L.F. (1996). Wake Behind a Backward-Facing Step-a Numerical Study. *Journal of the Brazilian Society of Mechanical Sciences*. **18**, 248-262.

Prasad, AK. & Koseff, JR. (1989). Reynolds Number and End-Wall Effect on a Lid-Driven Cavity Flow. *Phys. Fluid A*, **1**, 208-218.

Paolucci, S. (1990). Directt Numerical Simulation of Two-Dimensional Turbulent Natural Convection in An Enclosed Cavity. *J. Fluid Mech.*, **215**, 229-262.

Patankar, SV. (1980). *Numerical Heat Transfer and Fluid Flow*, Hemisphere, New York.

Patankar, SV. & Spalding, DB. (1972). A Calculation Procedure for Heat, Mass an Momentum Transfer in Three-Dimensional Parabolic Flows. *Int. J. Heat Mass Transfer*, **15**, 1787-1806.

Peric, M., Kessler, R., & Scheuer, G. (1988). Comparison of Finite-Volume Numerical Method with Staggered and Collocated Grids. *Computer & Fluids*, **16**, 389-.

Perng, C. & Street, RL. (1989). Three-Dimensional Unsteady Flow Simulations: Alternative Strategies for Volume-Averaged Calculation. *Int. J. Int. J. Numerical Methods in Fluids***9**, 341-361.

Piomelli, U. (1993b). High Reynolds Number Calculations Using The Dynamic Subgrid-Scale Stress Model. *Phys. Fluids A*, **5**, 1484-1490.

Piomelli, U. (1993a). Applications of Large Eddy Simulations in Engineering: An Overview. *Large Eddy Simulation of Complex Engineering and Geophysical Flows*. Cambridge University Press, 119-137.

Pruitt, JM., Hassan, YA., & Steininger, DA. (1991). Large Eddy Simulation of Turbulent flow in A Tube Bundle. *Thermal Hydraulics of Advanced Heat Exchangers. ASME, Nucl. Engrg. Div.*, **5** ,ASME, New York, NY, USA, 1-6.

Pruitt, JM., Hassan, YA., & Steininger, DA. (1993). Large Eddy Simulation of Turbulence Entering a PWR Steam Generator. *Fundamental Aspects of Fluid-Structure Interactions, Applied Mechanics Division*, **151**. ASME, New York, NY, USA, 173-183.

Quartapelle, L. (1993). *Numerical Solution of The Incompressible Navier-Stokes Equations. ISNM*, **113**, Birkhauser verlag.

Rhie and Chow, WL. (1983). Numerical Study of Turbulent Flow Past an Airfoil with Trailing Edge Separation. *AIAA Journal*, **21**, 1525-1532.

Rhodes, N. (1989). Prediction of smoke movement: An overview of field modelds. *ASHRAE Transactions*, **95(1)**.

Rogallo, RS. & Moin P. (1984). Numerical Simulation of Turbulent Flows. *Ann. Rev. Fluid Mech.*, **10**, 99-137.

Said, MNA., Zhang, J., Shaw, CY., & Christian, LL. (1995), Computation of Room Air Distribution. *ASHRAE Transactions*, **101**, Part 1, 1065-1077.

Sakamoto, S., Murakami, S., & Mochida, A. (1993). Numerical Study on Flow Past 2D Square Cylinder by Large Eddy Simulation: Comparison between 2D and 3D Computations. *J. Wind Engrg. Industrial Aerodynamics*, **50**, 61-68.

Schneider, GE. & Raw, MJ. (1987). Control Volume Finite Element Method for Heat Transfer and Fluid Using Collocated Variables, 1. Computational Procedure; 2. Application and Validation. *Numerical Heat Transfer*, **11**, 363-.

Schumann, U. (1973). Ein Verfahren zur Direkten Numerischen Simulation Turbulenter Stromungen in Platten und Ringspaltkanalen und uber seine Anwendung zur Untersuchung von Turbulenzmodellen. *Dissertation, Univ. of Karlsrube.*

Schumann, U. (1975). Subgrid Scale Modelling for Finite Difference Simulations of Turbulent Flows in Plane Channels and Annuli. *J. Comp. Phys.*, **18**, 376-.

Silveira-Neto, A., Grand, D., Metais, O., & Lesieur, M. (1993). A Numerical Investigation of The Coherent Vortices in Turbulence behind A Backward-Facing Step. *J. Fluid Mech.*, **256**, 1-25.

Shaanan, S., Ferziger, JH., & Reynolds, WC. (1975). Numerical Simulation of Turbulence in The Presence of Shear. *Rep. TF-6*, Dept. of Mech. Engrg., Stanford University, Stanford, CA.

Smagorinsky, J. (1963). General Circulation Experiments with The Primitive Equations. *Mon. Weather Rev.*, **91**, 99-164.

Speziale, CG. (1985). Galilean Invariance of Subgrid Scale Stress Models in The Large Eddy Simulation of Turbulence. *J. Fluid Mech.*, **156**, 55-62.

Spitler, JD. (1990). An experimental Investigation of Air Flow and Convective Heat Transfer in Enclosures Having Large Ventilative Rates. *Ph.D. Thesis*, Department of Mechanical and Industrial Engineering, University of Illinos at Urbana-Champaign.

Spitler, JD. & Pedersen CO. (1991). An experimental Facility for Investigation of Interior Convective Heat Transfer. *ASHRAE Transactions*, **97**, Part 1, 497-504.

Sreedhar, M. & Ragab, M. (1994). Large-Eddy Simulation of Longitudinal Stationary Vortices. *Phys. Fluids A*, **6**, 2501-2514.

Su, MD. & Friedrich, R. (1994a). Investigation of Fully Developed Turbulent Flow in a Straight Duct with Large Eddy Simulation. *J. Fluids Engrg., Trans. of ASME*, **116**, 677-684.

Su, MD. & Friedrich, R. (1994b). Numerical Simulation of Fully Developed Flow in A Curved Duct of Rectangular Cross-Section. *Int. J. Heat & Mass Transfer*, **37**, 1257-1268.

Sukoriansky, S., Chekhlov, A., Orszag, SA., Galperin, B., & Staroselsky, I. (1996). Large Eddy Simulation of Two-Dimensional Isotropic Turbulence. *J. Scientific Computing*, **11**, 13-45.

Sun, X. & Dalton, C. (1994). Application of Two SGS Models to Flow Past A Circular Cylinder. *Turbulence in Complex Flows American Society of Mechanical Engineers, Fluids Engineering Division*, **203**, ASME, 21-29.

Sun, X. & Dalton, C. (1995). Application of The LES Method to The Oscillating Flow Past a Circular. *Proc. the 14th Int. Conf. on Offshore Mechanics and Arctic Engrg - OMAE*, **1**, Part A, ASME, New York, NY, USA, 295-304.

Taylor, GI. (1935). Statistical Theory of Turbulence. Parts 1-4. *Proc. Roy. Soc. A*, **151**, 421-.

Temam, R. (1969). Sur L'approximation de la Solution des equation de Navier-Stokes par la Method des Fractionnaires. *Arch. Ration. Mech. Anal.* **32**, 135-153; **33**, 377-385.

Thomas, TG. & Williams, JJR. (1994). Turbulent Simulation of Open Channel Flow at Low Reynolds Number. *Int. Conf. on Hydraulic Engineering Software* **2**, 19-30.

Thomas, TG. & Williams, JJR. (1995). Large Eddy Simulation of Turbulent Flow in An Asymmetric Compound Open Channel. *J. Hydraulic Res.*, **33**, 27-41.

Thomas, TG. & Williams, JJR. (1996). Large Eddy Simulation of a Symmetric Trapezoidal Channel at a Reynolds Number of 430,000. *J. Hydraulic Res.*, **33**, 825-842.

Tsai, HM. & Leslie, DC. (1990). Large Eddy Simulation of A Developing Turbulent Boundary Layer at A Low Reynolds Number. *Int. J. Numerical Methods in Fluids***38**, 519-555.

Voke, PR., Gao, S., & Leslie, D. (1995). Large-Eddy Simulations of Plane Impinging Jets. *Int. J. Numerical Methods in Fluids*, **38**, 489-507.

Wu, X. & Squires, KD. (1997) Large Eddy Simulation of An Equilibrium Three-Dimensional Turbulent Boundary Layer. *AIAA Journal*, **35**, 67-74.

Wu, X., Squires, KD., & Lund, TS. (1997). Large Eddy Simulation of A Spatially-Developing Boundary Layer. *Proc. of ACM/IEEE Supercomputing Conf.*, **2**, IEEE, Los Alamitos, CA, 1838-1857.

Wyngaard, JC. & Moeng, C. (1993). Large Eddy Simulation in Geophysical Turbulence Parameterisation: An Overview. *Large Eddy Simulation of Complex Engineering and Geophysical Flows*, Cambridge University Press, 316-366.

Xin, S. & Quere, P. (1994). Numerical Simulation of 2D Turbulent Natural Convection in Differentially Heated Cavities of Aspect Ratios of 1 and 4. *Direct and Large Eddy Simulation I*, Kluwer Academic Publishers, 423-434.

Xin, S. & Quere, P. (1995). Direct Numerical Simulation of Two-Dimensional Chaotic Natural Convection in A Differentially Heated Cavity of Aspect Ratio 4. *J. Fluid Mech.*, **304**, 87-118.

Yang, K. & Ferziger, JH. (1993). Large-Eddy Simulation of Turbulent Obstacle Flow Using a Dynamic Subgrid-Scale Model. *AIAA J.*, **31**, 1406-1413.

Yoshizawa A. (1986). Large-eddy Simulation of Turbulent Flows. *Handbook of Fluid Mechanics*, Gulf Pub. Co. Book Division, 1277-1299.

Yu, D. & Kareem, A. (1996a). Numerical Simulation of Flow Field around Buildings. *Probabilistic Mech. and Structural and Geotechnical Reliability, Proc. of the Speciality Conference*, ASCE, New York, NY, USA, 490-493.

Yu, D. & Kareem, A. (1996a). Numerical Modelling of Wind-Structure Interactions. *Building an Int. Community of Structural Engineers Structures Congress - Proc.*, **2**, ASCE, New York, NY, USA, 1005-1012.

Wang, SK. (1991). *Handbook of Air Conditioning and Refrigeration.* McGraw-Hill, Inc.

Weathers, JW. & Spitler, JD. (1993). Comparative Study of Room Airflow: Numerical Prediction Using Computation Fluid Dynamics and Full-Scale Experimental Measurements. *ASHRAE Transactions*, **99**, Part 2, 144-157.

Williams, PT., Baker, AJ., & Kelso, RM. (1994). Numerical Calculation of Room Air Motion — Part 3: Three-Dimensional CFD simulation of a Full-Scale Room Experiment. *ASHRAE Transactions*, **100**, Part 1, 549-564.

Zang, Y., Street, RL., & Koseff, JR. (1992). A Dynamic Mixed Subgrid-Scale Model and its Application to Turbulent Recirculating Flows. *Phys. Fluids A*, **5**, 3186-3196.

Zang, Y., Street, RL., & Koseff, JR. (1993). Large Eddy Simulation of Turbulent Cavity Flow Using a Dynamic Subgrid-Scale Model. Engineering Application of Large Eddy Simulations, **162**, FED, ASME.

Zhang JS., Wu, GJ., & Christianson, LL. (1992). Full-Scale Experimental Results on the Mean and Turbulent Behaviour of Room Ventilation Flows. *ASHRAE Transactions*, **98**, Part 2, 307-318.

Zhang JS., Wu, GJ., & Christianson, LL. (1993). New similitude Modelling Technique for Nonisothermal Room Ventilation Flows. *ASHRAE Transactions*, **99**, Part 1, 129-138.

Zhao, H. & Voke, PR. (1996). Dynamic Subgrid-Scale Model for Low-Reynolds-Number Channel Flow. *Int. J. Numerical Methods in Fluids*, **23**, 19-27.

Zhou, F. Charles, S., & Chen, B. (1997). Large Eddy Simulation of Strongly Curved Open Channel Flow. *J. Hydrodynamics*, **8**, 27-34.

Appendix A

Derivations of Formule

This appendix provides derivations of formule supporting the claims appearing in the text of the thesis.

A.1 Product of Two Modes of Fluctuation of Different Length Scales

In this section, we will determine the modes involved in the product of two spatially fluctuating modes, ϕ_1 and ϕ_2, of different length scales which are, respectively, Δ_1 and Δ_2. It is assumed without losing generality that both ϕ_1 and ϕ_2 are 1-D spatially

fluctuating modes and have zero initial phases, so that they can be expressed as

$$\phi_1 = A_1 \sin(\frac{2\pi x}{\Delta_1})$$

$$\phi_2 = A_2 \sin(\frac{2\pi x}{\Delta_2})$$

where A_1 and A_2 are the amplitudes of ϕ_1 and ϕ_2. Thus

$$\phi_1\phi_1 = A_1 A_2 \sin(\frac{2\pi x}{\Delta_1}) \sin(\frac{2\pi x}{\Delta_2})$$

$$= \frac{1}{2} A_1 A_2 [\cos(\frac{2\pi x}{\Delta_1} - \frac{2\pi x}{\Delta_2}) - \cos(\frac{2\pi x}{\Delta_1} + \frac{2\pi x}{\Delta_2})]$$

$$= \frac{1}{2} A_1 A_2 [\cos(\frac{2\pi x}{\frac{\Delta_1\Delta_2}{\Delta_1-\Delta_2}}) - \cos(\frac{2\pi x}{\frac{\Delta_1\Delta_2}{\Delta_1+\Delta_2}})]$$

which shows that the resultant expression involves modes of length scale $\frac{\Delta_1\Delta_2}{\Delta_1-\Delta_2}$ and $\frac{\Delta_1\Delta_2}{\Delta_1+\Delta_2}$.

A.2 Coefficient $K_{\tau_{ij}}$ in Germano *et al*'s Dynamic SGS Model

In the case that the characteristic length scale of the volume average Δ_i is extremely small compared with the dominant length scale of the fluctuation B_i, and the step of time advancing is extremely small, *i.e.* $\eta \approx 0$, the distribution function (3.32) can be approximated by the linear relation shown in Figure A.1.

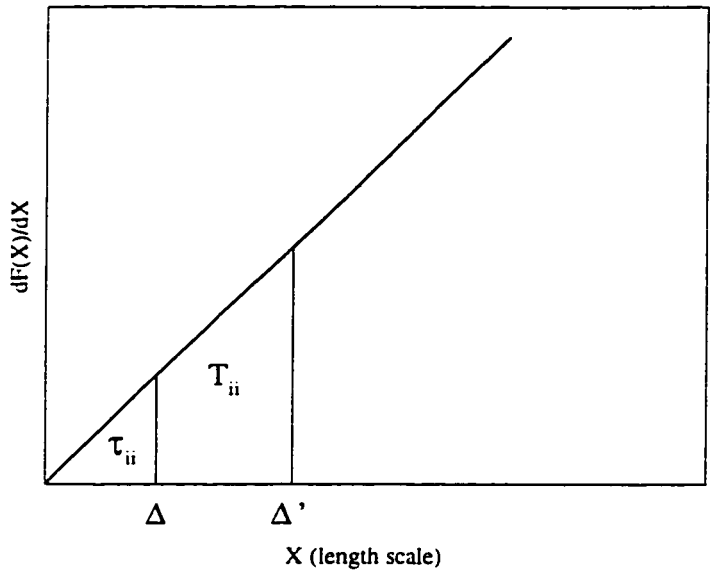

Figure A.1: Linear approximation of the distribution function $F(X)$

If $\Delta' = 2\Delta$, then it is apparent from Figure A.1 that

$$K_{\tau_{ij}} = \frac{1}{3}$$

based on the following reasoning: In Germano *et al*'s (1991) SGS model, it is assumed that the SGS eddy viscosity ν_t is identical in the sub-grid and test-grid levels. On the other hand, the difference between the resolvable strain rate tensors in sub-grid and test-grid levels is negligible when an extremely fine grid is applied. Thus, the auto-correlation components of the SGS Reynolds stress tensors in both the sub-grid and test-grid levels are proportional to the squares of the characteristic length scale of averaging. Therefore,

$$K_{\tau_{ij}} = \sqrt{\frac{\tau_{ii}\tau_{jj}}{T_{ii}T_{jj}}} = \sqrt{\frac{\Delta_i{}^2\Delta_j{}^2}{(\Delta_i'^2 - \Delta_i{}^2)(\Delta_j'^2 - \Delta_j{}^2)}} = \frac{1}{3}$$

A.3 Turbulence Intensity at Inlet of Room

A direction independent turbulent diffusion α_t can be defined from equation (3.41) as:

$$\alpha_t = \frac{1}{2}\breve{u}_t L_g \tag{A.1}$$

where $\breve{u}_t$ is the RMS of the inlet turbulence, and $L_g = 0.05\ m$ is the length scale of the grille of the inlet. If the ratio of the turbulent diffusion α_t over the kinematic viscosity ν is 29, then

$$\breve{u}_t = (2)(29)(\nu)/(0.05\ m) = (2)(29)(1.6834 \times 10^{-5}\ m^2/s)/(0.05\ m) = 0.01953\ m/s$$

Thus, the inlet turbulence intensity I_t for the case of 30 ACH is

$$I_t = \frac{\breve{u}_t}{V_{in}} = \frac{0.01953\ m/s}{0.8\ m/s} = 2.44\%$$

Appendix B

Flow Charts for Subroutines

The flow charts for all five subroutines (LES-LOCAL, LES-SGS, LES-FALSE, LES-CPR, LES-SOLVER) which are called directly by the mainline LES-MAIN are given below.

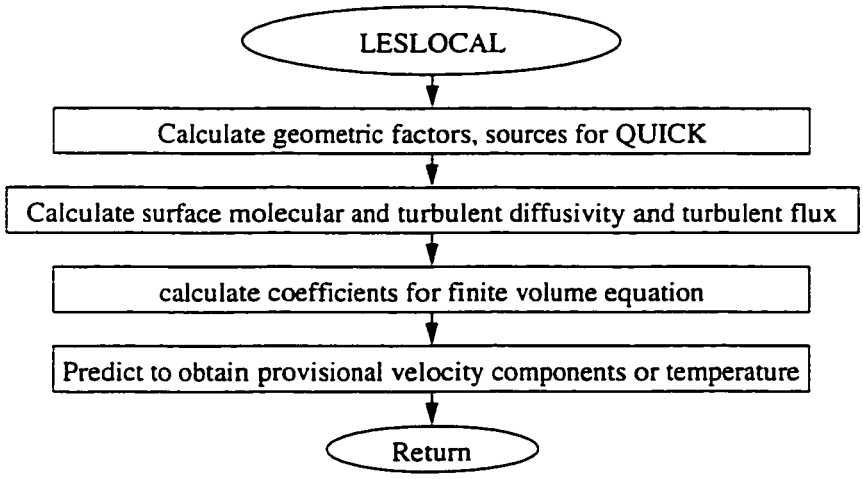

Figure B.1: Flow chart for the code LES-LOCAL

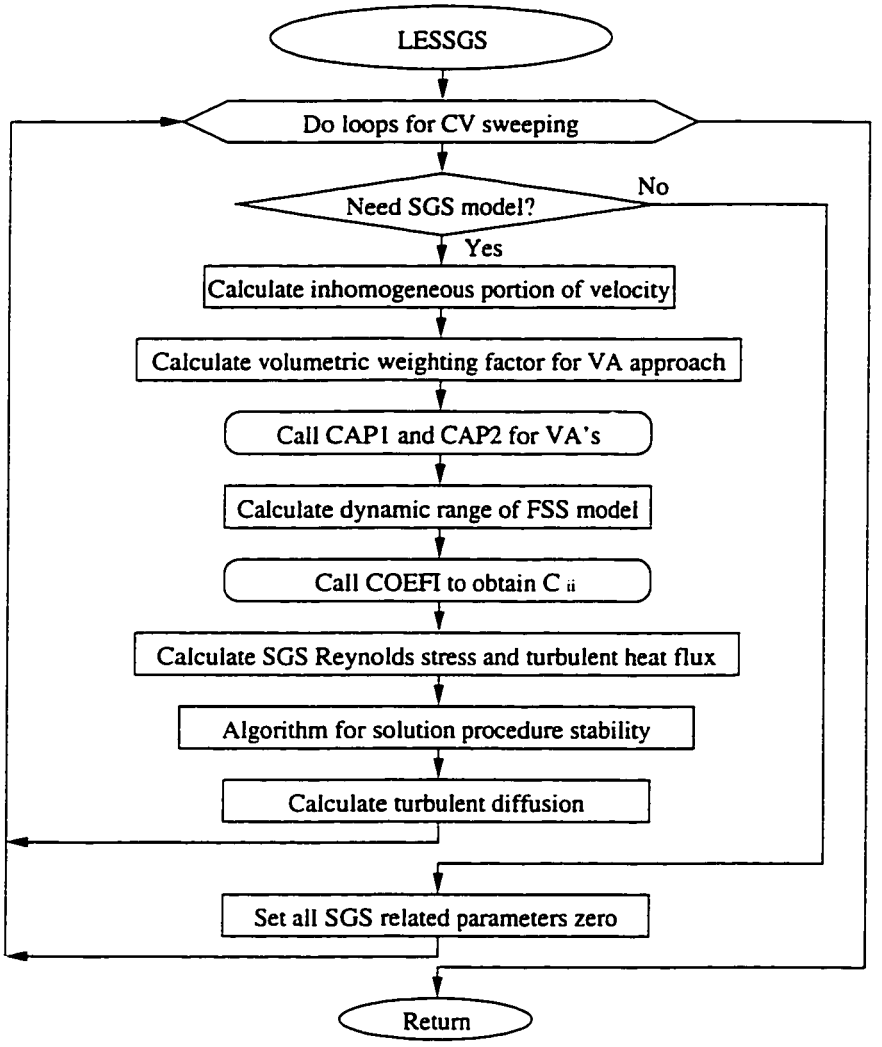

Figure B.2: Flow chart for the code LES-SGS

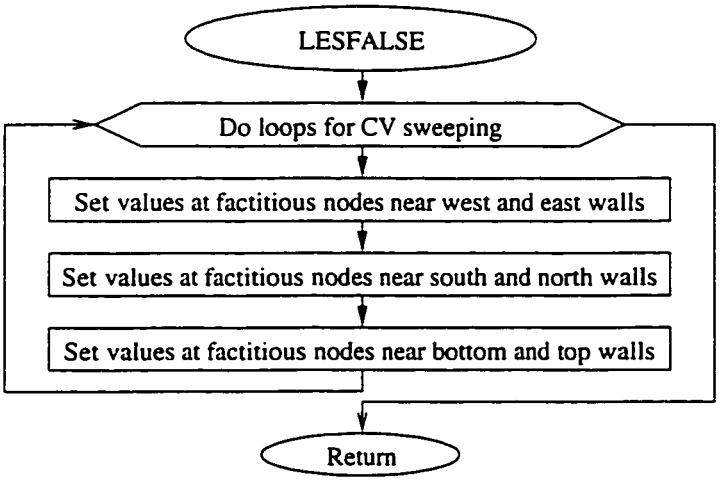

Figure B.3: Flow chart for the code LES-FALSE

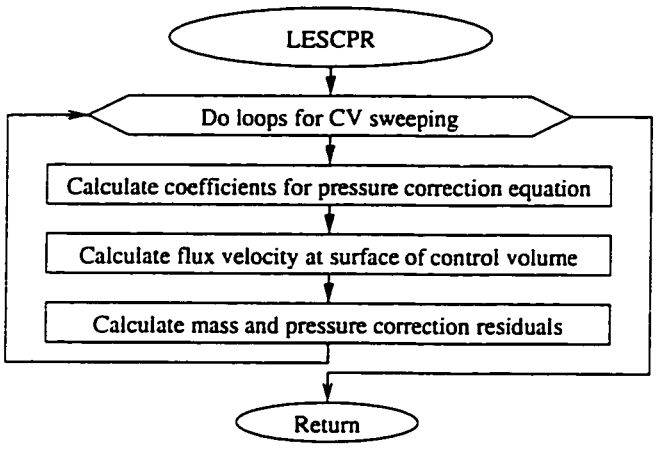

Figure B.4: Flow chart for the code LES-CPR

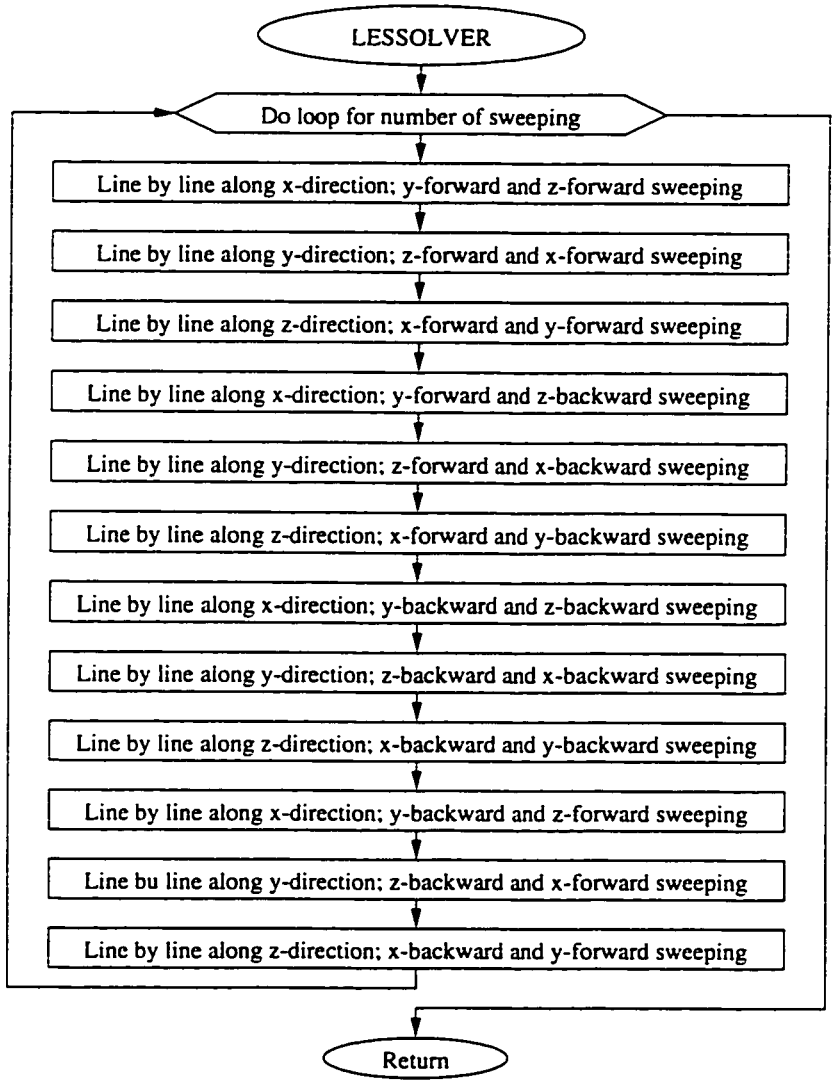

Figure B.5: Flow chart for the code LES-SOLVER

IMAGE EVALUATION
TEST TARGET (QA-3)

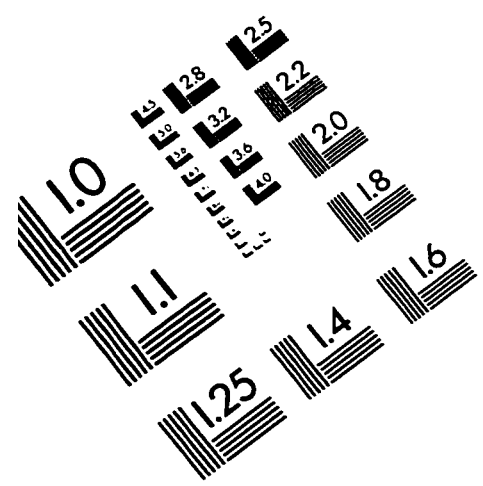

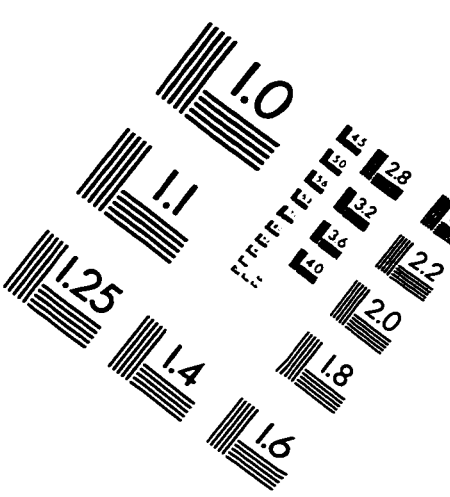

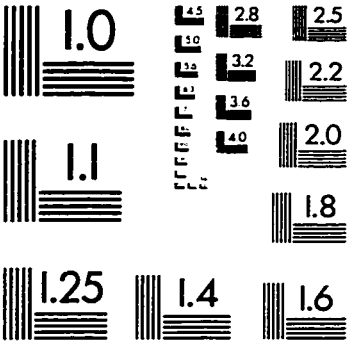

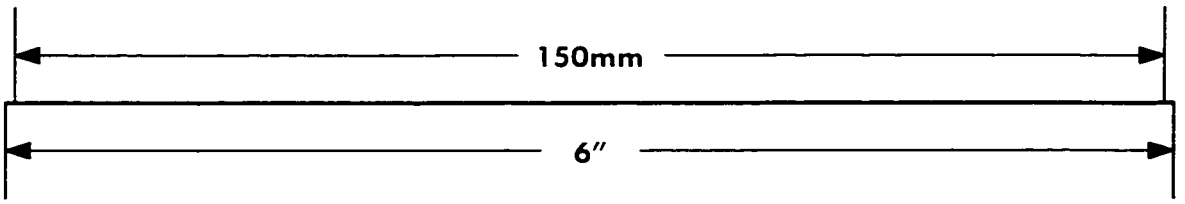

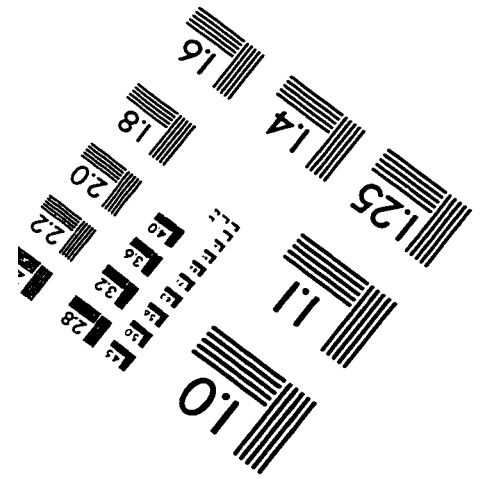

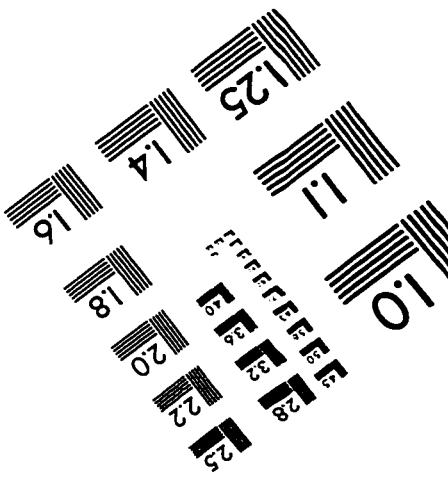

APPLIED IMAGE, Inc
1653 East Main Street
Rochester, NY 14609 USA
Phone: 716/482-0300
Fax: 716/288-5989